Modeling and Design of Modern Cocciopesto Mortars

Václav Nežerka

supervisor: **Jan Zeman, Ph.D.**

co-supervisor: **Pavel Tesárek, Ph.D.**

Czech Technical University in Prague

Faculty of Civil Engineering

A thesis submitted for the degree of

Doctor of Philosophy

December, 2015

I would like to dedicate this thesis to my recently deceased grandfathers, Václav Nežerka and Václav Hušpauer. They always appreciated my academic achievements, and inspired me enormously to study and work hard.

Acknowledgements

First of all, I would like to thank my supervisor Jan Zeman for his support, encouragement and patience. It is a pleasure to cooperate with him; he is a perfect mentor and his brilliance is a great inspiration for me. Next, I want to express my gratitude to my co-supervisor Pavel Tesárek for his willingness to help me with the preparation of experiments any time I needed. Huge thanks go to Petr Kabele for his trust in me and for giving me the opportunity to participate in a project led by him.

Thanks also belong to several members of the Department of Mechanics at the Faculty of Civil Engineering, CTU in Prague, in particular to Tomáš Plachý and Jiří Němeček for their help with experimental assessment of material properties, to Vít Šmilauer for many fruitful discussions, to Bořek Patzák and Jan Vorel for their patience when introducing me into the finite element analysis software OOFEM, and last but not least to Miloš Drdácký, Zuzana Slížková and Dana Křivánková from the Institute of Theoretical and Applied Mechanics, Academy of Science Czech Republic, for numerous consultations and cooperation on the project.

Special thanks go to my parents for their huge support during the years of my study, to my fiancée, Monika, for putting up with long and late hours at the computer, and to my friend and colleague Michael Somr for many discussions and long refreshing bicycle rides that kept my mind fresh. Last but not least, I want to thank Jakub Antoš for amazing cooperation when working under my supervision.

The work presented in this thesis was carried out as part of the research project NAKI No. DF11P01OVV008. I gratefully acknowledge the scholarship and financial support which I received from the Ministry of Culture of the Czech Republic under this project.

Abstract

Architectural conservation and repair are becoming increasingly important issues in many countries due to numerous prior improper interventions, including the use of inappropriate repair materials over time. As a result, the composition of repair masonry mortars is now being more frequently addressed in mortar research. Just recently, for example, it has become apparent that Portland cement mortars, extensively exploited as repair mortars over the past few decades, are not suitable for repair because of their chemical, physical, mechanical, and aesthetic incompatibilities with original materials.

Lime-based mortars were widely used in history and nowadays they are often required for restoration of ancient masonry structures. However, their slow setting, relatively low tensile strength, and quite extensive shrinkage cracking are main obstacles to their application. These have been partly overcome by the addition pozzolans and/or crushed bricks, exploited by masons since the Roman period, and the mortars containing crushed clay products, known as *cocciopesto*, proved to be more resistant mainly with respect to the seismic loading. So far, their enhanced strength and durability have been attributed to the formation of hydration products on the interface between the lime-based matrix and brick fragments. These conclusions have been exclusively reached on the basis of macroscopic mechanical tests and local chemical analyses of mortar constituents, while the local mechanical analyses were lacking.

In order to understand the behavior of lime-based mortars, and to identify the influence of pozzolans, nine different sets of lime-pozzolan pastes were studied. The chemical composition and microstructure were investigated by means of thermogravimetry, mercury intrusion porosimetry, backscattered electron microscopy microscopy and energy-dispersive X-ray spectroscopy. The mechanical strength and fracture properties were determined from destructive tests, while the evolution of the dynamic Young's modulus was monitored using the resonance method. The study revealed that metakaolin exhibits much stronger pozzolanic activity than crushed bricks and that the mechanical properties of pastes are not necessarily enhanced by the addition of pozzolans. However, the significant shrinkage reduction results in elimination of cracking around aggregates contained in mortars.

Next, it was necessary to quantify the elastic properties of the interfacial transition zone (ITZ) between crushed brick fragments and the surrounding matrix by means of nanoindentation, complemented by microscopy investigations. To that goal, an ancient mortar sample from a late Byzantine church was investigated. The elemental analysis revealed an increased amount of silica and alumina in the vicinity of brick fragments in relation to the matrix composition. In addition, an increased

stiffness of ITZ compared to the lime matrix in the distance up to 20–30 μm from the grains was encountered by nanoindentation. Therefore, it was confirmed that the interface is stronger than the surrounding matrix, unlike the situation of inert sand aggregates, where ITZ is weakened by shrinkage-induced cracking. The average Young's modulus in ITZ assessed by nanoindentation (18.4 GPa) was comparable with low-density C-S-H phases that appear in cementitious composites. On the other hand, no such increase of ITZ stiffness was observed in the case of reproduced mortars. The curing period of 3 months did not allow the formation of the reinforcing layer, but the vicinity of brick fragments was not weakened by the formation of shrinkage cracks. These information contributed to a better understanding of traditional mortars and provided the input data for their further micromechanical modeling.

A continuum micromechanics model for the simulation of uniaxial compressive and tensile tests on lime-based mortars was developed in order to predict their stiffness, compressive and tensile strengths, and tensile fracture energy. In tension, an incremental strain-controlled form of the Mori-Tanaka scheme with a damageable matrix phase was adopted, while a simple J_2 yield criterion was employed in compression. To reproduce the behavior of lime-based mortars correctly, the scheme must take into account shrinkage cracking among aggregates. This phenomenon was introduced into the model via penny-shaped cracks, whose density was estimated on the basis of a particle size distribution combined with the results of finite element analyses of a single crack formation between two spherical inclusions. The predictions showed a good agreement with experimental data and explained the advantages of compliant crushed brick fragments, often encountered in ancient mortars, over stiff sand particles. The validated model provided a reliable tool for optimizing the mortar mix composition.

Based on the outputs of the study, the on lime-pozzolan pastes combined with the model predictions, a mortar mixture ensuring superior strength parameters was proposed. The mortar contained an optimized amount of lime, metakaolin, sand, and crushed bricks, in the mass ratios 0.7, 0.3, 1.0, and 1.5, respectively. Its performance was compared with various mortars intended for repairs of historic structures and the reference one, enriched by Portland cement. An integrated experimental-numerical approach was pursued to test the structural performance of individual mortars and to identify key mortar parameters influencing the load-bearing capacity of masonry piers subjected to a combination of compression and bending. The simulations were in a good agrement with the experimental observations, and indicated that the superior load-bearing capacity of the masonry pier containing the optimized modern cocciopesto mortar was a consequence of its high compressive strength.

Contents

Goals

The major goal of the presented research was to study the behavior of lime-based mortars containing crushed bricks, also known as cocciopesto, at multiple scales, develop a computational model to optimize their composition, and demonstrate the superior structural performance of the designed mortar through a full-scale masonry testing. To achieve these goals, it was necessary to divide the thesis into the following sub-goals:

- comprehensive literature study, identification of crucial mortar parameters, and selection of an appropriate modeling strategy, Chapter 1,
- identification of the influence of pozzolans, and investigation of the microstructure and properties of lime-based pastes without any aggregates, Chapter 2,
- quantification the elastic properties of the interfacial transition zone (ITZ) between crushed brick fragments and the surrounding matrix by means of nanoindentation complemented with microscopy analysis, Chapter 3,
- development of a continuum micromechanics model for the simulation of uniaxial compressive and tensile tests on lime-based mortars, in order to predict their stiffness, compressive and tensile strengths, and tensile fracture energy — with the aim to develop a computational tool for the optimization of the mortar composition to be used in conservation and restoration of architectural heritage, Chapter 4,
- testing of the optimized modern cocciopesto mortar, and comparison with the structural performance of various lime-based alternative materials intended for repairs of structures, Chapter 5,
- fifteen-month monitoring of the mortar deterioration when exposed natural agents such as wet-dry and freeze-thaw cycles in outdoor environment, Chapter 6.

Chapter 1

Introduction and State of Art

Ancient structures embody the culture and stories of people, who built, used, and lived in them. The charm of ancient structures attracts tourists to the sites with well-preserved architectural heritage, which in turn has a positive economic impact on the region. The majority of ancient structures in Central Europe are made of masonry, being a traditional construction material that exhibits an extraordinary durability if an adequate maintenance is provided. For that reason, conservation of old masonry structures is encouraged by the governments and a significant effort is devoted to develop materials and technologies compatible with the ancient ones. The deterioration and damage of such structures are usually concentrated to the joints that surround and bond the stone or brick units.

Among the restoration community it is well known that the materials used for repairs should be compatible with the original materials. Serious damage to a number of historic masonry structures has been caused by an extensive use of Portland cement mortar over the past decades. The intention for its use was to avoid the inconveniences connected with the originally used lime-based mortars, such as slow setting, high shrinkage and low strength [1]. However, the use of the Portland cement mortars has been reconsidered for the repairs of historic masonry, because of their low plasticity, excessive brittleness and early stiffness gain [2, 3, 4, 5]. Moreover, the relatively high content of soluble salts that leach over time [3, 4, 5] can severely damage the original masonry units because of large crystallization pressures [6, 7] and produce anaesthetic layers on the surface.

The strict regulations with respect to the Portland cement use led to the exploitation of traditional additives, such as volcanic ash, burnt clay shale [8] or increasingly popular metakaolin [5]. These additives, known as *pozzolans*, have been used since ancient times in combination with lime to improve the moisture resistance of mortars, their freeze-thaw resistance [9], and also to increase their durability [1, 5] and mechanical strength [10, 11]. The use of pozzolans is also crucial in the case of rendering mortars, where the severe cracking of pure-lime mortars can cause spalling of the facade surface layers and has a negative aesthetic impact [12]. Pozzolanic additives are very effective in mitigating shrinkage [13], shrinkage cracking and consequent crack opening. Mortars enriched by pozzolans are able to harden in a high relative humidity and therefore they are referred to as *hydraulic* (that is why they were extensively used in baths or to support glazed tiles, where the access of CO_2 was limited). More information about the chemical processes in lime-based mortars is provided in Section 1.1 following next.

Over a long period of the lime-based mortars use, the ancestors tried find alternatives to natural pozzolans when there was no natural source available in the region. The Phoenicians were probably the first ones to add crushed clay products, such as burnt bricks, tiles or pieces of pottery, to the mortars in order to increase their durability and strength. Crushed bricks were often added to mortars used in load-bearing walls in the Roman Empire [14] and Romans called the material cocciopesto [15]. Cocciopesto mortars were then extensively used from the early Hellenistic up to the Ottoman period in water-retaining structures to protect the walls from moisture, typically in baths, canals and aqueducts [16, 17]. The brick dust was mainly used for rendering, while large pebbles up to 25 mm in diameter appeared mainly in masonry walls, arches and foundations [18], and the thickness of joints then often exceeded 40 mm.

The enhanced strength, durability and increased resistance of the cocciopesto mortars to seismic loading have been attributed to the formation of hydration products at the interface between the crushed brick fragments and the surrounding lime matrix. However, according to the outcomes of even preliminary micromechanical modeling [19], it seemed very unlikely that the thin coating of hydration products could have such a positive influence on the effective mortar properties, which has been experimentally confirmed by our comprehensive study on lime-based pastes [13] and results of nanoindentation on ancient mortar samples [20].

Based on the findings presented in this work, the crushed bricks are rather seen as a very suitable filler, ensuring a good adhesion between the aggregates and lime-based matrix, and because of their water retention resulting from their high porosity, the presence of crushed bricks can promote the pozzolanic reaction for a relatively long period. Therefore, it seems reasonable to combine brick fragments with pozzolans of a higher reactivity, such as metakaolin [13]. Finally, the crushed brick fragments are relatively compliant, which mitigates the shrinkage microcracking [21, 22] and reduces the effective mortar stiffness [19, 23, 24].

1.1 Chemical Processes

Hardening in non-hydraulic lime mortars is accomplished by drying and carbonation. Carbonation is a chemical process during which the slaked lime (portlandite), $Ca(OH)_2$, reacts in a solution with atmospheric carbon dioxide, CO_2, to form the calcium carbonate (calcite), $CaCO_3$:

$$Ca(OH)_2 + CO_2 \rightarrow CaCO_3 + H_2O, \tag{1.1}$$

where the resulting compound is significantly stronger and less soluble than the portlandite it replaces. The carbonation process requires a presence of water, since $Ca(OH)_2$ is accessed by CO_2 in its dissolved state [25], but the water to binder ratio should not be unnecessarily high to avoid excessive shrinkage cracking and strength reduction [26, 27]. Because the mortar surface is directly exposed to the atmospheric CO_2, the carbonation is always more developed on the surface than in the core of mortar samples [1].

Compared to historic limes, today's commercial ones are very pure, despite the very benevolent regulating standard EN 459-1 requiring the mass of CaO and MgO in the commonly used CL-90 lime hydrate higher than 90 %. However, the presence of impurities in historic limes mortars was not always harmful [28], since the content of silica (SiO_2) and alumina (Al_2O_3) was mainly responsible for their hydraulic character, and the reaction between lime and SiO_2

or Al_2O_3 leads to the formation of calcium silicates or aluminates [29].

As a result, the contemporary high-purity limes without any additives lack the required durability, strength and suffer from an enormous shrinkage, but the minerals can be introduced in the form of pozzolans, such as metakaolin. During the hydration process, calcium aluminate and silicate hydrates are formed after activation of the aluminate and silicate phases of pozzolans in the presence of $Ca(OH)_2$ and water [30]. It has been reported by Vejmelková et al. [28] that the pure lime mortars exhibited about 10 % higher porosity than those containing metakaolin replacing 20 % of the lime powder mass. This phenomenon can be explained by the formation of hydration phases, such as calcium silicate and aluminate hydrates, C_3AH_6 and C_2ASH_8, resulting from the reaction of silicate and aluminate ions with Ca^{2+} ions [31]. According to a few studies, calcium-silicate-hydrates (CSH) and calcium-aluminum-silicate-hydrates (CASH) are the main hydrated phases formed at the room temperature after the pozzolanic reaction of metakaolin and $Ca(OH)_2$ [30, 32, 33].

Vitrivius, Roman author, architect and engineer, who lived in the first century BC, recommended in his *Ten Books on Architecture* to add some portion of crushed bricks into lime-based mortars. Despite his ignorance of chemical processes in the mortars, he knew by experience, that the addition of crushed clay products can increase mortar durability and strength. According to Silva et al. [34], the amorphous components of brick fragments are mainly represented by aluminosilicates that are able to react with lime, which makes the interfacial surface alkaline. Products of the chemical reaction are mainly CSH and CASH, giving the mortars hydraulic character. The thin layer of hydration products filling the voids and discontinuities in the thickness region of about 20µm from the interface [35, 36] forms only if the ceramic clay is fired at appropriate temperatures between 600 and 900 °C [37].

1.2 Microstructure

After mixing lime hydrate with water, portlandite crystals are formed, followed by the formation of calcite plates. The structure of such matrix is not very dense and many discontinuities are present. Scattered electron microscopy (SEM) images of the lime binder after 28 days of curing show crystals of size less than 10 µm [27], Figure 1.1. The cracking can very easily occur due to shrinkage that results from the carbonation process and the removal of absorbed water from the capillary pores, inducing autogenous stresses that are higher than the matrix tensile strength.

The products of pozzolanic reaction can be seen in Figure 1.2: aluminates crystallize in the form of hexagonal pellets similar to those of portlandite but the crystals are usually larger and thinner [30] and CSH phases most commonly adopt the morphologies in the form of fibres, flakes or a honeycomb structure [1].

Based on the results of mercury intrusion porosimetry (MIP), Arandigoyen et al. [38] concluded that well-carbonated lime pastes have two pore size peaks — the first one between 0.5 and 1.0 µm in diameter, varying according to the amount kneading water used for mortar preparation, and a smaller peak between 0.1 and 0.2 µm, independent of the water content in the fresh mortar. The pore-size peak between 0.1 and 0.2 µm results from the change of the matrix microstructure due to recrystallization of the portlandite to the smaller carbonate crystals,

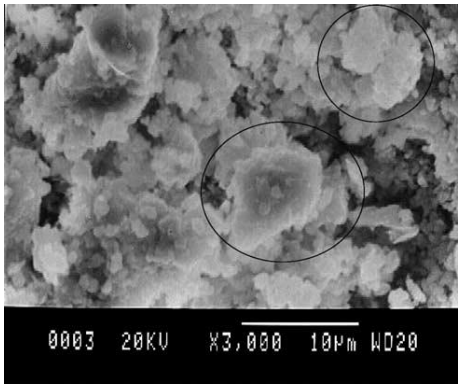

Figure 1.1: Calcite crystals in the lime paste (reproduced from [27]).

while the formation of pores around 1.0 µm is a consequence of the binder dispersion within the mortar [39].

The porosity at the interface between relatively stiff sand grains and the surrounding matrix is increased because of shrinkage [13]. Hence the weaker interfacial transition zone (ITZ) forms and debonding takes place. The formation of cracks and the debonding of grains can be clearly observed in the BSE images by Mosquera et al. [40], unlike in the case of more compliant crushed brick aggregates [18], where the thin coating composed of hydration products [18, 35, 41] can form, and the porosity and shrinkage cracking are reduced [13, 20, 42, 43]. However, due to the very limited thickness of the reaction rims, their significance is, based on our studies related to micromechanical modeling [19] and nanoindentation at the interface [20], often exaggerated, even though the reinforcement of the interface and reduced porosity certainly do ensure a better adhesion between the brick fragments and the surrounding matrix.

1.3 Shrinkage

Fine shrinkage-induced cracks are a distinct characteristics of lime-based mortars used both as rendering or in masonry joints. These cracks are caused by the relatively high shrinkage of the binder, restrained by a substrate or surrounding masonry blocks during the hardening process. If the shrinkage-induced stress is higher that the tensile strength at any time during the mortar hardening, a crack appears. However, the relationship is not that simple, one has to account for the effect of stress relaxation which prevents the crack formation in the early age of the mortar hardening [12].

There are basically two efficient ways to reduce the shrinkage in mortars: first the introduction of pozzolans leads to a significant shrinkage reduction in the lime matrix, and second, the increase of aggregates amount reduces the volume of the matrix and thus eliminates the effective mortar shrinkage. Moreover, even the mortar shrinkage normalized to the amount of the matrix is lower in the case of aggregate-rich samples, as the rigid inclusions restrain the volume changes of the surrounding matrix [12, 44]. Apparently the shrinkage is better restrained by bigger aggregates [27]; from the microscopy observations it appears that the shrinkage cracks are present and blocked mainly between bigger-size aggregates, as proposed also in our model [21, 24]. The formation of microcracks between the relatively stiff sand grains is

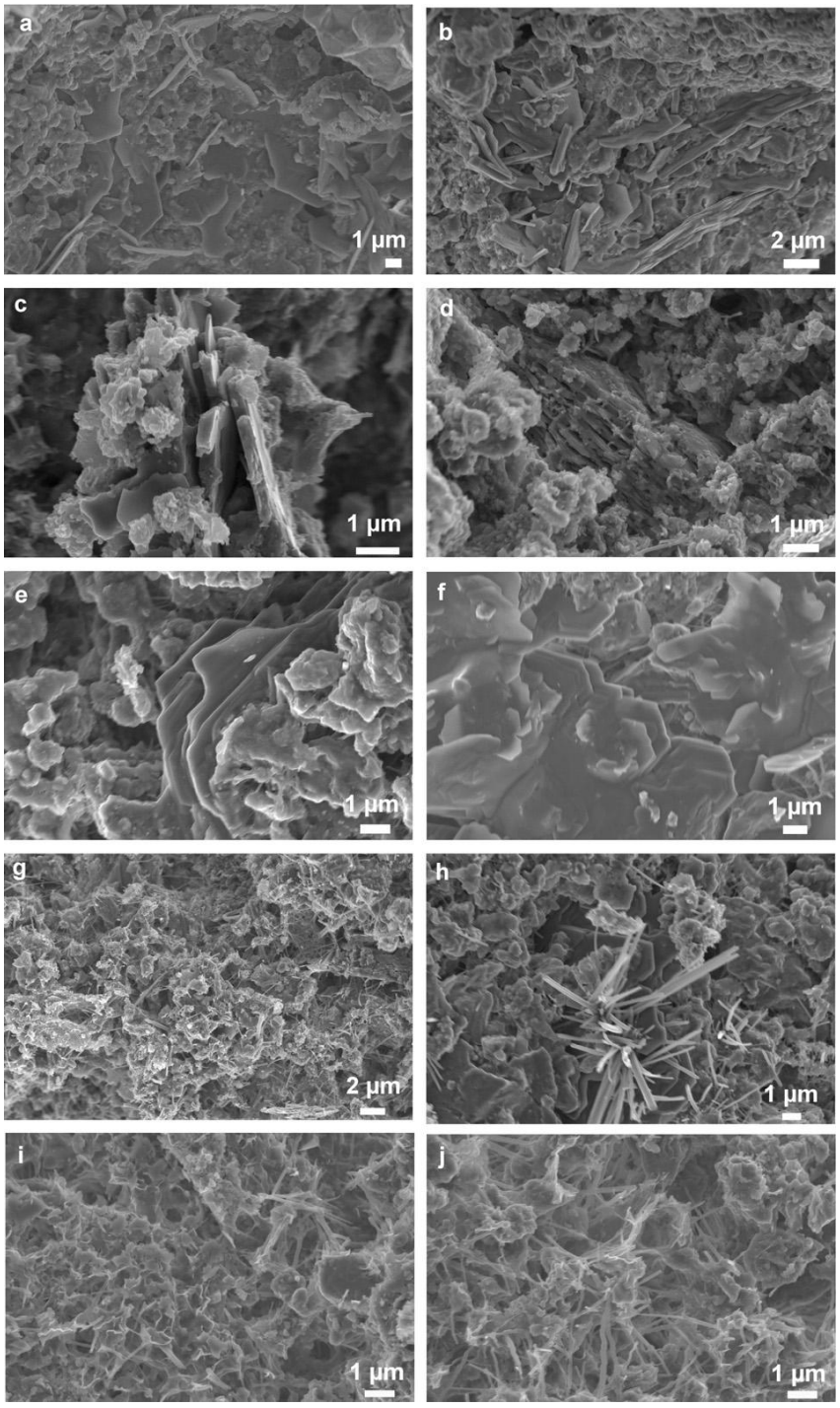

Figure 1.2: SEM images of hydrated phases formed after pozzolanic reaction: hexagonal plates randomly oriented observed in (a) and (b), overlapping sheets of aluminate observed in (c) and (d), aluminate crystals oriented in one direction (e), CSH fibres isolated flakes in (g) and (h), honeycomb structure and reticular network of silicated hydrates in (i) and (j), respectively (reproduced from [1]).

probably responsible for the reduced stiffness and strength of mortars rich in sand, as reported in [1, 29, 45].

1.4 Mechanical Properties

Beside the excessive shrinkage, the limited strength of poorly designed lime-based mortars is the major obstacle for their use in practice. Therefore, one must be very careful when designing the proper mix — it must contain an optimum amount of aggregates of a suitable grain-size distribution and it should be enriched by a reactive pozzolan to provide a durable and strong matrix. Finally, the content of kneading water must be minimized in order to avoid excessive shrinkage and porosity, but it must be added in a sufficient amount to ensure a sufficient workability.

1.4.1 Influence of Pozzolans

The addition of aluminates and silicates in the form of pozzolans does not only reduce shrinkage, but also strength and stiffness of the hydraulic mortars are higher. According to the study by Velosa et al. [5], the flexural strength of mortars can be increased up to 3-times (from 0.28 to 0.83 MPa after 90 days of curing) if 25 % of the lime powder mass is replaced by metakaolin, as well as the compressive strength (from 0.9 to 2.5 MPa after 90 days of curing), almost reaching the strength of common Portland cement mortars. On the other hand, the increase of Young's modulus is not that significant, only 2.5-times higher than in the case of pure lime mortars, allowing for bigger elastic deformation. This is in agreement with the findings of Vejmelková et al. [28] who also concluded that in comparison with pure lime mortars a remarkable improvement of mechanical properties can be achieved if the 20 % of lime is replaced by metakaolin. According to their study the compressive strength increased from 1.43 to 7.03 MPa and the flexural strength from 0.6 to 1.6 MPa after 90 days of curing.

1.4.2 Role of Aggregates

It is generally accepted that the presence of aggregates increases the resistance of mortars to mechanical loading and reduces their shrinkage. However, there is a threshold beyond which the additional aggregates make the mortar weaker. Traditionally, it has been established that binder to aggregate volume ratio equal to 1 : 3 is the most suitable for repair mortars, reaching the highest strength and that mortars of higher ratios suffer from shrinkage cracking. Stafanidou and Papayianni [27] obtained the highest values of compressive strength in the case of pure lime mortars having the binder to aggregate volumetric ratio equal to 1 : 2.5 (about 2.5 MPa). Minimum porosity, though, was measured on the samples containing the highest binder to aggregate ratio (1 : 5). It is well known that the strength of cement-based mortars is reduced with an increasing porosity, e.g. [46], but in the case of lime-based mortars this relationship is not that clear [45].

Lanas et al. [29] reported that the use of siliceous aggregates results in mortar strength reduction, while limestone aggregates contribute to its increase. That supports the idea that

the relatively stiff sand grains contribute to the formation of microcracks at the interface with matrix, while more compliant particles of limestone or crushed bricks reinforce mortars more efficiently. Regarding the aggregate size, based on the study by Stefanidou and Papayianni [27] it seems most favorable to use the sand of grain size ranging between 0 and 4 mm, because this fraction produced mortars of the highest compressive strength (3.6 MPa), while the bigger grains caused the mortar strength reduction. The bond between the coarse aggregates, together with the strength of the surrounding matrix, were reduced by the shrinkage-induced cracking, Figure 1.3.

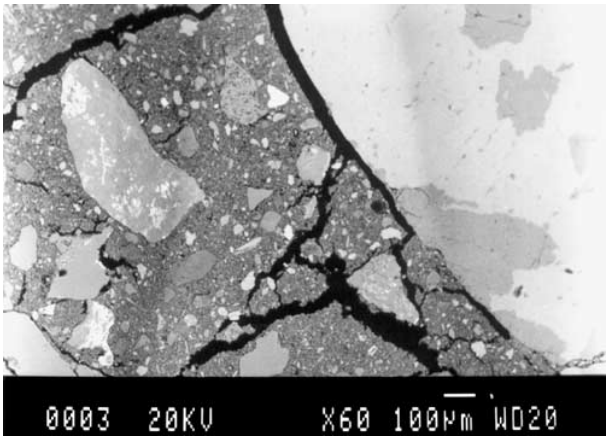

Figure 1.3: Electron microscopy images of the pure lime mortar with coarse aggregates (reproduced from [27]).

1.4.3 Influence of Mortar Age

The age of pure lime mortars favors the carbonation process and therefore the older the mortar is, the higher strength and stiffness it attains, as manifested by the results of experimental studies by Vejmelková at al. [28], and Stefanidou and Papayianni [27]. On the other hand, hydraulic mortars start to lose their strength approximately from the 28-th day. Veiga and Carvalho [47] attributed the approximately 5 % strength reduction between 28-th and 90-th day in the case of lime-metakaolin mortars to microcracking caused by the binder shrinkage, to which especially the flexural strength is very sensitive. Similar results of early strength and stiffness gain, followed by a slight reduction, were also reported by Giavarini et al. [48].

1.5 Micromechanical Modeling

Nowadays, with the availability of a great computational power, micromechanical modeling can be efficiently used for the selection, design, and optimization of structural materials. Such approach is relatively cheap, minimizing the tedious and time-consuming process of samples preparation and time-demanding experimental analysis.

In the engineering practice, when evaluating the response of the structure at the macro-level, it is common and advantageous to replace the highly inhomogeneous concrete or mortars by an

equivalent continuum in the terms of elasticity parameters, strength and other properties of interest. The estimation of the effective macroscopic properties is referred to as *homogenization*. For that purpose, it is crucial to know the properties of individual phases, their distribution within the material, and to choose the proper model representing the material in a realistic way. Therefore, the representative volume element (RVE) must be small enough to represent only the infinitesimal volume from the structural point of view (much smaller than the macroscopic body [49]), but large enough to include all inhomogeneities and to yield the effective composite properties independent of its location. RVE size is dependent on the geometry of the microstructure, homogenized property, contrast in the properties of individual inhomogeneities, and the required accuracy [50].

The first homogenization theories date back to Voigt, who in 1887 introduced the first theory of mixtures assuming a parallel configuration of phases and perfect bond among them. The second mixture theory with serial configuration of phases was introduced in 1929 by Reuss. These energy-based methods define the true upper (Voigt) and lower (Reuss) bounds of bulk and shear moduli of isotropic materials, as proven by Hill [51]. More restrictive bounds, developed using variational principles, were introduced by Hashin and Shtrikman [52], and generalized in many aspects later on [53].

Another group of homogenization methods is based on the Eshelby solution, relating the eigenstrains in ellipsoidal inclusions to externally applied strain via fourth-order Eshelby tensor [54]. This finding is of a fundamental importance for the development of the scheme of dilute distribution where the defects are described by an equivalent eigenstrain. This simple scheme assumes the inhomogeneities to be dilutely distributed in a homogeneous matrix so that their interaction among each other and with the boundary of RVE can be neglected.

The model of dilutely distributed non-interacting inhomogeneities is a starting point for more accurate description accounting for a mutual interaction of inhomogeneities, such as the Mori-Tanaka scheme [55, 56]. Unlike the scheme of dilute distribution, the Mori-Tanaka model relates the strain in individual inhomogeneities to the average strain in a matrix.

In order to accurately represent complex microstructures, a special attention has been paid to the cases of multilayered particles, discs or penny-shaped cracks. The coating of particles, e.g. a weak zone (ITZ) around aggregates, can be represented in the homogenization schemes using the concentration factors derived by Herve and Zaoui [57]. They found the analytical solution for the elastic strain and stress fields in an infinite medium constituted of a layered isotropic spherical inclusion, embedded in a matrix subjected to uniform stress or strain conditions. The introduction of the crack density parameter, determining the effective properties of solids containing cracks, was accomplished e.g. by Kachanov [58, 59].

An incremental form of the Mori-Tanaka method coupled with a proper description of failure mechanisms, such as plasticity or damage, enables us to evaluate the loading path, and to estimate the material properties of a composite, such as its strength or fracture energy. In the simple case of isotropic damage concentrated exclusively to the matrix phase, the damage parameter is evaluated for each strain increment and after the calculation of the effective composite stiffness tensor, the corresponding macroscopic stress is found [60].

Another approach to effectively estimate the compressive strength in composite materials assumes that only a deviatoric stress is responsible for a failure of the material. Therefore, it is necessary to calculate a norm of the deviatoric stress in individual components, which can be

afterwards compared with a critical stress. Such approach was used Pichler and Hellmich [61] and it turned out to be suitable for upscaling the compressive strength in cement pastes and mortars. However, the post-peak behavior cannot be assessed using this approach [62].

Chapter 2

Microstructure and Mechanical Properties of Lime-Pozzolan Pastes

Based on: V. Nežerka, Z. Slížková, P. Tesárek, T. Plachý, D. Frankeová, and V. Petráňová, Comprehensive Study on Microstructure and Mechanical Properties of Lime-Pozzolan Pastes, *Cement and Concrete Research* 64 (2014) 17–29, doi: 10.1016/j.cemconres.2014.06.006

2.1 Introduction

Today's commercial limes are very pure, even though the regulating standard EN 459-1 is not very strict — the mass of CaO and MgO in the commonly used CL-90 lime hydrate should be higher than 90 %. The presence of impurities in historic lime mortars was not usually harmful [28], the content of silica (SiO_2) and alumina (Al_2O_3), was mainly responsible for their hydraulic character. The reaction between lime and SiO_2 and Al_2O_3 leads to the formation of calcium silicates and aluminates [29]. The contemporary high-purity limes without any additives lack the required durability, strength and suffer from an enormous shrinkage. Therefore, the minerals have to be added to lime in form of pozzolans — in our study we used metakaolin and finely crushed bricks.

Pozzolans, e.g. volcanic ash or crushed bricks, have been used since ancient times in combination with lime to improve the moisture resistance of mortars, resulting in freeze-thaw resistance [9], and also increase their mechanical strength [10, 11] and durability [1, 5]. Mortars with the addition of pozzolans should be able to harden in a high relative humidity (they are called *hydraulic*) or when the access of CO_2 is limited as in case of mortars supporting glazed tiles [5]. Crushed ceramic material from tiles, bricks and pottery was added to lime-based mortars since the Byzantine period [4], and crushed bricks in the joints of load-bearing masonry were extensively used in the Roman Empire as the pozzolanic material where no volcanic material was available [14]. Such mortars were also preferred from the early Hellenistic to early Byzantine times in water-retaining structures to protect the walls from moisture, typically in baths, canals and aqueducts [16, 17]. While fine brick particles were mainly used for rendering,

larger crushed brick particles appeared mainly in masonry walls, arches and foundations [18]. The mortars containing crushed bricks were known as *Horasan* in Turkey [63], *Surkhi* in India, *Homra* in Arabic countries [64], and *Cocciopesto* in Roman times [15].

In recent years, the understanding of cement-based materials has been significantly promoted by their micromechanical modeling. Analytical and numerical homogenization have been used for stiffness prediction of alkali-activated pastes [65], upscaling the compressive strength of Portland cement mortars [61], or multi-scale simulations of three-point bending tests of concrete specimens [60]. Based on their work, a similar approach for the lime-based mortars was proposed by Nežerka and Zeman [24]. The last study revealed that a realistic model of lime-based composites needs to incorporate the properties of pure paste and processes taking place in the matrix, such as shrinkage.

Despite a considerable amount of literature devoted to the lime-based mortars, the authors are not aware of any work dealing with pure lime pastes — the available studies usually focus on specific properties of mortars containing aggregates. In particular, they deal with their use and performance in ancient structures [15, 18, 35], their chemical composition [29, 66] and influence of pozzolans [1, 4, 5, 14], morphology of the individual phases [1, 42, 43, 67], porosity [38, 40, 68], or mechanical properties [5, 27, 28, 29].

The aim of the study presented in this Chapter is to fill the gap by performing a systematic study on lime-based pastes, with emphasis on their microstructure, porosity and mechanical properties. Information on the chemical composition and grain size distribution of individual components used for the preparation of pastes can be found in Section 2.2, where the reader can also find the data describing the chemical development, shrinkage and porosity of the investigated pastes. Microscopy images in Section 2.3.5, complemented by SEM-EDX elemental analysis, illustrate the morphology and reactivity of individual components. The development of stiffness, expressed by means of the dynamic Young's modulus, is presented in Section 2.4.1. Data on the compressive strength of individual mixes are contained in Section 2.4.2, followed by the results of tensile testing (Section 2.4.3) and information about the fracture properties in Section 2.4.4.

2.2 Materials

To make our study useful for practical applications, we used only materials commonly available in the Czech Republic, and similar to the materials that can be found within Europe. We provide a detailed specifications in terms of their chemical composition and particle size distribution, see Table 2.1 and Figure 2.1. The chemical composition was determined by means of EDXRF analysis using Oxford Instruments X-Supreme 8000. The particle size was measured using Laser analyzer CILAS 920, by which the materials containing particles of a diameter ranging from 0.3 to 400 μm can be analyzed. Measurement of the specific surface area was done by the gas adsorption, BET method, using the device Micromeritics ASAP 2020. Moreover, metakaolin and crushed bricks were characterized in terms of their pozzolanic activity, which indicates the ability of the pozzolans to react with lime (see Section 2.3.1).

2.2.1 Lime

In our study, commonly available white air-slaked lime (CL90) Čertovy schody, Czech Republic, having a great purity (98.98 % of CaO + MgO) was used. The chemical composition is summarized in Table 2.1 and grading curve is plotted in Figure 2.1. The most frequent particle diameter found in lime was 15 µm, diameter at 50 % was equal to 13 µm and diameter at 90 % to 38 µm. The specific surface area, determined by the gas adsorption, was in the case of lime equal to 16.5 m^2/g.

2.2.1.1 Metakaolin

Metakaolin is obtained by calcination of kaolinitic clays. From the chemical point of view, the metakaolin consists of minerals enabling hydraulic reactions — siliceous content is always high (around 60 %) as well as Al_2O_3 content (around 30 %) [5]. The addition of metakaolin into the mix should result in an enhanced strength of the lime paste and increased durability, while the vapor transport properties should be superior to the case of the Portland cement additions [7].

The metakaolin used in our study was a finely ground burnt claystone with the commercial name Mefisto L05, containing higher amount of alumina at the expense of silica. This pozzolanic material produced by České lupkové závody Inc., Nové Strašecí, Czech Republic, had the particle diameter at 50 % equal to 4 µm, at 90 % to 11 µm, and the specific surface area 12.7 m^2/g. Its main chemical components are summarized in Table 2.1 and its grading curve appears in Figure 2.1.

Table 2.1: Chemical composition of used materials.

	lime	metakaolin	bricks
component	amount [% wt] (±0.5 %)		
CaO	97.8	0.17	3.22
MgO	1.16	0.75	2.69
SiO_2	0.65	52.1	54.1
Al_2O_3	0.00	43.4	25.3
K_2O	0.12	0.66	4.11
Fe_2O_3	0.10	0.85	8.03
TiO_2	0.00	1.87	1.45
SO_3	0.08	0.00	0.00
P_2O_5	0.01	0.00	0.00
Mn_2O_3	0.01	0.00	0.00
SrO	0.01	0.00	0.00

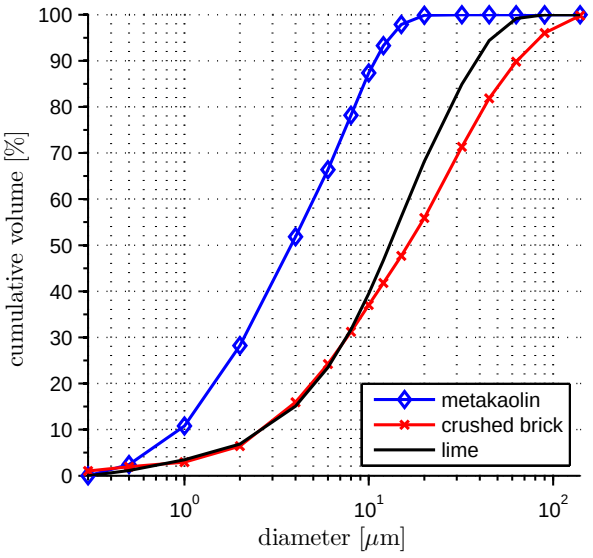

Figure 2.1: Grading curves of individual materials.

2.2.1.2 Crushed Bricks

According to Silva et al. [34], the amorphous components of the crushed brick aggregates are mainly represented by aluminosilicates that are able to react with lime by making the interfacial surface alkaline. This chemical reaction produces calcium-silicate-hydrate (CSH) and calcium-aluminum-silicate-hydrate (CASH) at the brick-lime interface, giving the mortars a hydraulic character. The smaller the particles, the bigger the surface per volume and consequently also the hydraulic reactivity.

In our study, the crushed bricks, made of unfired bricks from a brick factory Štěrboholy in Prague, Czech Republic, were used as an alternative pozzolanic material. They were burnt in a laboratory at the temperature of 750 °C, ground and sieved. It is known that in order to gain the required pozzolanic activity, the ceramic products should be fired at temperatures between 600 and 900 °C [37].

The fraction 0.063–0.120 mm obtained by sieving was used for this study but the exact size of the particles was determined later by the Laser analyzer. It brought slightly different characteristics of the grain size distribution: diameter at 50 % was equal to 16 μm and diameter at 90 % to 64 μm, see Figure 2.1. This was due to the fact that the burnt brick grains were dispersed in water, causing a disintegration of the imperfectly sintered material. Similar effects may be expected also during the preparation of pastes or mortars, when the crushed brick particles are in contact with water and mechanically disintegrated by mixing. The chemical composition of crushed bricks used in our study is summarized in Table 2.1. Compared to metakaolin, crushed bricks had slightly bigger specific surface area, 15.6 m^2/g, which is caused by their scalloped morphology.

Table 2.2: Specific surface area.

	specific surface area [m^2/g] ($\pm$0.3 %)
lime	16.5
metakaolin	12.7
crushed bricks	15.6

2.2.2 Prepared and Tested Samples

Altogether nine different compositions of lime-based pastes were prepared and investigated. The first paste (L) was composed of pure lime and used as a reference mix. Lime-metakaolin pastes (MK-1 – MK-4) contained lime and metakaolin only, in the mass ratios lime to metakaolin equal to 9:1, 8:2, 7:3, and 6:4. Finally, the pastes containing lime and crushed bricks (CB-1 – CB-4) were prepared in the mass ratios lime to crushed bricks equal to 9:1, 8:2, 7:3, and 6:4.

Based on our experience with the lime-based materials, the amount of water in all mixes was adjusted in such a way to ensure the workability of the pastes while keeping the water to dry mass ratio as low as possible to avoid shrinkage cracking, see Table 2.3.

The pastes were cast into prismatic molds with dimension of 40×40×160 mm and removed after 6 days. During casting, the pastes were slightly compacted using a shaking table in order

Table 2.3: Summary of prepared mixes.

mix	constituents			water / dry mass	flow test results
	lime	metakaolin	crushed bricks		[cm]
L	100 %	–	–	0.823	13.0×13.1
MK-1	90 %	10 %	–	0.773	13.8×13.6
MK-2	80 %	20 %	–	0.759	14.9×14.3
MK-3	70 %	30 %	–	0.778	15.9×15.7
MK-4	60 %	40 %	–	0.773	16.0×15.8
CB-1	90 %	–	10 %	0.782	13.0×13.3
CB-2	80 %	–	20 %	0.758	15.5×15.7
CB-3	70 %	–	30 %	0.771	16.0×15.7
CB-4	60 %	–	40 %	0.694	15.0×15.1

to remove the excessive air bubbles and voids. Curing was executed in the common laboratory conditions, i.e. in the temperature 20±1 °C and relative humidity of 50–60 % with no humidification supporting the hydraulic reactions.

The prismatic specimens were cut into different configurations for individual tests. The dynamic Young's modulus was continuously measured using resonance method on uncut specimens of dimensions approximately 39×39×156 mm (the initial dimensions were reduced due to shrinkage). These specimens were also used for the monitoring of shrinkage. The fracture energy was evaluated from the three-point bending test on notched specimens having the dimensions approximately 19×19×100 mm and the notch depth of 7 mm. This size should be sufficient with respect to the size of inhomogeneities contained in the pastes. The fractured specimens were consequently glued to steel clamps and used for tensile test (see Figure 2.15). The compression test was executed on cubic specimens having the dimensions approximately 39×39×39 mm, prepared from the prismatic specimens used for the testing of the dynamic Young's modulus.

2.3 Chemical Processes and Development of Microstructure

Carbonation is a chemical process during which the slaked lime, $Ca(OH)_2$, reacts in a solution with CO_2 to form calcium carbonate, $CaCO_3$:

$$Ca(OH)_2 + CO_2 \rightarrow CaCO_3 + H_2O \tag{2.1}$$

where the resulting compound is significantly stronger and less soluble than the replaced portlandite. The carbonation process requires the presence of water, since $Ca(OH)_2$ is accessed by CO_2 in its dissolved state [25], and it is always more developed on the surface than in the core of mortar samples [1].

During the hydration process, calcium aluminate and silicate hydrates are formed after activation of the aluminate and silicate phases of pozzolans in the presence of $Ca(OH)_2$ and water [30]. Vejmelková et al. [28] reported that the pure lime mortar without addition of pozzolans exhibited about 10 % higher porosity than those containing metakaolin (20 % of binder

mass). This phenomenon is explained by the formation of hydration products, such as calcium silicate hydrates, C_4H_{13}, C_3AH_6 and C_2ASH_8, as a result of the reaction of silicate and aluminate ions with Ca^{2+} ions [31]. According to many studies, CSH gels and CASH are among the main hydrated phases formed at the room temperature after pozzolanic reaction of metakaolin [30, 32, 33].

2.3.1 Pozzolanic Activity

The pozzolanic activity was assessed using the modified Chapelle test [69, 70]. This method is based on the reactivity of the tested material (in our case the crushed bricks or metakaolin) with calcium oxide (prepared by calcination of $Ca(OH)_2$) in water. The prepared mixture was kept at the temperature of 85 °C for 16 hours. After that time the mixture was filtered and the CaO content was determined by means of sucrose extraction and titration with HCl solution [71]. The solid phase composition was then investigated by the thermogravimetric analysis (TGA). The obtained result — CaO fixed in a solid phase — was adjusted using the TGA data (CaO bound in $Ca(OH)_2$ and $CaCO_3$ was subtracted from the total CaO fixed). The resulting pozzolanic activity, see Table 2.4, is expressed as the amount of $Ca(OH)_2$ fixed by 1 g of pozzolans.

Table 2.4: Pozzolanic activity of metakaolin and crushed bricks.

	$Ca(OH)_2$ fixed by 1 g of pozzolans [mg] ($\pm$2.0 %)
metakaolin	1,002
crushed bricks	337

The results of the measurement, summarized in Table 2.4, clearly indicate that metakaolin reacted with lime more easily than crushed bricks, even though the bricks had been fired at appropriate temperatures (see Section 2.2.1.2), and their chemical composition seems to be perfect for the pozzolanic reaction. This finding is supported by the results of thermogravimetric analysis, see Section 2.3.3. According to Cabrera et al. [66], the pozzolans containing bigger amount of amorphous silico-aluminates, and having particles of small diameter and therefore big specific surface, exhibit high reactivity. This is not confirmed by our study, since the specific surface area of crushed bricks was even higher than in case of metakaolin, Table 2.2, but their pozzolanic activity was significantly smaller.

2.3.2 Weight Development

The hydration products can be detected from a measurement of the weight development, because they bind water during their development. This is obvious from Figure 2.2(a), where the addition of metakaolin resulted in quite significant reduction of weight loss in early age. This water retention was not observed in the pastes containing crushed bricks, indicating a weak pozzolanic reaction.

According to Lanas et al. [29], the pure lime mortars start to gain weight approximately from 28th day. At this time the elimination of excess water is stopped and the carbonation process still takes place. This is in agreement with our measurements, where the pure-lime

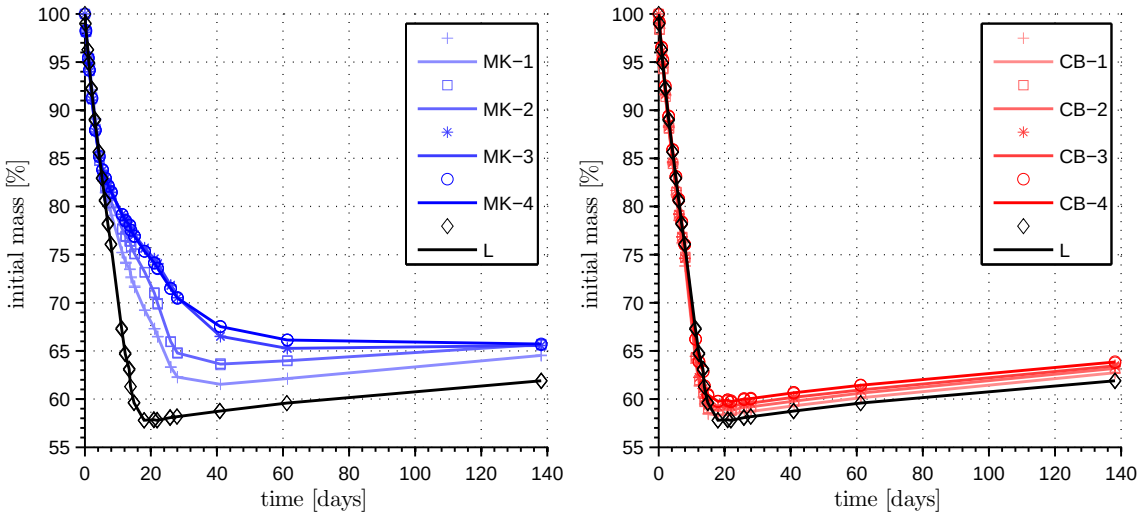

(a) MK and L pastes

(b) CB and L pastes

Figure 2.2: Development of weight in time.

paste samples started to gain weight after about 18 days, see Figures 2.2(a) and 2.2(b). The same phenomenon can be observed in pastes containing crushed bricks, because the hydraulic reactivity of crushed bricks is weak and the effects of carbonation prevail.

From the obtained data a relationship between the mass of dry ingredients (lime powder and pozzolans) and the final product (mortar paste) can be established. The results are summarized in Table 2.5. It can be concluded that the ratio of the final paste mass to the mass of powdered ingredients is about 1.46 in case of MK pastes (the highest water retention), 1.39 in case of CB pastes and 1.45 for L paste.

Table 2.5: Ratios of final paste mass to mass of powdered ingredients.

	L	MK-1	MK-2	MK-3	MK-4	CB-1	CB-2	CB-3	CB-4
mass ratio (±0.5 %)	1.45	1.43	1.46	1.46	1.49	1.38	1.40	1.38	1.40

2.3.3 Thermogravimetric Analysis

The thermogravimetric analysis is based on the measurement of weight loss due to increasing temperature and the quantity of individual phases determines the hydraulicity of the mortar. Since the aggregates are mainly of silicic nature and exhibit no response in TGA, only the binder is analyzed by TGA. From this point of view, the pastes present an ideal sample for the analysis. The following effects can be observed by TGA: i) around 100 °C, release of physically adsorbed (hygroscopic) water; ii) at 200–600 °C, dehydration of hydraulic phases (hydrated aluminates and silicates); iii) at 400–520 °C, dehydration of portlandite ($Ca(OH)_2$); and finally at iv) 700–840 °C, decomposition of calcium carbonate ($CaCO_3$) [72].

For the analysis, a small piece (of about 1 cm^3) from the center of a paste sample was powdered and then the mass of about 20 mg was used for the analysis. TGA was carried out

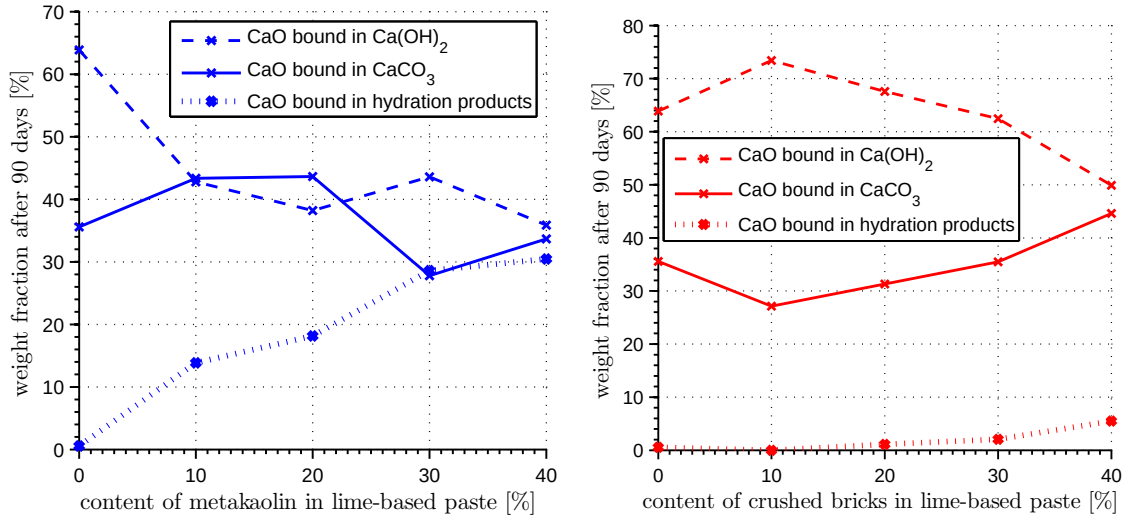

(a) MK pastes (b) CB pastes

Figure 2.3: Results of TGA analysis.

using the equipment SDT Q600 (TA Instruments) in the range of temperatures 25–1,000 °C in the N_2 atmosphere at the heating rate of 20 °C per minute.

In our study we focused on the presence of residual portlandite content, carbonated calcite and water bound to hydration products in the pastes after 90 days of curing — the dependence of their content on the amount and type of pozzolans is depicted in Figures 2.3(a) and 2.3(b). It is obvious that the amount of hydration products is increasing with the amount of pozzolans on the expense of portlandite, while the amount of calcite is almost constant. This is in agreement with Arizzi et al. [1], who claim that the main phases in pure lime pastes are calcite ($CaCO_3$) and portlandite ($Ca(OH)_2$), but the portlandite amount found after only 28 days of carbonation is low, because the part not transformed into calcite (i.e. carbonation) is involved in the lime-pozzolan reactions (i.e. hydration).

Interestingly, the amount of calcite increases with the small additions of crushed bricks, but the higher amount seems to promote carbonation. The high amount of hydration products in the pastes containing metakaolin explains their early stiffness (and probably also strength [5]) gain. A better development of hydration products around crushed brick particles would be probably significantly promoted if the specimens were kept in a wet environment [18].

TGA of ancient Byzantine mortars by Moropoulou et al. [72] revealed an increased content of bound water in the mortars containing crushed brick particles, indicating the presence of hydration products, even though the crushed bricks had usually bigger diameters and played a role of aggregates. It was reported by Moropoulou et al. [35, 41] that mortars containing crushed bricks exhibit self-healing effects due to re-formation of amorphous hydraulic CSH formations, also responsible for a better adhesion between the binder [18]. From our results provided by TGA, the formation of hydration products on the lime-crushed brick interface was very limited, which was confirmed by the SEM-EDX microscopy, see Section 2.3.5.

2.3.4 Porosity

Mercury Intrusion Porosimetry (MIP) was used for the determination of pore size distribution and compared with pycnometric method in order to check whether the pores of all sizes were captured. Using this method, the pores within the sample are filled by mercury under a pressure and its volume is continuously recorded. It is assumed that smaller pores have to be filled under a higher pressure. The limitations of this method were investigated by Stefanidou [73] and Quallet et al. [74], who proved that despite several simplifications the method is sufficiently accurate for lime- and cement-based materials.

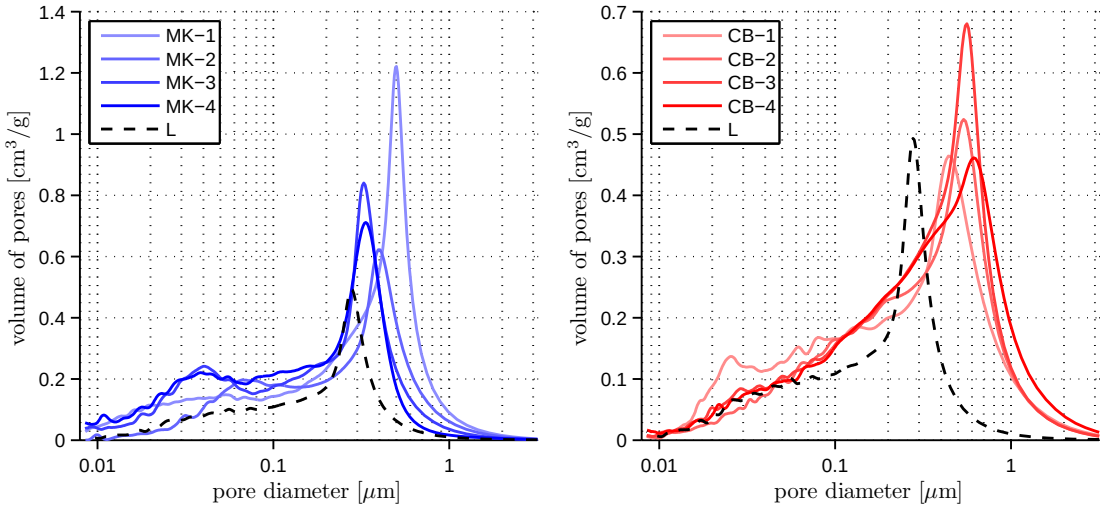

(a) MK and L pastes

(b) CB and L pastes

Figure 2.4: Pore size distribution.

The data were obtained by the Poremaster PM–60–13 Quantachrome instrument, working within the pressure range 0.005–413 MPa. The mercury parameters were set to the values of 480 erg/cm^2 for the surface tension and 140 ° for the contact angle. Concerning the sample size, a small piece (up to 1 cm^3) from the center of the paste sample was investigated. Larger pores with the peak around 100 μm were present in all pastes by less than 10 % and these are not included in the diagrams in Figures 2.4(a) and 2.4(b).

It was expected that the formation of hydration products due to the presence of pozzolans in the pastes would contribute to a reduction of pore radii in comparison with the pure lime paste [42]. Quite surprisingly, it turned out that the addition of crushed bricks increased the radius of pores, see Figure 2.4(b). Just a slight reduction of pores with the addition of pozzolans was observed only in the case of pastes containing metakaolin, see Figure 2.4(a). This supports the findings by TGA, recall Section 2.3.3, that amount of hydration products in the pastes containing crushed bricks was very limited and therefore the radii of pores within these pastes were larger. Interestingly, the porosity of lime-based paste was lowest even though the water to binder ratio during the preparation was high.

The pores are mainly created by replacement of excessive water by air during hardening, forming spherical voids or veins. It has been shown by Arandigoyen et al. [38] that carbonated lime-pastes have two pore size peaks: one peak between 0.5 and 1.0 μm in diameter, varying

Table 2.6: Porosity of individual pastes.

	L	MK-1	MK-2	MK-3	MK-4	CB-1	CB-2	CB-3	CB-4
total porosity [%]	39.56	54.39	55.29	54.57	55.95	54.31	51.62	53.34	53.13
diameter at peak [μm]	0.286	0.507	0.413	0.333	0.348	0.471	0.552	0.538	0.648

according to kneading water used in mortar preparation, and a smaller peak between 0.1 and 0.2 μm, independent of the water content in the fresh mortar. This finding can be neither confirmed, nor disproved by our study, since the latter peak is not very distinctive.

Arizzi and Cultrone [1] found that the main peak in pore size distribution curves obtained in lime and metakaolin-based mortars corresponds to pores having the radius between 0.1 and 1.0 μm and their volume has the major impact on the total porosity of mortars. This is in agreement with our study, see Table 2.6. Frias et al. [75] reported that the peak of pores having the diameter in the range between 0.02 and 0.2 μm can be observed in the hydraulic mortars due to the presence of metakaolin forming the network of hydrated calcium silicates. These hydration products have, according to Pandey et al. [68], the diameter of pores in range between 0.02 and 0.08 μm. That was confirmed by our measurements, where the second peak was emerging with the addition of metakaolin approximately at 0.04 μm.

2.3.5 Microscopy Investigation

The microstructure of the pastes was analyzed with Scanning Electron Microscopes (SEM) MIRA II LMU produced by Tescan Corporation (Brno, Czech Republic), equipped with the energy dispersive X-ray detector (EDX), manufactured by Bruker Corporation (Berlin, Germany). The polished specimens were coated with a thin layer of carbon in order to increase the conductivity necessary for a high resolution of the images.

Figures 2.5(a) and 2.5(b) present Backscattered Scanning Electron Microscopy (BSE) images of the lime paste microstructure. Figure 2.5(a) illustrates the lime grains having the size 10–50 μm, which are the most frequently occurring in the sample area. The shape of the grains is more angular, which provides an evidence about the lime product milling. Finer particles of size under 10 μm fill the space between the larger lime grains. The investigated grain size distribution very well corresponds with the results of Laser Particle Size Analysis, see Figure 2.1. Figure 2.5(a) shows a drying crack passing through a few larger grains, while Figure 2.5(b) presents the same lime paste at a higher magnification, focusing at the microstructure of the finer lime grains.

The microstructure of the lime-metakaolin paste MK-4 is illustrated in Figures 2.6(a) and 2.6(b). The metakaolin plates (dark gray) of the size mainly around 5 μm are visible in the detailed image of the microstructure in Figure 2.6(a). These plates surround a bigger lime grain of the size approximately 25 μm (the white lump in the center). The disintegration of the lime grain indicates a reaction with metakaolin and water within the period of 120 days after the paste preparation. The microstructure with even distribution of lime (light gray particles) and metakaolin (gray area) can be seen at a lower magnification in Figure 2.6(b). The black inclusions represent traces of grains which disappeared during the section lapping and the white grains are overburnt lime inclusion. The microstructure of the paste containing crushed bricks,

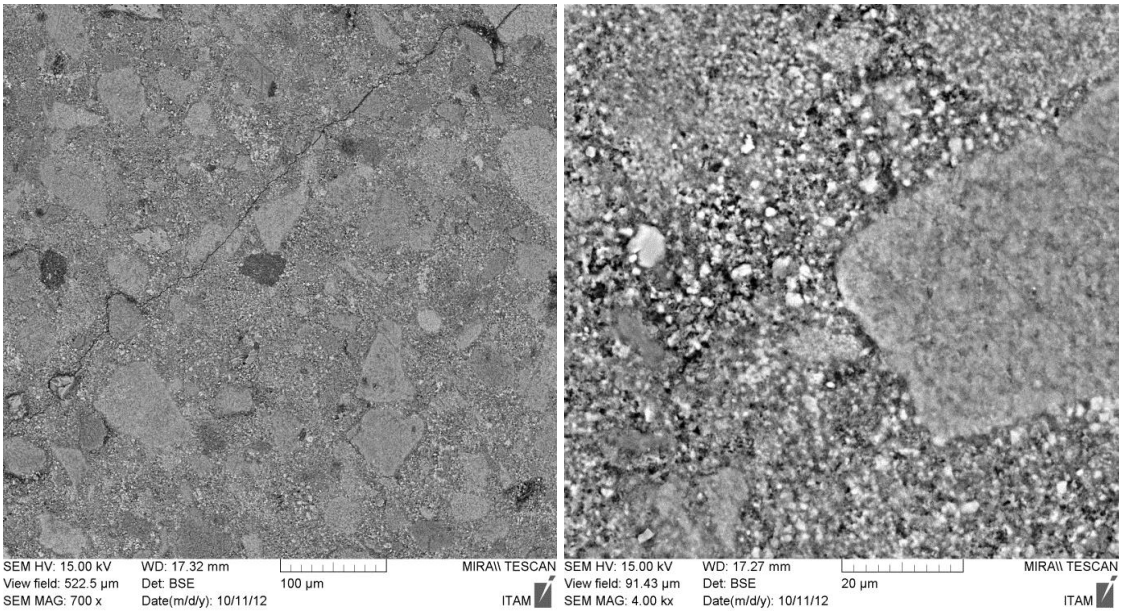

(a) magnified 700×, showing well graded sub-angular particles of lime (light grey)

(b) magnified 4000×, detail of bigger lime grain (on right) surrounded by finer lime particles

Figure 2.5: SEM-BSE image of hardened paste L.

CB-4, is shown in Figures 2.7(a) and 2.7(b). The crushed brick grains of nearly the same size as lime, but having different structure, can be observed in Figure 2.7(a). It seems that in case of MK pastes the increasing content of metakaolin leads to an increasing occurrence of disintegrated lime grains. This phenomenon was not found in CB pastes.

Elemental mapping by SEM-EDX was utilized to study the reaction between constituents in the pastes and distribution of Ca, Al and Si elements within the investigated areas. Figures 2.8(a), 2.8(b) and 2.8(c) show the microstructure and elemental composition of MK-4 paste. An overburnt compact lime grain in the center, surrounded by more disintegrated lime lumps, was captured in the microstructure image. Figure 2.8(b) shows the presence of Ca in lime particles (red color). The presence of Al and Si in metakaolin particles (turquoise blue) and Si (blue) in disintegrated lime particles, except the central compact lime grain, was detected in Figure 2.8(c). From the investigation of all MK pastes it seems that the Si content in the area of the lime grain is related to the extent of disintegration of lime grain, compact lime grains are not actively involved in the pozzolanic reaction. Different behavior was found in CB pastes, where the interaction between the lime and crushed brick particles was not detected by EDX mapping. Figures 2.9(b) and 2.9(c) document the composition of lime grains, consisting of Ca element only (without Si marks), while elemental composition of brick grains is based purely on Si and Al.

2.3.6 Shrinkage

The measurement of volume changes was performed using a digital caliper. It revealed that their rate is strongly dependent on the presence and type of pozzolans, as can be clearly seen in Figures 2.10(a) and 2.10(b).

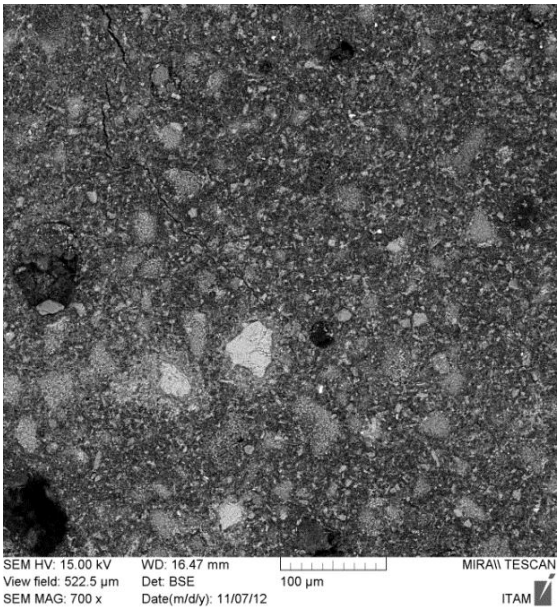

(a) magnified 700×, microstructure with voids from section lapping (black) and overburnt lime inclusions (white)

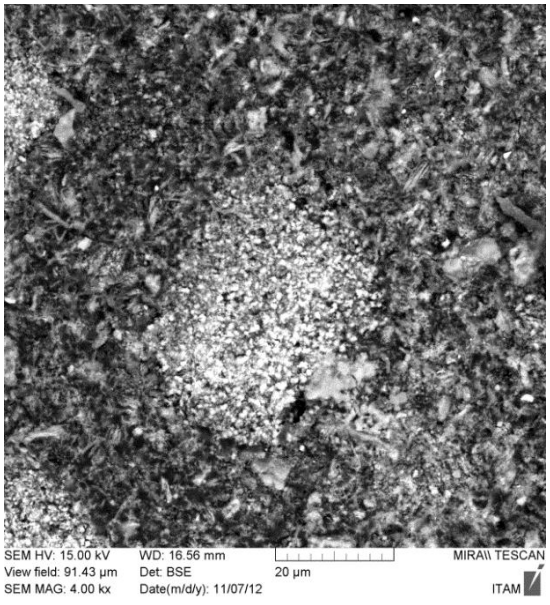

(b) magnified 4000×, detail of porous disintegrated lime grain surrounded by metakaolin flaky particles

Figure 2.6: SEM-BSE image of hardened paste MK-4.

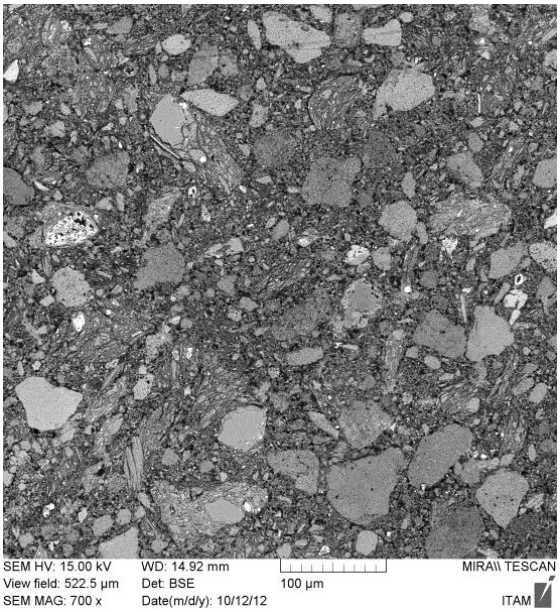

(a) magnified 700×, sub-angular lime grains surrounded by elongated flaky clay brick particles

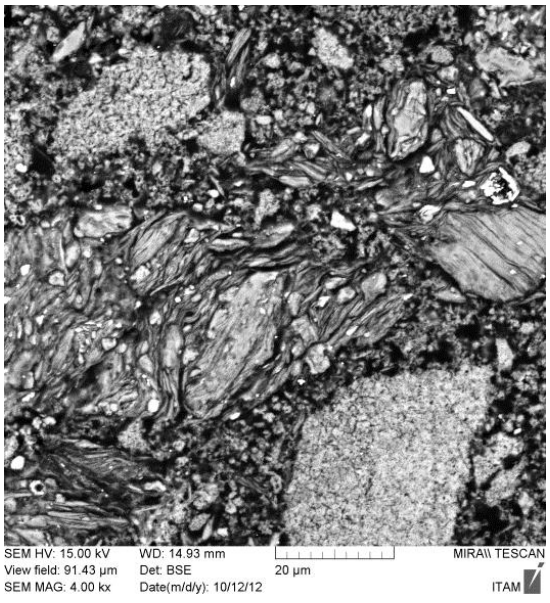

(b) magnified 4000×, detail of lime lump (granulated) surrounded by laminated brick particles

Figure 2.7: SEM-BSE image of hardened paste CB-4.

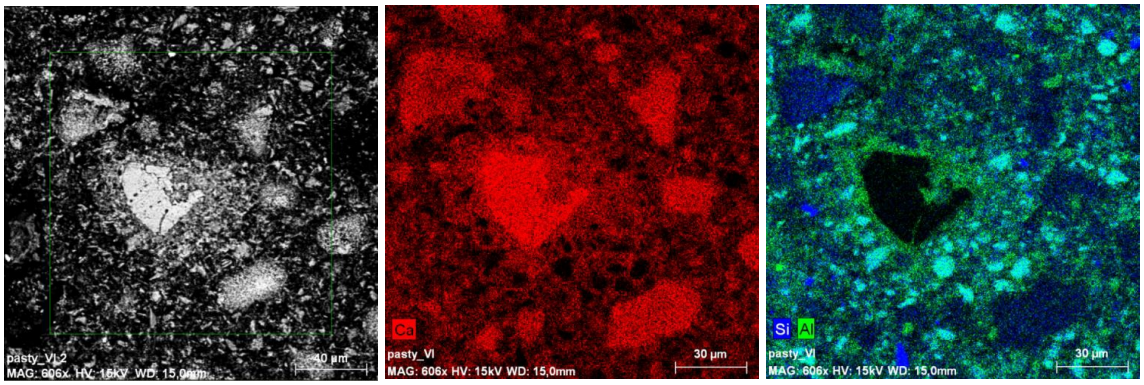

(a) overburnt and unreacted lime inclusion surrounded by disintegrated lime grains

(b) distribution of Ca (red) element

(c) distribution of Al (green) and Si (blue) elements

Figure 2.8: SEM-BSE image of hardened paste MK-4, magnified 606×.

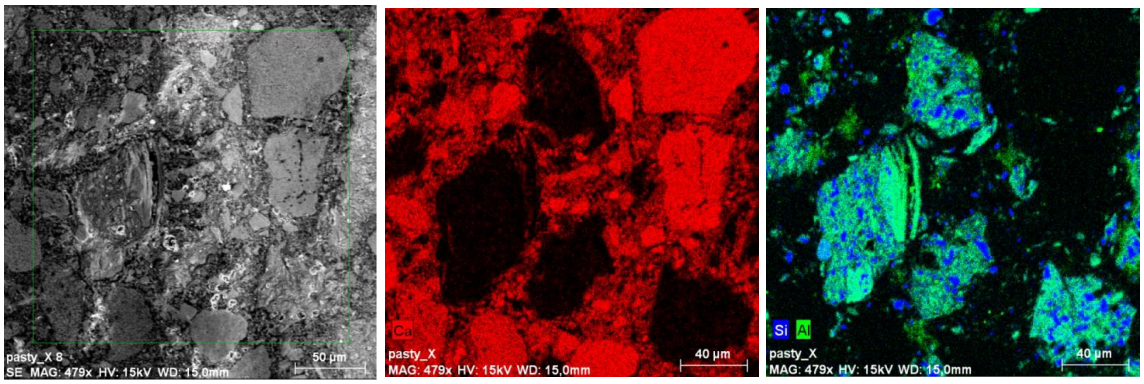

(a) microstructure with lime and brick grains

(b) distribution of Ca (red) element

(c) distribution of Al (green) and Si (blue) elements

Figure 2.9: SEM-BSE image of hardened paste CB-4, magnified 479×.

The volume of specimens was stabilized at approximately same age of about 28 days. The addition of pozzolans results in a significant reduction of shrinkage, which is in agreement with Silva et al. [34], who investigated the influence of fine ceramics in cement-based mortars and found that its additions improve mechanical properties and contribute to a reduction of the mortar shrinkage. It is obvious from our measurements that the shrinkage of lime-metakaolin pastes was much smaller than in case of lime-crushed brick pastes; the measured average values are summarized in Table 2.7.

The reduced shrinkage of mortars containing pozzolans can explain their enhanced strength — the high shrinkage of pure lime matrix pastes causes microcracking around aggregates [22, 76, 77], and the presence of cracks causes a strength and stiffness reduction as reported e.g. in [28]. According to Mosquera et al. [40], clearly visible cracks can be observed in case of pure lime mortar, unlike in case of hydraulic mortars.

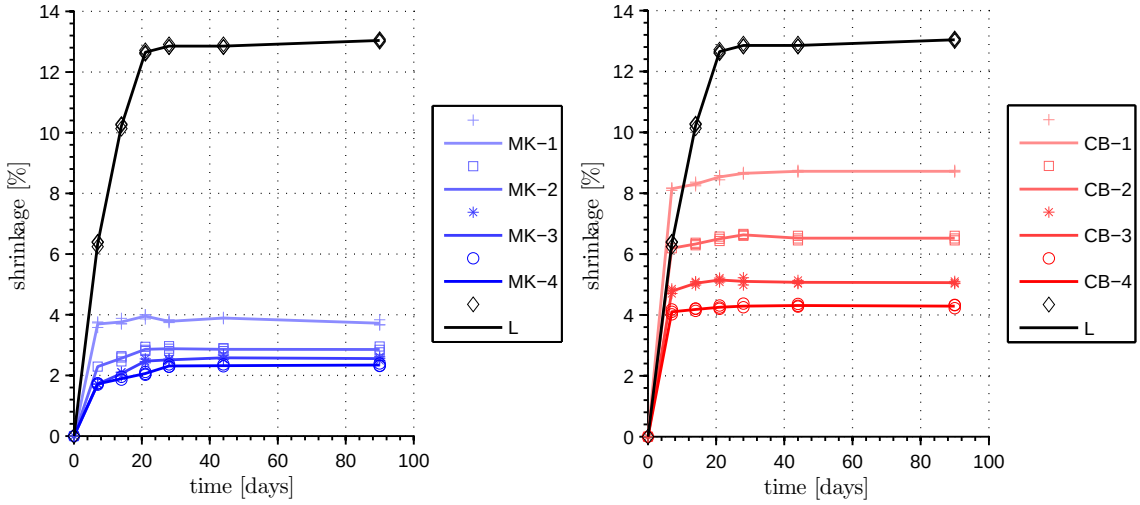

(a) MK and L pastes

(b) CB and L pastes

Figure 2.10: Development of shrinkage.

Table 2.7: Shrinkage development in lime-based pastes.

mix	shrinkage [%] (±0.1 %)					
	7 days	14 days	21 days	28 days	44 days	90 days
L	6.34	10.22	12.65	12.85	12.85	13.04
MK-1	3.69	3.76	3.95	3.78	3.89	3.72
MK-2	2.29	2.56	2.86	2.88	2.86	2.85
MK-3	1.71	2.06	2.47	2.51	2.58	2.55
MK-4	1.72	1.89	2.06	2.31	2.32	2.34
CB-1	8.14	8.30	8.53	8.65	8.72	8.72
CB-2	6.19	6.33	6.50	6.63	6.52	6.52
CB-3	4.78	5.04	5.15	5.10	5.07	5.06
CB-4	4.10	4.18	4.25	4.29	4.31	4.29

2.4 Mechanical Properties

The mechanical properties were investigated on specimens described in Section 2.2.2. The presented results of the destructive methods (compressive strength, fracture energy) are relatively scattered. This is probably due to presence of eigenstrains, caused by a non-uniform chemical development and shrinkage, which made these samples vulnerable to microcracking. These microcracks often govern the performance of the specimens when subjected to loading.

Using the non-destructive resonance method we were able to track the evolution of the dynamic Young's modulus, E_{dyn}. We also attempted to extract the values of the static Young's modulus, E_{stat}, from the stress-strain diagrams obtained during the compression test, but we found these values to be inaccurate due to compliance of the testing machine and boundary effects at the contact with the compression plates. If needed, the static modulus can be estimated using the results available for similar materials. In particular, Rosell and Cantalapiedra [78] determined the relationship between Young's moduli of cement-based mortars from a static and

dynamic impact test as $E_{\mathrm{dyn}} = 1.17E_{\mathrm{stat}} - 1,800$ [GPa], and Malaikah et al. [79] claimed that the $E_{\mathrm{dyn}}/E_{\mathrm{stat}}$ ratio is in the range between 0.9 to 1.1.

2.4.1 Dynamic Young's Modulus

The measurement of the dynamic Young's modulus, E_{dyn} [Pa], by the resonance method is based on the equation for a longitudinal vibration of the beam with a continuously distributed mass and free-free boundary condition, from which it follows that

$$E_{\mathrm{dyn}} = \frac{4Lmf_{\mathrm{I}}^2}{bt} \tag{2.2}$$

where L is the length of the specimen [m], m is the mass of the specimen [kg], f_{I} is the fundamental longitudinal resonant frequency of the specimen [Hz], b is the width of the specimen [m] and t is the thickness of the specimen [m]. For additional details on the experimental procedure and data processing, we refer the reader to [80, 81].

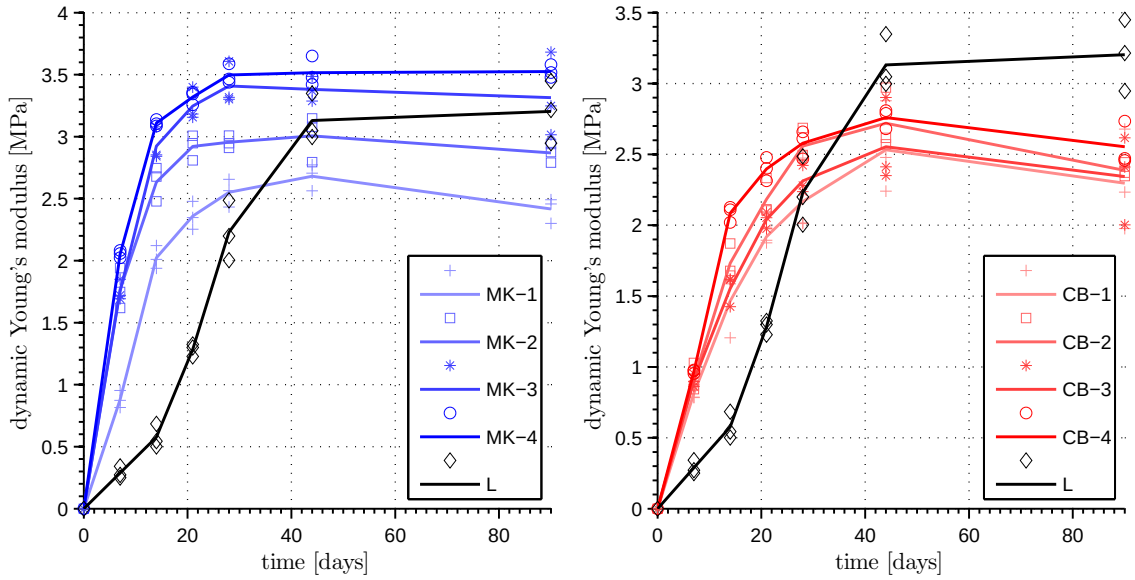

(a) MK and L pastes

(b) CB and L pastes

Figure 2.11: Development of Young's modulus.

The results of our measurements can be seen in Figures 2.11(a) and 2.11(b). The average dynamic Young's moduli with the coefficient of variation from individual measurements are summarized in Table 2.8. The results show that the stiffness development in the pure lime pastes is slower than in case of pastes containing metakaolin or crushed bricks. However, after 90 days of carbonation the pure lime paste reaches relatively high values of the dynamic Young's modulus.

The observed early stiffness gain in the pastes containing pozzolans is probably coupled with the early strength gain, which is in agreement with the conclusions reported in literature, e.g. [1, 10, 11]. We assume that the early stiffness gain in the pastes containing metakaolin is caused by the formation of hydration products, while the accelerated stiffness gain in the pastes

Table 2.8: Development of dynamic Young's modulus in lime-based pastes.

mix	average dynamic Young's modulus [GPa] (coefficient of variation [%])					
	7 days	14 days	21 days	28 days	44 days	90 days
L	0.29 (4.8)	0.58 (9.6)	1.28 (5.0)	2.23 (24.2)	3.13 (19.0)	3.20 (25.1)
MK-1	0.88 (6.9)	2.02 (9.2)	2.36 (11.2)	2.55 (11.2)	2.68 (10.7)	2.42 (10.1)
MK-2	1.77 (16.2)	2.63 (13.9)	2.92 (10.2)	2.96 (5.0)	3.01 (18.7)	2.87 (7.5)
MK-3	1.75 (8.4)	2.92 (13.4)	3.25 (13.3)	3.41 (17.2)	3.38 (10.0)	3.31 (33.9)
MK-4	2.05 (3.0)	3.11 (2.6)	3.32 (5.5)	3.50 (8.0)	3.52 (12.0)	3.53 (5.2)
CB-1	0.82 (5.1)	1.46 (22.4)	1.92 (6.0)	2.17 (26.6)	2.53 (32.2)	2.30 (35.5)
CB-2	0.91 (10.0)	1.73 (12.2)	2.18 (13.0)	2.56 (11.2)	2.72 (21.9)	2.39 (5.1)
CB-3	0.90 (4.4)	1.55 (11.1)	2.04 (6.0)	2.31 (9.7)	2.55 (30.2)	2.34 (31.2)
CB-4	0.97 (1.3)	2.08 (5.7)	2.40 (8.2)	2.58 (9.9)	2.76 (6.9)	2.55 (15.6)

containing crushed bricks is promoted by the absorption of the excessive water by the brick particles, since the hydraulic reactions in CB pastes were negligible, recall Sections 2.3.3 and 2.3.5.

Our measurements agree with the study by Veiga and Carvalho [47], who found that the stiffness and strength from the age of 28 days to the age of 90 days in the case of lime-metakaolin mortars decreases. The same phenomenon was observed by Vejmelková et al. [28] — they found that the highest values of the flexural strength were reached after 28 days in case of lime-metakaolin mortars, while in the case of pure lime mortars the strength was continuously increasing. Similar results of early strength gain, followed by a slight reduction of strength (compressive and flexural) and stiffness were also reported by Giavarini et al. [48].

2.4.2 Compressive Strength

The compressive test was carried out on the cubic specimens using LabTest 4.100SP1 device. The flat lateral sides, being in contact with mold during preparation, were loaded in order to ensure a uniform contact and uniform distribution of the compressive force. The compressive strength was calculated as the ratio of the maximum force reached during the testing to the loaded area. The loading was displacement-controlled with a rate of 0.3 mm/min.

The dependence of the paste strength on the content of pozzolans can be seen in Figure 2.12, and the typical stress-strain diagrams of the pastes are illustrated in Figure 2.13. The additions of metakaolin up to 30 % of the binder mass had rather negative effect on the compressive strength of the pastes, probably due to introduction of inhomogeneities into the material. However, the increase of compressive strength in mixes containing 40 % of metakaolin was remarkable. On the other hand, the addition of crushed brick particles did not contribute to a compressive strength increase. The average values of the measured compressive strength, together with the coefficient of variation from individual measurements, are summarized in Table 2.9.

Vejmelková et al. [28] concluded that in comparison with pure lime mortars a remarkable improvement of mechanical properties can be achieved if 20 % is replaced by metakaolin, the compressive strength increased up to five times. They also found that the water vapor diffusion coefficient decreased about 25 % in comparison with pure lime mortar, indicating

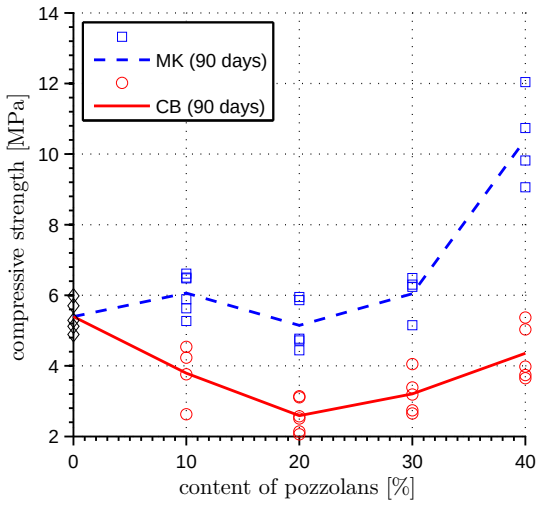

Figure 2.12: Dependence of paste compressive strength on content of pozzolans.

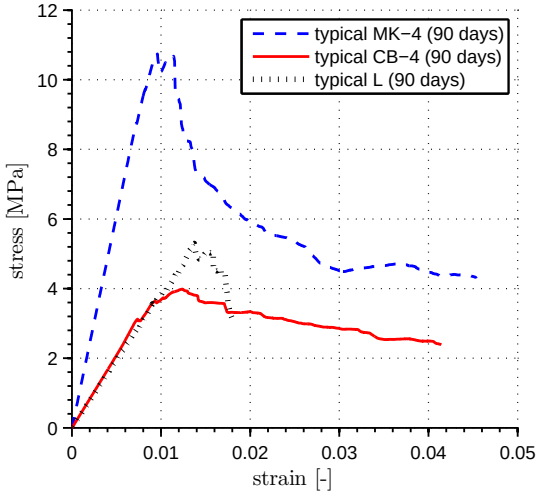

Figure 2.13: Typical stress-strain diagrams of MK-4, CB-4 and L pastes in compression.

Table 2.9: Compressive strength of lime-based pastes after 90 days of curing.

mix	average compressive strength [MPa] (coefficient of variation [%])				
	0 % pozzolan	10 % pozzolan	20 % pozzolan	30 % pozzolan	40 % pozzolan
MK pastes	5.40 (44.1)	6.06 (55.0)	5.15 (70.3)	6.04 (60.6)	10.42 (128.3)
CB pastes	5.40 (44.1)	3.79 (83.7)	2.59 (46.1)	3.20 (56.4)	4.35 (79.1)

the formation of microcracks. In our study, the pastes containing metakaolin were not much stronger compared to the pure-lime ones. This supports the idea that the shrinkage cracking around aggregates in pure lime mortars without additions of pozzolans is responsible for the increased permeability and reduced mechanical strength.

2.4.3 Tensile Strength

The tensile test was carried out on the prismatic samples using LabTest 4.100SP1 device. Special extensions had to be glued to the specimens to avoid lateral compression from the machine clamps, and to ensure a uniform contact and distribution of the tensile force. The tensile strength was calculated as the ratio of the maximum force reached during the testing to the loaded area. The loading was displacement-controlled with a rate of 0.1 mm/min.

The dependence of the paste strength on the content of pozzolans can be seen in Figure 2.14. Quite interestingly, the highest tensile strength was observed in pure lime paste specimens, and any other addition of pozzolans resulted in its reduction. The failure of the specimens was brittle, as expected, due to absence of any reinforcing aggregates within the pastes. The average values of the measured tensile strength, together with the coefficient of variation from individual measurements, are summarized in Table 2.10.

The strength reduction of lime-based pastes with the additions of pozzolans is similar to the measurements of e.g. Cizer et al. [82], who reported that the additions of Portland cement in

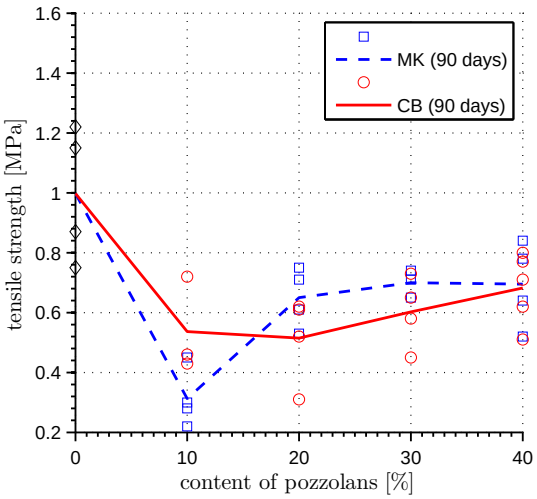

Figure 2.14: Dependence of paste tensile strength on content of pozzolans.

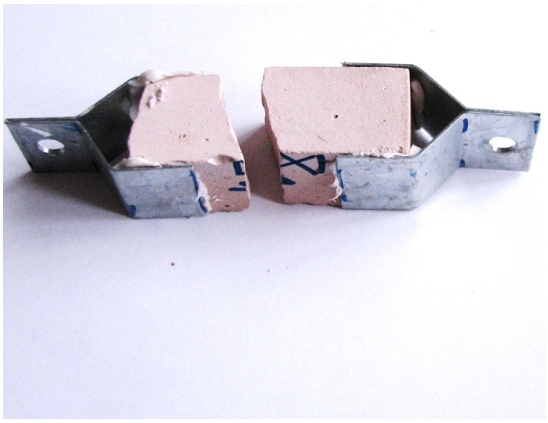

Figure 2.15: Damaged specimen equipped by steel extensions after tensile test.

Table 2.10: Tensile strength of lime-based pastes after 90 days of curing.

mix	average tensile strength [MPa] (coefficient of variation [%])				
	0 % pozzolan	10 % pozzolan	20 % pozzolan	30 % pozzolan	40 % pozzolan
MK pastes	1.00 (22.4)	0.31 (9.8)	0.65 (9.9)	0.70 (4.6)	0.69 (14.4)
CB pastes	1.00 (22.4)	0.54 (15.9)	0.52 (14.4)	0.60 (11.9)	0.68 (11.8)

small amounts into lime-based mortars also caused a flexural strength reduction. This might be explained by the inhomogeneous structure of the binder and differential hardening, resulting in development of non-uniform strain field.

2.4.4 Fracture Energy

The measurement of fracture energy was carried out using MTS Alliance RT 30 kN test machine on the simply supported notched beams with a span of 80 mm. The experiment was displacement-controlled directly above the notch with a rate of 0.025 mm/min, as we attempted to capture the descending part of the load-displacement diagram.

The fracture energy, G_F [J/m^2], was evaluated directly from the continuously recorded load-displacement diagram using the RILEM approach, assuming the balance between external energy and work of fracture dissipated during cracking of simply supported notched beam [83]:

$$G_F = \frac{W_{int}}{b(h - a_0)} \tag{2.3}$$

where W_{int} is the work of fracture [Nm], equal to the area under the force-displacement curve, b is the width of the beam [m], h is its height [m], and a_0 is the notch depth [m]. The authors are aware of the size-dependence when using this approach (see e.g. [84, 85, 86]), however, since no energy dissipation due to plastic deformation at the crack tip can be expected and the size of inhomogeneities is small compared to the size of the tested specimens, the method should

provide reasonably accurate results.

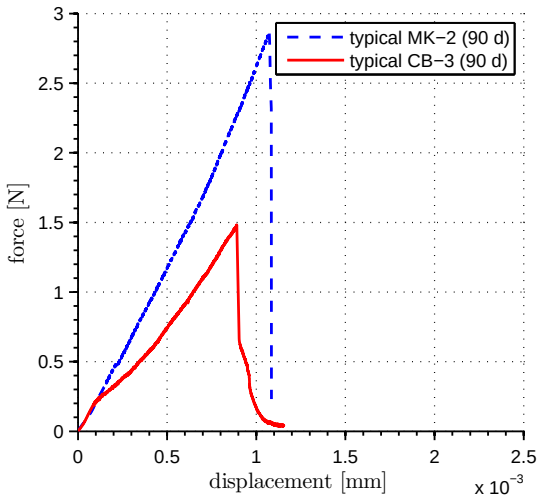

Figure 2.16: Typical load-displacement diagrams of MK-2 and CB-3 pastes in three-point bending test on notched beams.

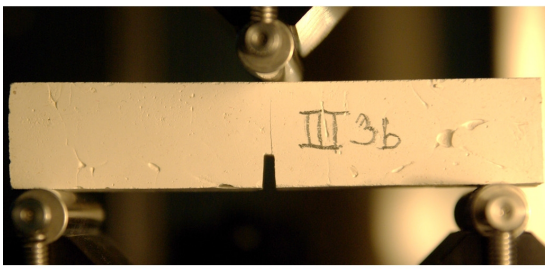

Figure 2.17: Three-point bending test on notched beams made of MK paste.

The typical load-displacement diagrams can be seen in Figure 2.16, however, they cannot be perfectly compared in this form, because the tested specimens had slightly different dimensions due to shrinkage. It is clear that the descending part of the load-displacement diagram was not captured correctly, since the fracture energy, G_{F}, needed for the material splitting into two parts was consumed during the elastic deformation and no softening was present.

Therefore, the only conclusion that can be made from the measurement is that lime-based pastes are extremely brittle material and sensitive to any stress concentrations near defects. The brittleness of the pastes caused that an abrupt collapse of the specimen could be triggered by a tiny crack, which is reflected by a large dispersion of the measured data, see Table 2.11. These findings fully justify the use of aggregates in mortars, acting both as a reinforcement and barrier against the crack propagation. The value of the fracture energy can be correctly measured only by controlling the crack opening displacement, but this was not possible to accomplish on this type of material with the available experimental apparatus.

Table 2.11: Upper limit of fracture energy of lime-based pastes after 90 days of curing.

mix	fracture energy [J/m^2] (coefficient of variation [%])				
	0 % pozzolan	10 % pozzolan	20 % pozzolan	30 % pozzolan	40 % pozzolan
MK pastes	14.31 (368.5)	10.76 (131.6)	16.50 (321.3)	17.13 (575.4)	21.37 (582.2)
CB pastes	14.31 (368.5)	13.88 (114.2)	9.01 (245.1)	6.21 (56.2)	14.41 (69.7)

The obtained results are in agreement with the findings of Nishikawa et al. [87] who investigated the fracture-mechanical properties of cement pastes without aggregates. They concluded that any inclusion, even unhydrated clinker within the paste, can increase the energy needed for the crack propagation.

2.5 Conclusion

The investigation of lime-pozzolan pastes provided valuable results and findings unbiased by the presence of aggregates. The information contained in this Chapter can be further used in a modeling or design of lime-based mortars that are nowadays used for repairs of cultural heritage.

Metakaolin proved to be much more reactive pozzolan than crushed bricks, which is in accordance with the pozzolanic activity test results. The pozzolanic reaction in the pastes containing metakaolin was confirmed by the development of weight during hardening, TGA and also the porosimetry indicated the presence of hydration products in these pastes. The SEM-BSE microscopy gave a clue about the microstructure of the samples and its development — the disintegration of metakaolin and lime particles suggested their reaction. Elemental mapping by SEM-EDX clearly demonstrated the integration of Si from metakaolin grains in lime and, on the contrary, unreacted crushed brick particles.

The shrinkage was significantly reduced by the presence of pozzolans, mainly in the case of metakaolin additions. The presence of pozzolans also accelerated the stiffness gain, which was reflected by the results of dynamic Young's modulus measurements. However, the tensile and compressive strengths were not enhanced by the low additions of pozzolans, which is probably caused by the presence of eigen stresses from a non-uniform chemical evolution, and development of stiffness and shrinkage. The three-point bending test on notched specimens revealed almost perfect brittleness of the pastes.

These findings explain the increase of strength in lime-based mortars containing pozzolans — since the observed strength enhancement of the pastes with the addition of pozzolans is not significant (if any), the reduced shrinkage is probably the main benefit, resulting in reduced cracking around aggregates. The increased shrinkage cracking in mortars without pozzolans is probably responsible for the shift of pores to bigger radii, which was not observed in case of pure-lime pastes without aggregates.

Chapter 3

Investigation of Crushed Brick-Matrix Interface

Based on: V. Nežerka, J. Němeček, Z. Slížková, and P. Tesárek, Investigation of Crushed Brick-Matrix Interface in Lime-Based Ancient Mortar by Microscopy and Nanoindentation, *Cement & Concrete Composites* 55 (2015) 122–128, doi: 10.1016/j.cemconcomp.2014.07.023

3.1 Introduction

Powdered ceramic material was used as a pozzolanic material since the early Hellenistic period. The Romans added crushed bricks into the mortar when there was no volcanic material available [15]. Crushed bricks were frequently added into the lime-based mortars during the Byzantine period [4], and these were preferred in water-bearing structures and to protect the walls from moisture, typically in baths [88], canals and aqueducts [16, 17]. It has been reported in a few papers [35, 36, 42] that a thin layer of hydration products forms around the crushed ceramic particles if the clay is fired at appropriate temperature between 600 and 900°C so that the clay minerals can gain the pozzolanic activity [37]. Based on the mineralogical composition, it was only assumed that the layer of hydration products strengthens the composite and improves the bond with the surrounding matrix. However, due to the limited thickness of the interfacial transition zone (ITZ), conventional testing methods cannot be used for investigation of its mechanical properties and to prove this hypothesis.

The purpose of the work presented in this Chapter was to investigate the boundary of crushed brick fragments and ITZ between the surrounding lime-based matrix, and to asses the elastic properties of ITZ by nanoindentation. This method, originally developed for testing of homogenous materials, is now widely used also for quantification of mechanical properties of various composites including cement or lime based mortars.

Among others, nanoindentation had been recently exploited by Hughes and Trtik [89] for assessment of micromechanical properties of cement paste, Constantinides and Ulm [90] utilized nanoindentation to determine the elastic modulus of high and low density C-S-H gel, and

Němeček et al. [91] exploited the grid nanoindentation for identification of individual phases in cement pastes and aluminium alloys, and Tesárek et al. [92, 93] used similar technique for identification of phases in gypsum. Statistical analysis is mostly employed for the analysis of multi-phase structural materials [94, 95]. An indirect approach was used by Neubauer et al. [96], who determined the elastic properties of interfacial transition zone (ITZ) around aggregates in concrete by fitting the microstructural model to experimental data.

3.2 Materials

The investigated sample was extracted from the apse of a late Byzantine church built approximately in the 9^{th} century AD in the district Üsküdar, located in Istanbul, Turkey. The sample of the bedjoint mortar contained pieces of crushed bricks, which represented the main type of the aggregate, Figure 3.1(a). Beside the brick fragments, the mortar contained also particles of porous slag, polycrystalline quartz, and grains of laminated and micritic carbonate (calcite). The binder to aggregate ratio in the investigated mortar sections was approximately equal to $2 : 3$ by volume as provided by the image analysis performed on area approximately 20×20 mm.

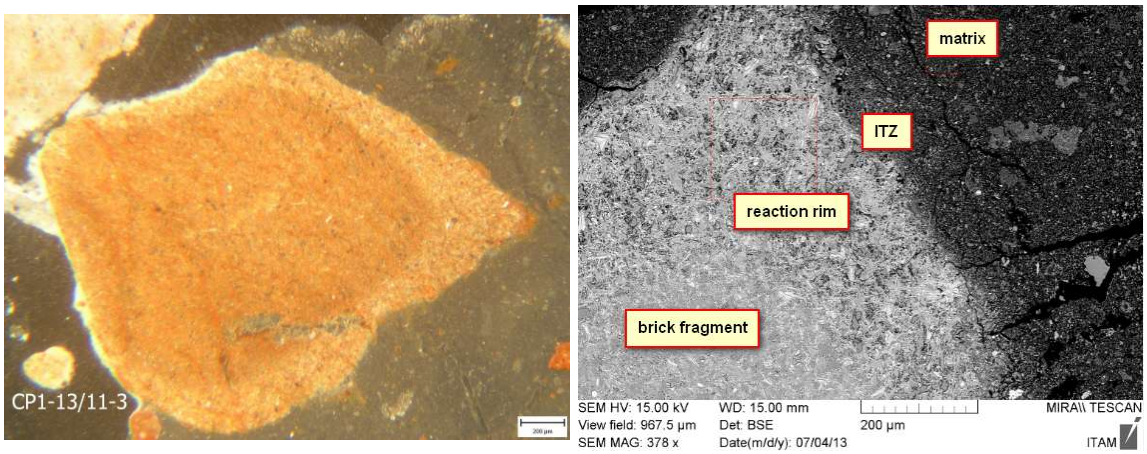

(a) brick grain surface texture with a reaction rim of various thickness (RPL), magnified 500×, scale bar = 200 µm

(b) SEM-BSE micrograph of brick fragment boundary, magnified 378×

Figure 3.1: Presence of reaction rims at boundary of crushed brick particle.

The chemical composition of the mortar sample was investigated by means of the Scanning Electron Microscopy / Energy Dispersive X-ray Spectroscopy (SEM-EDX) and the results are summarized in Table 3.1. The analysis was focused on the composition of the lime-based matrix, the unreacted core of crushed brick fragments (dark center of the brick fragment in Figure 3.1(a)), reaction rim formed at their boundary (light colored in Figure 3.1(a)) and ITZ around the fragments; the location of individual phases is indicated in Figure 3.1(b).

The results summarized in Table 3.1 were obtained as an average of several area measurements on areas of about 150×150 µm at distinct locations within individual phases. Approximately 20 analyses were performed for each phase (brick, reaction rim, ITZ and matrix) on

Table 3.1: SEM-EDX analysis of mortar components.

	matrix	ITZ	brick reaction rim (light)	unreacted brick (dark)
component	amount [% wt] (±2.0 %)			
CaO	57.1	57.3	36.3	15.6
SiO_2	31.0	34.5	39.9	56.8
Al_2O_3	8.72	8.81	10.2	14.8
MgO	1.50	1.26	3.42	1.31
K_2O	-	-	1.74	2.87
Na_2O	-	-	0.37	3.64
FeO	-	-	7.29	4.99
TiO_2	-	-	1.53	0.53
SO_3	1.17	-	0.66	-

the surface of 3 polished thin mortar sections. The matrix phase was chemically most homogeneous, while the brick fragments exhibited the highest variations in terms of the elemental composition.

3.3 Morphological and Chemical Analyses

Thin sections of the mortar samples were investigated by petrographic microscopy (Zeiss NU2 microscope) and scanning electron microscopy (SEM). Petrographic microscopy (PM) in linear polarized light mode, under crossed polars (XPL) and reflected polarized light (RPL) was used to analyze the general texture of the mortar and the reaction patterns. For higher resolution imaging and micro chemical analysis SEM was utilized. The SEM study in backscatter mode and micro chemical analysis with an energy dispersive x-ray detector (EDX) attached to the SEM were performed using MIRA II LMU device produced by Tescan Corporation with EDX by Bruker Corporation. The polished sections were coated with a thin layer of carbon in order to increase the conductivity necessary for a high resolution of the images.

The crushed brick aggregate was composed of fragments having their size in the range 0.5–12 mm with sub-angular surface texture and various red color shades. Some brick grains showed reaction rims indicated by the changes of red color in PM (Figure 3.1(a)) and reduced porosity revealed by SEM (Figure 3.1(b)). Based on the PM and SEM image analysis, the thickness of the rims was established as 100–200 µm. The chemical composition of the distinct phases was investigated separately and the results are summarized in Table 3.1.

The matrix phase was intensively cracked and it is represented mainly by a grey-green color in the PM images, see Figure 3.2(a). Its composition, determined by SEM-EDX analysis, is relatively homogeneous and can be classified as eminently hydraulic lime, see Table 3.1. Figure 3.2(a) also shows the calcium carbonate particles, represented by the brown area at the top of the figure. These particles were not present in a high concentration and consisted mainly of CaO (93 %), which was determined by SEM-EDX.

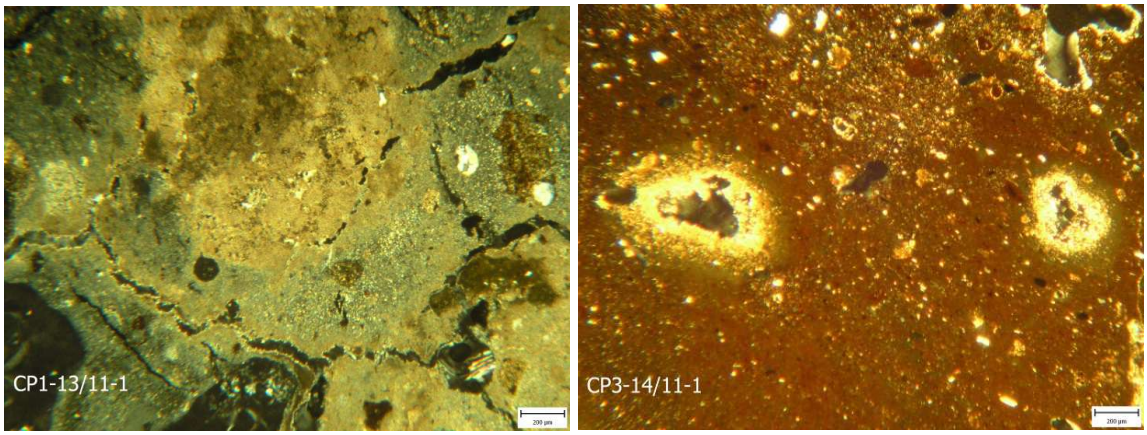

(a) Detail of cracked mortar binder (XPL), magnified 500×, scale bar = 200 µm

(b) Brick structure with oval pores partially filled with yellow clay and new minerals growing in the cavities (RPL), magnified 500×, scale bar = 200 µm

Figure 3.2: Texture of crushed bricks and surrounding matrix.

Beside crushed bricks, the mortar contained also some other particles as grey porous isotropic slags, volcanic rocks with porphyric structure (Figure 3.3(a)), grains of polycrystalline quartz (Figure 3.3(b)), carbonates with polysynthetic lamination (Figure 3.3(c)) and grains of micritic carbonate. However, the reaction rims were observed only at the boundary of crushed brick fragments.

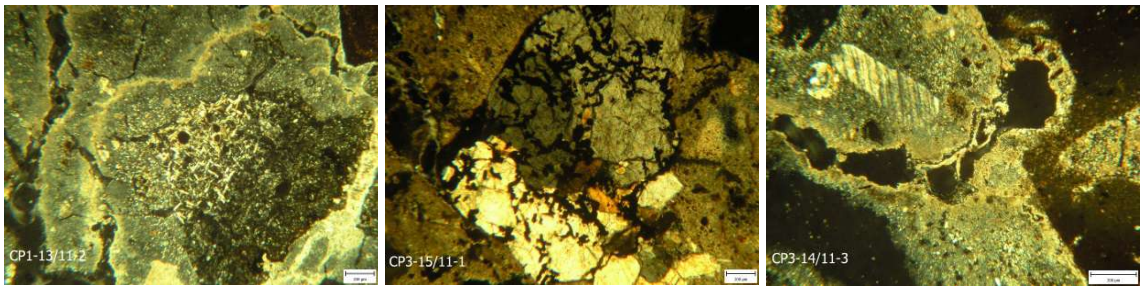

(a) volcanic rock (center) and black isotropic slag (right), scale bar = 300 µm

(b) polycrystalline quartz grain in mortar binder, scale bar = 300 µm

(c) grain of carbonate with polysynthetic lamination (upper part), scale bar = 300 µm

Figure 3.3: XPL analysis of non-brick aggregates.

The main attention of the present study was paid to the interface (ITZ) between the lime-based matrix and crushed brick particles which is assumed, as expected from other studies, to have a significant influence on the mortar mechanical performance [24, 96]. Probably multiple reasons positively influenced the development of the reinforced ITZ and reaction rims at the boundary of crushed brick fragments. Namely, these are wet environment, which is crucial for the activation of pozzolans and formation of hydration products [5, 16, 17], the suitable mineralogical composition of matrix and crushed particles rich in aluminosilicates [66] (see

Table 3.1), and also the mortar age [97].

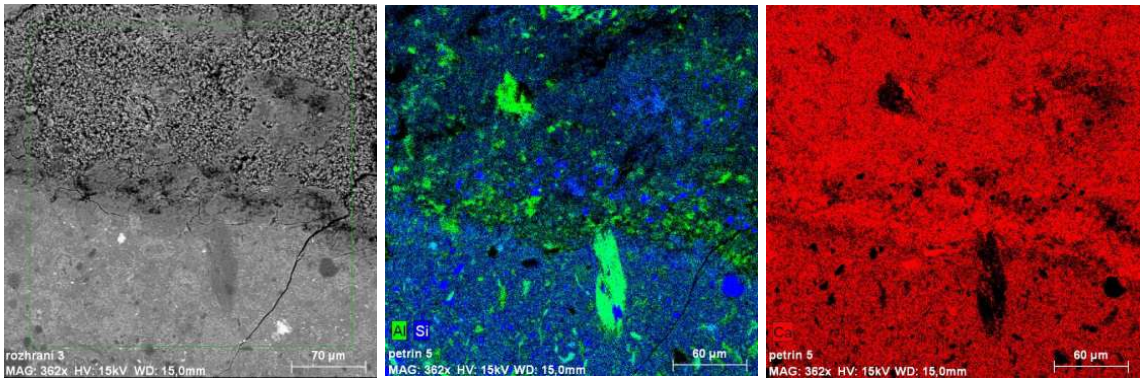

(a) Interface between brick (bottom) and matrix (top), scale bar = 70 µm

(b) Al and Si (green and blue) distribution around ITZ, scale bar = 60 µm

(c) Ca (red) distribution around ITZ, scale bar = 60 µm

Figure 3.4: BSE image and SEM-EDX elemental maps, magnified 634×.

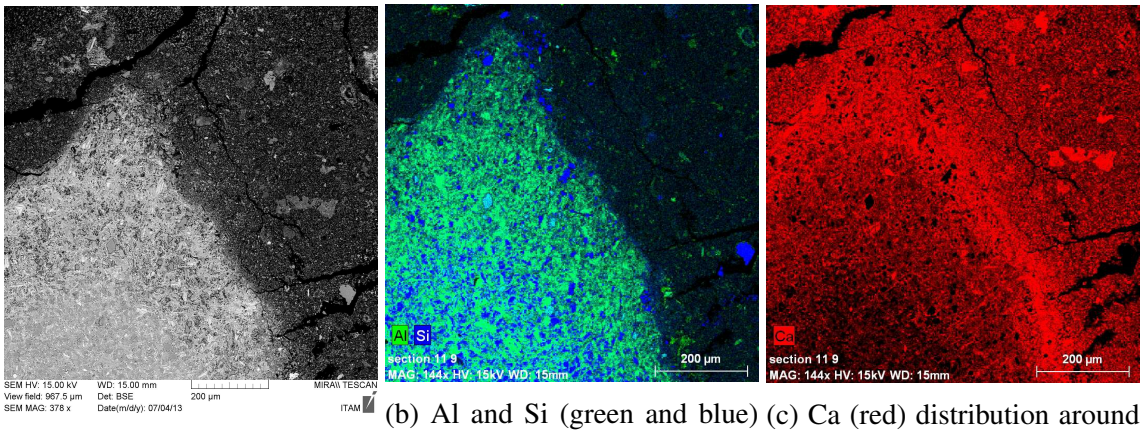

(a) Interface between brick (bottom) and matrix (top), scale bar = 200 µm

(b) Al and Si (green and blue) distribution around ITZ, scale bar = 200 µm

(c) Ca (red) distribution around ITZ, scale bar = 200 µm

Figure 3.5: BSE image and SEM-EDX elemental maps, magnified 634×.

Elemental mapping by SEM-EDX was utilized to study the distribution of basic elements in composite components and reaction compounds. With respect to the inhomogeneous chemical composition of the individual phases, mainly the distribution of elements present in the highest concentrations (Ca, Al and Si) is discussed. As the content of Si an Al decreases from bricks to the matrix, an opposite trend was found in the case of Ca distribution. Beside these elements, the mortar matrix was relatively rich in magnesium and sulphur, and unlike in the case of brick fragments and reaction rims, the presence of alkali elements (Na and K) was not detected. Fe element was not present in the matrix phase and its distribution within brick fragments was highly nonhomogeneous.

The change in concentration of CaO and aluminosilicates (SiO_2 and Al_2O_3) within a section through the matrix and brick fragment is indicated in Figure 3.1(b). Figures 3.4 and 3.5 show

the microstructure and elemental composition of the brick-binder interface. The elemental maps revealed an aluminium and silicon enrichment in the interface area as a result of the hydraulic reaction between the both components, Figures 3.4(b) and 3.5(b). The Ca element is present in relatively high concentrations within the reaction rim (Figure 3.5(c)), due to filling of voids by CaO. These findings support the hypothesis of calcium silicates and aluminates formation within the ITZ and reduction of pore radii at the boundary of brick fragments, which is in accordance with other studies [34, 42, 43].

3.4 Nanoindentation

Micromechanical properties of ITZ were studied by means of nanoindentation. Nanohardness tester (CSM Instruments, Switzerland) equipped with Berkovich (pyramidal) diamond tip was utilized for all measurements. The instrument is capable of performing indentations located in pre-defined positions via coupled optic system with ≈ 0.5 μm precision and with maximum load capacity 500 mN.

The sample was sectioned and mechanically polished prior to the measurement. A series of abrasive SiC papers with grits down to #4,000 were used. Suspension containing 0.25 μm diamond particles was applied in the final polishing stage and all the dust and free particles were removed from the surface of the samples by alcohol and simultaneous action of an ultrasonic bath.

A suitable ITZ location with minimum roughness was selected optically before the measurement. Several rectangular grids, each containing three parallel rows of indents, were placed at the brick-matrix interface. The size of individual indents and their spacing within the grid were chosen to minimize their mutual influence but to capture the gradient of mechanical behavior. The penetration depth of individual indents had to be chosen relatively large in order to avoid the influence of roughness, which is relatively high compared to e.g. more compact cementitious composites. The total area covered by a single indentation grid was prescribed to be 70×21 μm (with the larger dimension directed perpendicular to the interface). The spacing of indents was set to 7 μm in both directions. The arrangement of indents is illustrated in Figure 3.7.

Load controlled quasi-static indentation test was employed for all imprints within the grid. Loading function containing three segments (constant loading at 24 mN/min, holding period 10 s, and unloading at 24 mN/min) was used for each location and maximum load was set to 2 mN. The holding period was included to reduce creep effects on the elastic unloading [98]. The penetration depth varied depending on the stiffness of the indented phase.

Relatively large stiffness of the brick caused small penetration depths of indents (≈ 270 nm) in this part of the indentation grid. The penetration depth increased in matrix as the stiffness was decreasing from the brick interface. An average indentation depth outside the brick phase reached ≈ 900 nm. The penetration depth is associated with the affected indentation volume from which mechanical response is obtained. It must be understood that the mechanical stiffness obtained from indentation tests includes also all inhomogeneities in this volume (including porosity). Thus, the elastic constants received from the tests must be treated as effective values of the indentation volume, and the effective depth influenced by the indenter tip can be roughly

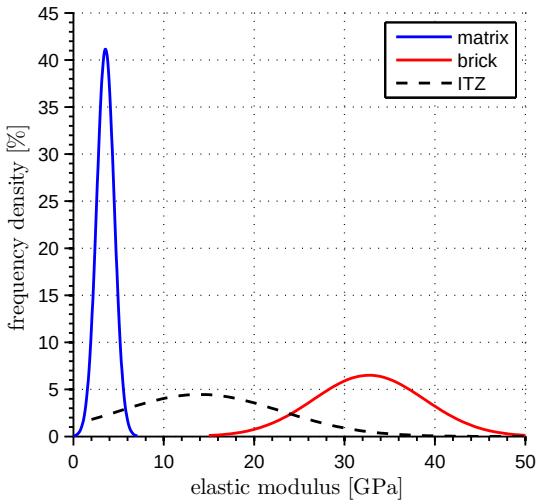

Figure 3.6: Gauss distributions of Young's modulus in matrix and brick fragments.

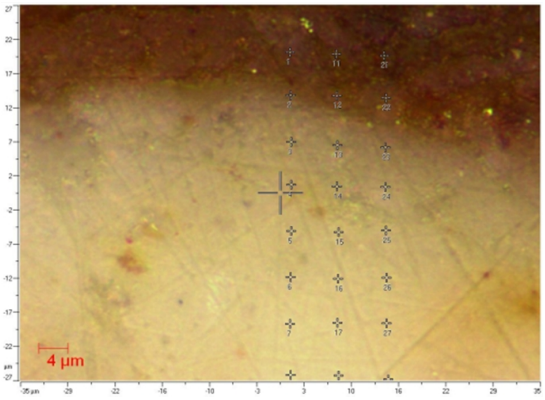

Figure 3.7: Detail of ITZ with prescribed indents locations as seen in optical microscope (brick at top), scale bar = 4µm.

estimated as three times the penetration depth which yields ≈ 2.7 µm.

According to Arizzi and Cultorne [1] the majority of pores present in hydraulic lime mortars is having their diameter in range between 0.01 and 0.1 µm. This has been supported by the findings by Lawrence et al. [39] who claim that the pores having the diameter approximately 0.1 µm are formed in all lime-based mortars, since these are attributed to the transformation of portlandite ($Ca(OH)_2$) to calcite ($CaCO_3$). The hydraulic mortars have generally their pores shifted towards smaller radii around 0.03 µm [13, 28, 29]. This is in agreement with our measurement based on mercury intrusion porosimetry (MIP), which indicated that all the pores within the sample were having the diameter lower than 0.9 µm and the highest frequency was found for pores of diameter equal to 0.5 µm. From this point of view the effective nanoindentation depth about ≈ 2.7 µm ensured sufficient volume of the material to include all pores in the micrometer range that are detectable by MIP.

The typical example of indentation loading curves corresponding to different components, i.e. the matrix, brick fragment and ITZ, are depicted in Figure 3.8. It is clear from Figure 3.8 that the stiffest response (characterized with the steepest unloading slope of the curve) is represented by the brick phase, ITZ is characterized with an intermediate stiffness, and the matrix is the most compliant part of the composite.

Each indent was evaluated by using the Oliver and Pharr methodology [99] which utilizes the unloading part of the indentation curve for the assessment of the material elastic modulus. From an experiment, the indentation (reduced) modulus is received as:

$$E_r = \frac{1}{2\beta}\frac{\sqrt{\pi}}{\sqrt{A}}\frac{\mathrm{d}P}{\mathrm{d}h} \tag{3.1}$$

in which P is the indentation force, h is the penetration depth, $\frac{\mathrm{d}P}{\mathrm{d}h}$ is the contact stiffness, β is a geometrical factor introduced to correct non-symmetrical shape of an indenter (1.0 for a

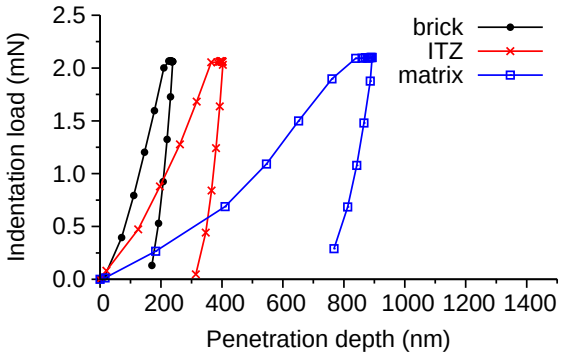

Figure 3.8: Typical examples of loading diagrams obtained at different locations within matrix by nanoindentation.

spherical tip, 1.034 for Berkovich indenter) and A is a projected contact area of the indenter. The reduced modulus is then converted to Young's modulus of the tested material from the series combination of plane strain moduli of the two bodies in contact (i.e. the sample and the indenter) as:

$$\frac{1}{E_r} = \frac{(1-\nu^2)}{E} + \frac{(1-\nu_i^2)}{E_i}, \tag{3.2}$$

where ν is Poisson's ratio of the measured material, and E_i and ν_i are elastic modulus and Poisson's ratio of the indenter, respectively.

Table 3.2: Young's modulus of matrix and brick fragments.

	matrix	brick	ITZ
satisfactory indents	30	46	21
mean Young's modulus [GPa]	3.6	32.7	18.4
C.O.V. [%]	27.3	18.7	63.8

Constant Poisson's ratio representing the indented phases, and equal to 0.2, was considered within the evaluation, also assuming isotropic character of the indented phase. Quite consistent results from all tested locations were obtained and no major differences occurred among the grids. Elastic moduli were averaged from respective positions in a grid and the resulting evolution of elastic stiffness in ITZ can be seen in Figure 3.9. It is characterized by a steep decrease from the brick modulus (average $\approx$ 32.7 GPa) to the average matrix modulus (3.6 GPa). The gradient of the stiffness occurs in a narrow 20–30 μm band at the brick phase. The width of this stiffness gradient agrees well with SEM images providing the information about the thickness of reaction rims.

Independent nanoindentation measurements were also performed on pure brick and matrix phases at regions located in sufficient distance from the ITZ using the same loading conditions. Elastic parameters of the distinct phases were characterized with high variations which is typical of these highly inhomogeneous materials. The parameters are summarized in Table 3.2 together with the results of the measurements in the expected location of ITZ, in the distance 0–30 μm from the interface of brick fragments. The Gaussian distributions of Young's moduli evaluated from individual indents within matrix and brick fragment are depicted in Figure 3.6.

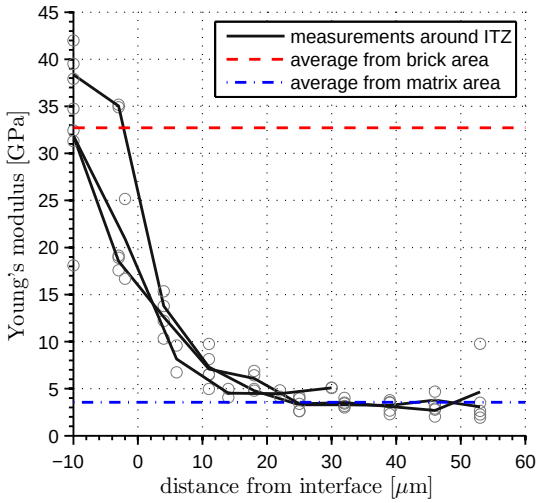

Figure 3.9: Development of elastic stiffness around brick-matrix interface.

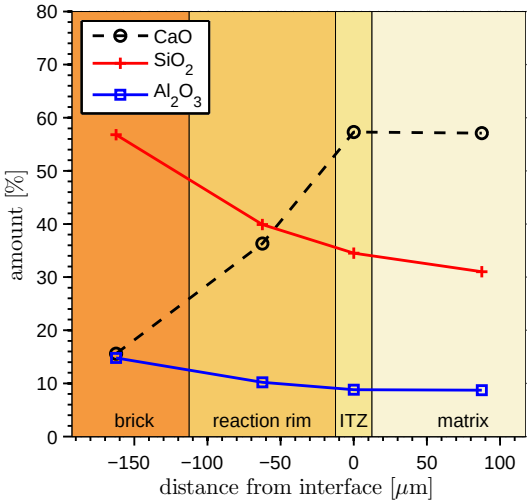

Figure 3.10: Amount of calcite and aluminosilicates in individual phases.

The development of Young's modulus in dependence on the distance from the brick interface can be seen in Figure 3.9 and it is complemented by Figure 3.10 showing the development of element distribution in individual phases.

3.5 Results and Discussion

The investigated sample of the ancient mortar consisted of brick fragments, slag, some other rocks grains and the predominantly hydraulic lime binder. The amorphous components of the crushed brick aggregates are generally mainly represented by aluminosilicates, which react with lime because the lime makes the interfacial surface alkaline. Resulting products of the chemical reaction, taking place at the interface between ceramic particles and the lime-based matrix, are calcium silicate hydrate (CSH) and/or calcium-aluminate-hydrate (CAH), giving the mortars a hydraulic character [34]. This was confirmed by SEM and PM analyses , where the reaction rims of the thickness 100–200 μm at the boundary of brick fragments and the reinforcement of ITZ in the thickness of 20–30 μm were observed.

Similar study was performed by Moropoulou et al. [35] in depth over a range of 120 μm, going from a matrix to a brick phase and considering the interface in thickness ranging from 30 to 50 μm. It revealed the following significant features: Ca element decreases, while Si and Al compounds increase from mortar matrix to brick. This was confirmed by our study, in which the CaO filling the pores of crushed brick fragments in the thickness up to 200 μm was observed, and the presence of aluminosilicates at the expense of the calcium was detected within ITZ in the thickness approximately 20–30 μm. That confirms the idea of Moropoulou et al. [42] that the lime penetrates into the ceramic and the consequent reaction transforms the microstructure of the ceramic by reduction of pore radii. However, in the case of large sized brick pebbles, the reaction cannot penetrate very far into the pebble and the reaction can only result in a better adhesion between the binder and the aggregate [18].

The reduction of porosity and the slightly higher amount of aluminosilicates within ITZ have an impact on its mechanical properties and influence the mechanical properties of mortars, as provided by micromechanical studies, e.g. [19, 57]. Therefore, the stiffness of ITZ was investigated by means of nanoindentation, providing the information about the stiffness of the matrix, brick fragments and the interface between these two distinct phases. Relatively high scatter of the results indicates that both phases are highly inhomogeneous, but distinct enough to capture their boundary. There was clearly observed ITZ, represented by the gradient of measured stiffness, located in a narrow, 20–30 μm, band at the boundary of brick fragments. It is in a perfect agreement with the results provided by SEM-EDX analysis.

It was reported that mortar samples containing crushed bricks exhibit self-healing effects thanks to the presence of the amorphous hydraulic calcium-silicate-hydrate (CSH) formations [35]. This idea is supported, beside SEM-EDX analysis, by the results of our nanoindentation measurements, yielding the stiffness of ITZ (18.4 GPa) similar to the stiffness of low-density CSH found in cement pastes [94, 98].

Moropoulou et al. [41] suggested that the presence of CSH gels could contribute to the increased resistance of cocciopesto mortars to earthquakes, since they require a higher energy absorption without initiations of fractures. According to our measurement the formation of hydration products reinforces ITZ and contributes to a better adhesion between the brick fragments and the surrounding matrix, unlike in case of inert sand particles, where ITZ is weakened by the presence of shrinkage-induced cracking [21]. However, the growth of hydration products at the interface of the ceramic fragments requires suitable composition of ceramic clay, adequate firing temperature, wet environment to promote the reaction and also a significant amount of time [13].

3.6 Conclusion

This Chapter provides a coupled micromechanical and chemical study on ITZ between fragments of crushed bricks and the surrounding matrix in historic lime-based mortar containing crushed brick particles. The sample from the late Byzantine church built approximately in 9-th century in the district Üsküdar, located in Istanbul, Turkey, was used for the analysis.

It has been suggested by many authors that the brick-matrix interface is characterized by the formation of hydration products and it was assumed that this fact can explain the remarkable earthquake resistance and durability of masonry structures having cocciopesto as the bed-joint mortar.

In our work, the formation of hydration products and their stiffness at the interface of the crushed brick fragments was at first analyzed by SEM-BSE, and the micro chemical analysis was accomplished by means of SEM-EDX. The SEM analyses revealed the reaction rims with reduced porosity at the boundary of crushed brick fragments in the thickness up to 200 μm due to filling of voids by CaO. The presence of hydration products (aluminosilicates) that reinforce ITZ was also detected in a thickness of 20–30 μm around the fragments, documented by the slight increase in aluminium and silicon compounds.

The Chapter further contains results from mechanical quantification of ITZ investigated by means of grid nanoindentation. It was proven that the interface is reinforced due to increased

elastic stiffness compared to the bulk matrix. It was found that there is a steep stiffness gradient within ITZ, located in a narrow band having the thickness also 20–30 μm. The derived ITZ thickness supports SEM-EDX findings and shows the mechanical enhancement by hydration products in the detected zone. The effect of reduced porosity in this area detected by SEM-BSE further supports the idea of ITZ stiffness enhancement. The average ITZ Young's modulus was approximately 18.4 GPa, which corresponds to the stiffness of low-density CSH found in cement-based composites.

Chapter 4

Micromechanics-Based Simulations of Compressive and Tensile Testing

Based on: V. Nežerka, J. Němeček, and J. Zeman, Micromechanics-Based Simulations of Compressive and Tensile Testing on Lime-Based Mortars, *submitted to Mechanics of Materials* (2015), arXiv:1512.01227

4.1 Introduction

Based on the findings presented in Chapters 2 and 3, the crushed brick fragments are considered rather as an inert aggregate, because the hydraulic reaction, if any, can take place only at the interface between the fragments and surrounding matrix. Moreover, the formation of hydraulic products requires the presence of moisture [31], significant amount of time [35], and ceramic clay fired at appropriate temperatures [97]. Beside the matrix-enhancing additives, the mechanical properties of lime mortars can be also improved by optimizing the amount and composition of aggregates [1, 27, 29], mostly via a time-demanding trial-and-error procedure.

The goal of the work presented in this Chapter was to render the mortar design process more efficient by proposing a simple model for the prediction of basic properties of lime-based mortars in tension and compression. Our developments have been inspired by earlier studies dealing with micromechanics of cement pastes in compression [61] and in tension [60]. The first study by Pichler and Hellmich [61] exploits a two-level homogenization approach combining the self-consistent [100, 101] and Mori-Tanaka [55, 56] schemes and a J_2-based criterion to estimate the compressive strength. In the latter work, Vorel et al. [60] estimated the tensile strength and fracture energy by combining the incremental form of the Mori-Tanaka method at a single-level with the crack band model [102] to account for the distributed matrix cracking. However, the crucial feature missing in both models is the effect of shrinkage-induced cracks that are intrinsic to the mechanical properties of lime-based mortars.

The shrinkage-induced cracking in cement-like materials has been addressed by both modelling and experimental studies. Detailed analytical investigation into shrinkage cracking around

a single cylindrical aggregate was performed by Dela and Stang [22] to estimate crack growth in high-shrinkage cement paste. Behavior of multi-aggregate systems was addressed numerically by Grassl and Wong [77] using a discrete lattice model; their findings were in agreement with the cracking patterns observed by Bisschop and Mier [103]. Backscattered electron microscopy (BSE) confirmed that the lime-based mortars rich in sand suffer from an extensive matrix cracking [27]. Based on these studies and also on our independent experimental investigations [13, 20], we decided to represent the shrinkage cracks as penny shaped polydisperse voids in our homgenization scheme.

Based on these considerations, the model proposed in Section 4.2 operates at two scales, see Figure 4.1. At Level I, we account for the individual components of mortar, such as lime matrix, sand or brick particles, and distributed voids. At Level II, the shrinkage cracks are introduced into the homogenized material from Level I. Details of this procedure are provided in Section 4.2.1, with the goal to estimate initial elastic properties by the Mori-Tanaka procedure at Level I, Section 4.2.1.1, and the dilute approximation at Level II, Section 4.2.1.2. The density and size distribution of the penny-shaped shrinkage cracks are determined from a crack formation criteria, proposed in Section 4.2.1.3 on the basis of three-dimensional finite element analyses of shrinkage-induced cracking between two isolated inclusions. Two extensions of the elastic model are presented next. The strength under stress-controlled uniaxial compression is estimated in Section 4.2.2 on the basis of the J_2 stress invariant in the matrix phase. Under strain-controlled uniaxial tension, Section 4.2.3, we employ the incremental form of the Mori-Tanaka scheme coupled with an isotropic damage constitutive model to estimate the tensile strength and fracture energy.

Having introduced our model, in Section 4.3 we specify the input data for individual components, along with the experimental procedures used to acquire them, and the composition of the tested mortar samples. Section 4.4 is dedicated mostly to the model validation, concluded by the determination of the optimal mix composition. Finally, we summarize our results in Section 4.5 and outline the strategy how to translate them to the structural scale.

In the following text, the condensed Mandel representation of symmetric tensorial quantities is employed, e.g. [104]. In particular, the scalar quantities are written in the italic font, e.g. a or A, and the boldface font, e.g. $\mathbf{a}$ or $\mathbf{A}$, is used for vectors or matrices representing second- or fourth-order tensors. $\mathbf{A}^{\mathrm{T}}$ and $(\mathbf{A})^{-1}$ denote the matrix transpose and the inverse matrix, respectively. Other symbols are introduced later, when needed.

4.2 Model

We consider an RVE occupying a domain Ω, composed of m phases indexed by r at Level I, and penny-shaped shrinkage-induced cracks reflected at Level II. The matrix is represented by $r = 0$ and indexes $r = 1, ..., m$ refer to heterogeneities of spherical shape or spherical shell in the case of interfacial transition zone (ITZ) around sand grains, see Figure 4.1. The volume fraction of r-th phase, having the volume $|\Omega^{(r)}|$, is provided by $c^{(r)} = |\Omega^{(r)}|/|\Omega|$. Note the representation of sand / crushed brick particles by spheres is less realistic then e.g. by ellipsoids [105], but the effect of the introduced errors is minor relative to the accuracy of the input data, cf. Section 4.3.

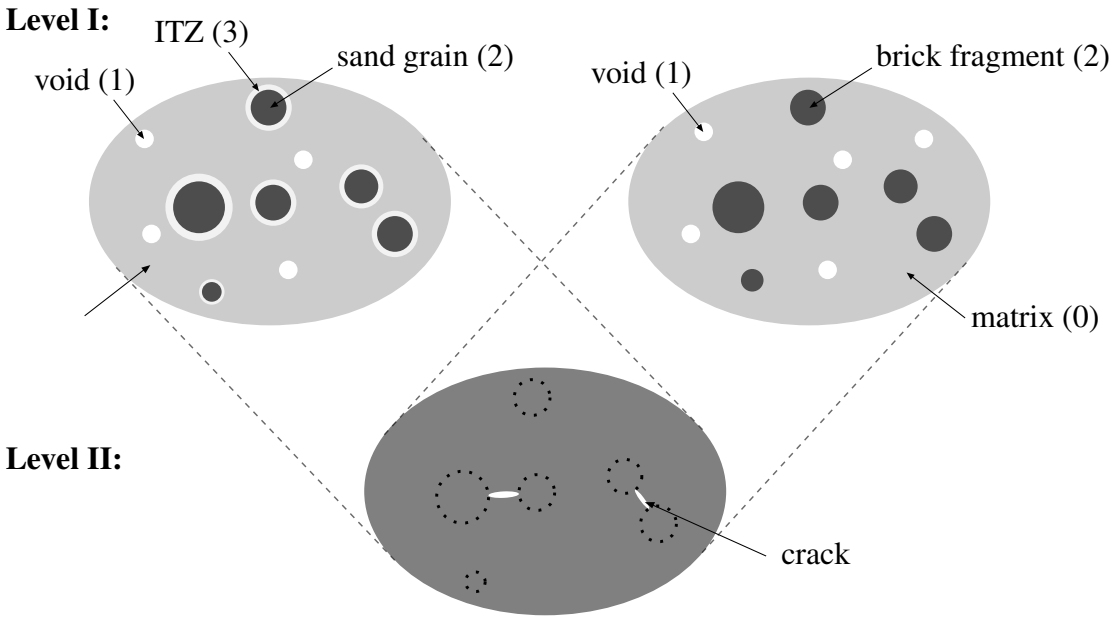

Figure 4.1: Scheme of the micromechanical model of mortars with various aggregate-types; the numbers in parentheses refer to the indexes of individual phases.

4.2.1 Elasticity

4.2.1.1 Level I: Homogenization of Aggregates and Voids

The elastic response of individual phases is described by the material stiffness matrix $\mathbf{L}^{(r)}$. Since all phases are considered as geometrically and materially isotropic, the matrix $\mathbf{L}^{(r)}$ can be decomposed using the orthogonal volumetric and deviatoric projections $\mathbf{I}_{\mathrm{V}}$ and $\mathbf{I}_{\mathrm{D}}$, e.g. [104, p. 23],

$$\mathbf{L}^{(r)} = 3K^{(r)}\mathbf{I}_{\mathrm{V}} + 2G^{(r)}\mathbf{I}_{\mathrm{D}}, \tag{4.1}$$

where $K^{(r)}$ and $G^{(r)}$ denote the bulk and shear moduli of the r-th phase.

Under the dilute approximation, the mean strain in individual phases, $\boldsymbol{\varepsilon}^{(r)}$, is related to the macroscopic strain, $\boldsymbol{\varepsilon}$, via the dilute concentration factors,

$$\boldsymbol{\varepsilon}^{(r)} = \mathbf{A}_{\mathrm{dil}}^{(r)}\boldsymbol{\varepsilon}. \tag{4.2}$$

In the Mori-Tanaka scheme, the strain in individual phases can be found as $\boldsymbol{\varepsilon}^{(r)} = \mathbf{A}_{\mathrm{dil}}^{(r)}\boldsymbol{\varepsilon}^{(0)}$, where $\boldsymbol{\varepsilon}^{(0)}$ is the strain within the matrix found as

$$\boldsymbol{\varepsilon}^{(0)} = \mathbf{A}_{\mathrm{MT}}\boldsymbol{\varepsilon}, \tag{4.3}$$

where the strain concentration factor $\mathbf{A}_{\mathrm{MT}}$ is provided by

$$\mathbf{A}_{\mathrm{MT}} = \left(c^{(0)}\mathbf{I} + \sum_{r=1}^{m} c^{(r)}\mathbf{A}_{\mathrm{dil}}^{(r)} \right)^{-1}. \tag{4.4}$$

Because of isotropy, the effective stiffness at Level I is fully specified by the effective bulk, $K^{\mathrm{I}}_{\mathrm{eff}}$, and shear, $G^{\mathrm{I}}_{\mathrm{eff}}$, moduli

$$K^{\mathrm{I}}_{\mathrm{eff}} = \frac{c^{(0)}K^{(0)} + \sum_{r=1}^{m} c^{(r)}K^{(r)}A^{(r)}_{\mathrm{dil,V}}}{c^{(0)} + \sum_{r=1}^{m} c^{(r)}A^{(r)}_{\mathrm{dil,V}}}, \qquad G^{\mathrm{I}}_{\mathrm{eff}} = \frac{c^{(0)}G^{(0)} + \sum_{r=1}^{m} c^{(r)}G^{(r)}A^{(r)}_{\mathrm{dil,D}}}{c^{(0)} + \sum_{r=1}^{m} c^{(r)}A^{(r)}_{\mathrm{dil,D}}} \tag{4.5}$$

that depend on the volumetric and deviatoric components of the dilute concentration factors

$$\mathbf{A}^{(r)}_{\mathrm{dil}} = A^{(r)}_{\mathrm{dil,V}}\mathbf{I}_{\mathrm{V}} + A^{(r)}_{\mathrm{dil,D}}\mathbf{I}_{\mathrm{D}}, r = 1, ..., m. \tag{4.6}$$

Uncoated Inclusions The dilute concentration factors for spherical particles follow from the seminal Eshelby work [54]:

$$A^{(r)}_{\mathrm{dil,V}} = \frac{K^{(0)}}{K^{(0)} + \alpha^{(0)}(K^{(r)} - K^{(0)})}, \qquad A^{(r)}_{\mathrm{dil,D}} = \frac{G^{(0)}}{G^{(0)} + \beta^{(0)}(G^{(r)} - G^{(0)})}, \tag{4.7}$$

where $\alpha^{(0)}$ and $\beta^{(0)}$ depend on the matrix Poisson's ratio, $\nu^{(0)}$, as:

$$\alpha^{(0)} = \frac{1 + \nu^{(0)}}{3(1 + \nu^{(0)})}, \qquad \beta^{(0)} = \frac{2(4 - 5\nu^{(0)})}{15(1 - \nu^{(0)})}. \tag{4.8}$$

Coated Inclusions The more involved case of particles coated by spherical shells was solved by Hervé and Zaoui [57]. Their introduction into the scheme makes the model sensitive to the grain-size distribution because the strain concentration factors depend on the radius of sand grains relative to their coating. From that reason the sand aggregates (2) and ITZ (3), Figure 4.1, must be subdivided into sub-phases m^{δ} corresponding to individual grain-size intervals. These are denoted by indices $(2, \delta)$ and $(3, \delta)$, where $\delta = 1, ..., m^{\delta}$.

Spatially, the dilute concentration factors for sand grains and surrounding ITZ, both represented by their outer radii, $R^{(2,\delta)}$ and $R^{(3,\delta)}$, and Poisson's ratios, $\nu^{(2)}$ and $\nu^{(3)}$, in the form

$$A^{(2,\delta)}_{\mathrm{dil,V}} = \frac{1}{Q^2_{11}}, \quad A^{(3,\delta)}_{\mathrm{dil,V}} = \frac{Q^1_{11}}{Q^2_{11}} \tag{4.9}$$

and

$$A^{(2,\delta)}_{\mathrm{dil,D}} = A_1 - \frac{21}{5}\frac{{R^{(2,\delta)}}^2}{1 - 2\nu^{(2)}}B_1, \quad A^{(3,\delta)}_{\mathrm{dil,D}} = A_2 - \frac{21}{5}\frac{{R^{(3,\delta)}}^5 - {R^{(2,\delta)}}^5}{(1 - 2\nu^{(3)})({R^{(3,\delta)}}^3 - {R^{(2,\delta)}}^3)}B_2, \tag{4.10}$$

where the auxiliary factors Q^1_{11}, Q^2_{11}, A_1, A_2, B_1 and B_2 are provided in [19, Appendix A].

The volume fractions of the coatings, $\{c^{(3,\delta)}\}_{\delta=1}^{m^{\delta}}$, are determined from the given volume fractions of the sand sub-phases, $\{c^{(3,\delta)}\}_{\delta=1}^{m^{\delta}}$, as

$$c^{(3,\delta)} = \left(\left(\frac{R^{(3,\delta)}}{R^{(2,\delta)}}\right)^3 - 1\right)c^{(2,\delta)}. \tag{4.11}$$

Because the coatings are assume to replace the matrix surrounding the inclusions, their total volume fraction $\sum_{\delta=1}^{m^{\delta}} c^{(3,\delta)}$ is subtracted from the matrix volume fraction $c^{(0)}$.

4.2.1.2 Level II: Homogenization of Shrinkage-Induced Cracks

The effective stiffness at Level II accounts for the effects of randomly distributed cracks under the dilute approximation. This reduction is accomplished by introducing additional compliances H_{E} and H_{G} [59]:

$$H_{\mathrm{E}} = \frac{f}{E^{\mathrm{I}}_{\mathrm{eff}}} \frac{16(1-{\nu^{\mathrm{I}}_{\mathrm{eff}}}^2)(10-3\nu^{\mathrm{I}}_{\mathrm{eff}})}{45(2-\nu^{\mathrm{I}}_{\mathrm{eff}})}, \qquad H_{\mathrm{G}} = \frac{f}{E^{\mathrm{I}}_{\mathrm{eff}}} \frac{32(1-{\nu^{\mathrm{I}}_{\mathrm{eff}}}^2)(5-\nu^{\mathrm{I}}_{\mathrm{eff}})}{45(2-\nu^{\mathrm{I}}_{\mathrm{eff}})}, \tag{4.12}$$

where f is the crack density parameter, determined later in Section 4.2.1.3, $E^{\mathrm{I}}_{\mathrm{eff}}$ and $\nu^{\mathrm{I}}_{\mathrm{eff}}$ are the effective Young's modulus and the Poisson ratio at Level I, obtained from (4.5) through, e.g. [104, p. 23],

$$E^{\mathrm{I}}_{\mathrm{eff}} = \frac{9K^{\mathrm{I}}_{\mathrm{eff}}G^{\mathrm{I}}_{\mathrm{eff}}}{3K^{\mathrm{I}}_{\mathrm{eff}}+G^{\mathrm{I}}_{\mathrm{eff}}}, \qquad \nu^{\mathrm{I}}_{\mathrm{eff}} = \frac{3K^{\mathrm{I}}_{\mathrm{eff}}-2G^{\mathrm{I}}_{\mathrm{eff}}}{2(3K^{\mathrm{I}}_{\mathrm{eff}}+G^{\mathrm{I}}_{\mathrm{eff}})}, \tag{4.13}$$

The effective Young's and shear moduli of the cracked composite then follow from

$$E^{\mathrm{II}} = \left(\frac{1}{E^{\mathrm{I}}_{\mathrm{eff}}} + H_{\mathrm{E}}\right)^{-1}, \qquad G^{\mathrm{II}}_{\mathrm{eff}} = \left(\frac{2(1+\nu^{\mathrm{I}}_{\mathrm{eff}})}{E^{\mathrm{I}}_{\mathrm{eff}}} + H_{\mathrm{G}}\right)^{-1}. \tag{4.14}$$

4.2.1.3 Crack Density Estimation

The criteria for the formation of shrinkage cracks were established based on results of 3D FE model containing 200k to 700k tetrahedral linear elements, depending on the RVE size. The average average element size was equal to 0.1 mm. The RVE consisted of two spherical inclusions embedded in a matrix. The model was supported in three corners in such a way to allow contraction of the RVE in all directions without external constraints. The shrinkage was introduced into the model via incrementally increased matrix eigenstrain and the resulting system was solved by the Newton-Raphson algorithm. Because the study was focused on establishing the critical gap between the inclusions, the simulations were stopped after the crack between the inclusions appeared or if the eigenstrain reached $4\,\%$, since such value corresponds to the maximum shrinkage of lime-based pastes [13].

The simulations were performed in OOFEM software [106], utilizing the anisotropic damage material model by Jirásek [107] for the matrix, and the isotropic elastic model for the aggregates. The anisotropic damage material model utilizes the concepts from the microplane theory — the damage variable characterizes the relative compliance of the material for each microplane direction and therefore the stiffness is not reduced parallel to the crack. The material parameters of individual phases used for the analysis are summarized in Table 5.2. ITZ around aggregates was not explicitly modeled; however, the zone of damage around aggregates developed spontaneously due to tensile stresses perpendicular to the grains at the interface, Figure 4.4). The mesh-independence was ensured by the crack band approach [102].

The results of the simulations appear in Figure 4.3, in which we plot the critical shrinkage strain as a function of the dimensionless gap between the particles,

$$g_{12} = \frac{2l_{12}}{d_1+d_2}, \tag{4.15}$$

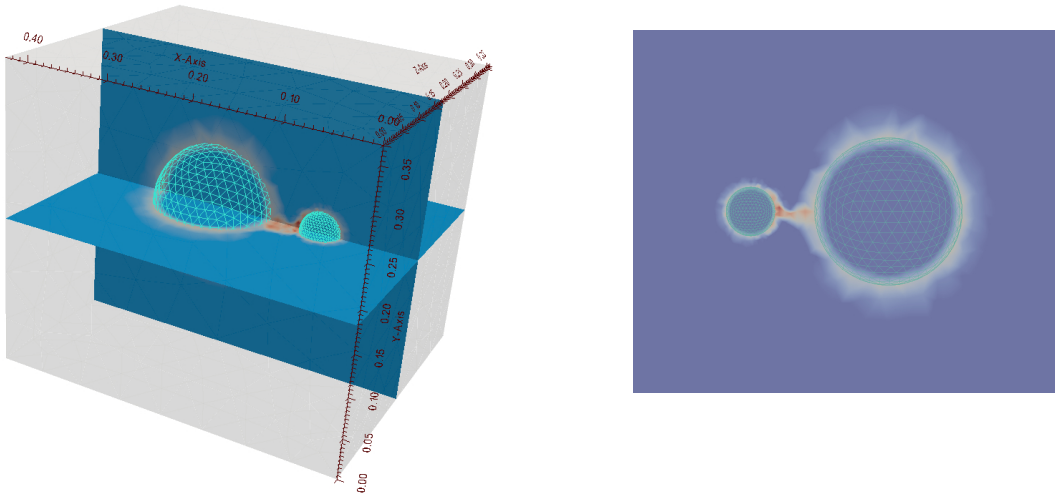

Figure 4.2: FE simulation of the crack formation between two aggregates of a size equal to 0.3 and 1.0 mm, respectively; visualized by ParaView software: axonometric view (left), front view (right). The red color indicates the formed cracks (the damage variable is equal to 1.0), while the blue regions represent the matrix volume with no damage.

where l_{12} stands for the face-to-face particle distance, and d_1 and d_2 are the particle diameters. Two particle types (compliant brick and stiff sand) and three ratios of the particle diameters were considered. For the shrinkage strain exceeding ≈ 0.1 % (which is much below the typical value of $\approx$ 4 % measured in [13]), we observe that a shrinkage crack between the particles develops if the gap is smaller than a critical value g_{crit}; otherwise no crack forms. The critical value is only weakly dependent on the diameter ratio, but depends strongly on the particle stiffness – in what follows we consider $g_{\text{crit}} = 0.37$ for the sand aggregates and $g_{\text{crit}} = 0.15$ for the brick aggregates, respectively.

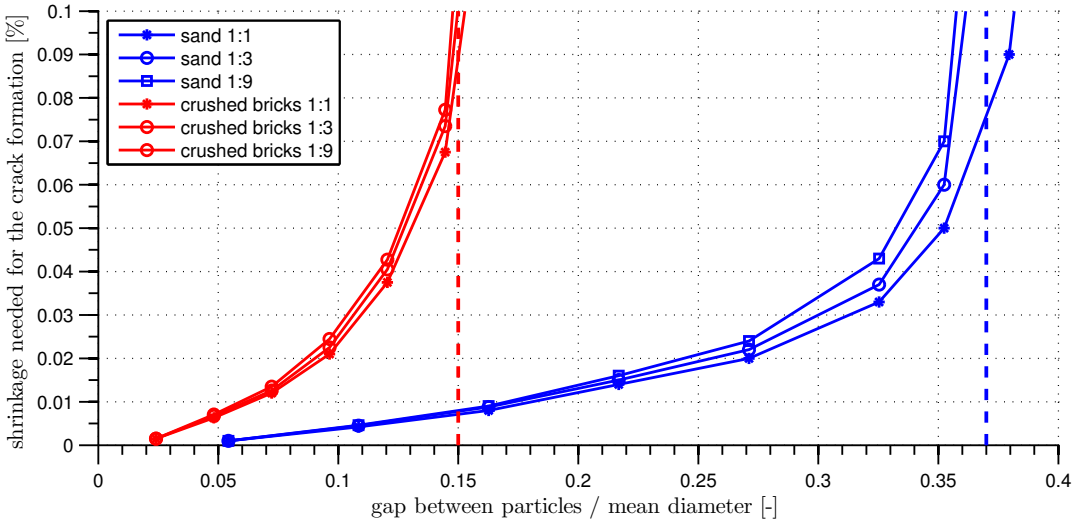

Figure 4.3: Critical relative gap, g_{crit}, indicated by dashed line for the compliant brick and stiff sand inclusions of three ratios of their diameters, when embedded in high-shrinkage (significantly exceeding 0.1 %) matrix.

Crack Density Parameter A circular penny-shaped crack is assumed to form between two neighboring particles once their dimensionless gap is smaller than g_{crit}. Given the number of the particles, k, distributed within a represenative volume element (RVE), Ω, the crack density parameter is defined as [59]

$$f = \frac{1}{|\Omega|} \sum_{\{i,j=1,\ldots,k: g_{ij} \leqq g_{\text{crit}}\}} (l_{ij})^3, \tag{4.16}$$

recall Eq. (4.15).

The input data to the crack density analysis were generated by an in-house packing algorithm for polydisperse spheres implemented in MATLAB. For the target volume fraction of the particles, $c^{(2)}$, and the given curve, we generate the particle distribution by a random sequential addition algorithm, proceeding from the largest particles to the smallest ones. As for the RVE size, we found that the size of 5-times maximum particle diameter yields the coefficient of variation in the density parameter f less than ≈ 2 %, Figure 4.4(b), which is sufficient for practical purposes.

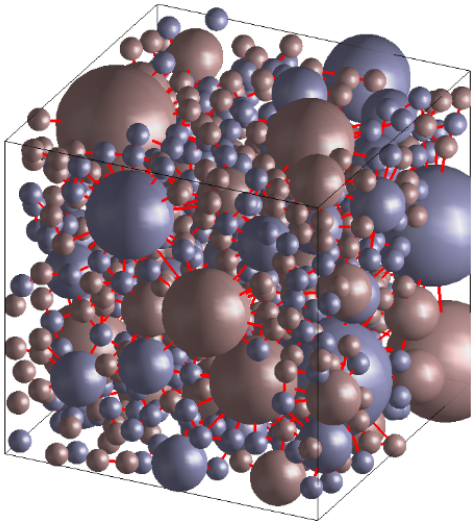

(a) example of polydisperse system RVE simulation ($c^{(2)} = 0.2$; the red lines indicate diameters of cracks between aggregates (if formed)

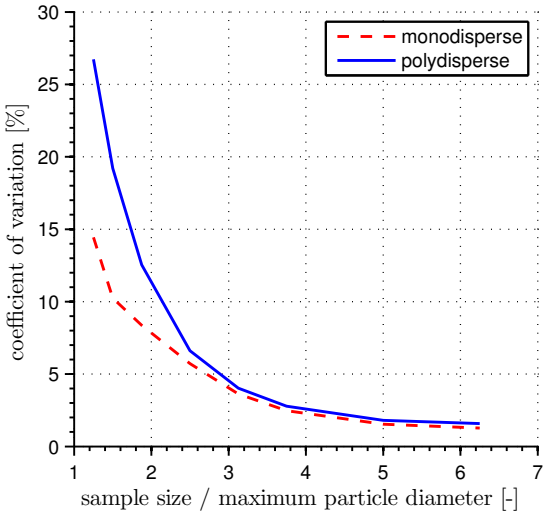

(b) relationship between RVE size relative to the maximum particle diameter and variation of the crack density parameters (based on 200 simulations)

Figure 4.4: MATLAB simulations of shrinkage-induced cracking within RVE

4.2.2 Compressive Strength

Inspired by phenomenological, e.g. [108], and micromechanical, e.g. [61], models for cementitious materials, we adopt the von-Mises failure criterion for the matrix phase,

$$\sqrt{J_2^{(0)}} - \frac{f_c^{(0)}}{\sqrt{3}} = 0, \tag{4.17}$$

to estimate the mortar strength in compression. In Eq. (4.17), $f_{\mathrm{c}}^{(0)}$ denotes the matrix compressive strength, and the second deviatoric invariant in the matrix phase, $J_2^{(0)}$, is determined from the average matrix stress, $\boldsymbol{\sigma}^{(0)}$, through

$$J_2^{(0)} = \frac{1}{2}\boldsymbol{\sigma}^{(0)^{\mathrm{T}}}\mathbf{I}_{\mathrm{D}}\boldsymbol{\sigma}^{(0)}. \tag{4.18}$$

The average stress in the matrix phase $\boldsymbol{\sigma}^{(0)}$ follows from the basic assumption of the Mori-Tanaka method, Eq. (4.3) as

$$\boldsymbol{\sigma}^{(0)} = \mathbf{L}^{(0)}\mathbf{A}_{\mathrm{MT}}\left(\mathbf{L}_{\mathrm{eff}}^{\mathrm{II}}\right)^{-1}\boldsymbol{\sigma}, \tag{4.19}$$

where $\boldsymbol{\sigma}$ stands for the applied macroscopic stress. The mortar compressive strength f_{c} is found by subjecting the sample to the macroscopic uniaxial stress state $\boldsymbol{\sigma} = [-f_{\mathrm{c}}, 0, 0, 0, 0, 0]^{\mathrm{T}}$, such that the condition (4.17) is satisfied.

4.2.3 Tensile strength and Fracture energy

Primarily the matrix phase is subjected to damage, but also the ITZ stiffness must be reduced to avoid locking effects. The materials' softening is driven by the damage evolution in the matrix phase at Level I

$$\boldsymbol{\sigma}^{(d)} = (1-\omega^{(0)})\mathbf{L}^{(d)}\boldsymbol{\varepsilon}^{(d)} = \mathbf{L}_{\mathrm{sec}}^{(d)}\boldsymbol{\varepsilon}^{(d)}, \tag{4.20}$$

where $d = 0, 3$ refers to the damageable phases. Because we assume that the strain in the matrix is increasing monotonically, the magnitude of damage in the matrix phase follows from

$$\omega^{(0)} = 1 - \frac{{\varepsilon_0}^{(0)}}{\varepsilon_{\mathrm{eq}}^{(0)}}\exp\left(-\frac{\varepsilon_{\mathrm{eq}}^{(0)} - {\varepsilon_0}^{(0)}}{\varepsilon_{\mathrm{f}}^{(0)} - {\varepsilon_0}^{(0)}}\right), \tag{4.21}$$

where $\varepsilon_{\mathrm{eq}}^{(0)}$ denotes the Rankine effective strain, determined from the tensile parts of the principal strains $\langle\varepsilon_I^{(0)}\rangle_+$ via

$$\varepsilon_{\mathrm{eq}}^{(0)} = \|\boldsymbol{\varepsilon}^{(0)}\| = \max_{I=1}^{3}\langle\varepsilon_I^{(0)}\rangle_+. \tag{4.22}$$

The critical equivalent strains at the damage onset, $\varepsilon_0^{(0)}$, and the fracturing strain, $\varepsilon_{\mathrm{f}}^{(0)}$, follow from

$$\varepsilon_0^{(0)} = \frac{f_{\mathrm{t}}^{(0)}}{E^{(0)}}, \qquad \varepsilon_{\mathrm{f}}^{(0)} = \frac{G_{\mathrm{f}}^{(0)}}{f_{\mathrm{t}}^{(0)}h}, \tag{4.23}$$

where $f_{\mathrm{t}}^{(0)}$ is the matrix tensile strength, $G_{\mathrm{f}}^{(0)}$ represents the matrix fracture energy, and h is the crack band width of the strain-softening zone [102], set to 2.7 times the maximum aggregate [109].

In order to estimate the effective tensile properties, we subject the composite to incremental strain path ($n = 1, 2, \ldots$)

$$\boldsymbol{\varepsilon}_n = [\varepsilon_{1,n-1} + \Delta\varepsilon, 0, 0, 0, 0, 0]^{\mathrm{T}}, \tag{4.24}$$

where $\Delta\varepsilon$ is a fixed strain increment, equal to 10^{-7}, and $\boldsymbol{\varepsilon}_0 = \mathbf{0}$. The damage in the matrix phase at the n-th load step, $\omega_n^{(0)}$, is determined from the consistency condition between the

damage value in (4.20), related to the reduction of the matrix and ITZ stiffness, and the value determined from (4.21) with the local strain $\boldsymbol{\varepsilon}^{(0)}$ estimated by the elastic Mori-Tanaka method from Eq. (4.3) with adjusted phase stiffnesses $\mathbf{L}_{\text{sec}}^{(d)}$ and the overall strain set to $\boldsymbol{\varepsilon}_n$. The resulting single non-linear equation for $\omega_n^{(0)}$ is solved by the conventional secant method on the interval $[\omega_{n-1}^{(0)}; 1]$ with the accuracy set to 10^{-8}. The simulation is stopped when the damage variable $\omega^{(0)}$ reaches the value of 0.999; that corresponds to the N-th time step.

The effective tensile parameters are obtained post-processing of the history of macroscopic stresses

$$\boldsymbol{\sigma}_n = \mathbf{L}_{\text{eff},n}^{\text{II}} \boldsymbol{\varepsilon}_n \text{ for } n = 1, 2, \ldots, N. \tag{4.25}$$

In particular, the effective tensile strength f_{t} is estimated as

$$f_{\text{t}} = \max_{n=1}^{N} \|\boldsymbol{\sigma}_n\|, \tag{4.26}$$

while the effective fracture energy G_{f} follows from

$$G_{\text{f}} = \frac{h\Delta\epsilon}{2} \sum_{n=1}^{N} \left(\sigma_{n-1,1} + \sigma_{n,1}\right). \tag{4.27}$$

4.3 Experimental Analysis

In this section, we gather the results of experimental studies needed to acquire the input data to the model, summarized in Table 5.2, as well as the validation data. After introducing the mortar components, Section 4.3.1, in Section 4.3.2 we discuss the acquisition of the elastic properties of individual phases. Section 4.3.3 is dedicated to inelastic properties of the matrix phase and the validation data are introduced in Section 4.3.4. Note that all experiments were always carried out on at least six specimens representing the same material or batch, in order to obtain representative data. In addition, when possible, we also compared our results with independent results from the literature, in order to ensure their credibility.

Table 4.1: Material properties of individual phases; ρ, E, ν, f_{c}, f_{t}, G_{f}, and PSD denote the mass density, Young's modulus, Poisson's ratio, compressive strength, tensile strength, fracture energy, and particle-size distribution, respectively.

phase	ρ [kg/m^3]	E [GPa]	ν [-]	f_{c} [MPa]	f_{t} [MPa]	G_{f} [J/m^2]	PSD
matrix	1,066	8.00	0.25	7.0	2.0	12.0	×
voids	×	0	0.25	×	×	×	no need
crushed bricks	1,761	3.50	0.2	×	×	×	needed
siliceous sand	2,720	90.0	0.17	×	×	×	needed
ITZ	1,066	2.67	0.25	×	×	×	thickness of 10 μm

4.3.1 Materials

The investigated mortars were reinforced by sand or crushed brick fragments, and the desired grain size distributions were obtained via sieving. The binder was composed of commonly available white air-slaked lime (CL90) Čertovy schody, Czech Republic, of a high purity (98.98 % of CaO + MgO), and metakaolin (finely ground burnt claystone, commercial name Mefisto L05) in a mass ratio equal to 7:3. The amount of water was adjusted so that the fresh mortars fulfilled the workability slump test, which is set according to ČSN EN 1015-3 as 15±1 cm.

The volume of individual phases listed in Table 5.2 was calculated from the mass of mortar constituents and the measured mass density, ρ. The matrix mass was determined based on the result of our previous study [13], which revealed that 1 kg of slaked lime powder and metakaolin mixed in the ratio 7:3 produce 1.46 kg of the paste. The volume of voids was obtained experimentally using the pycnometer method. For detailed information on the conversion of mass fractions to the volume volume fractions for individual phases, the reader is referred to [19, Section 3].

4.3.1.1 Particle-Size Distribution

The model validation was done on two kinds of samples, considering monodisperse and polydisperse particle-size distribution of the aggregates. The term "monodisperse" refers to a single to fraction 0.5–1.0 mm, obtained by sieve separation during preparation of the samples. The polydisperse particles were spanning the diameter range from 0.063 mm to 4.0 mm; for illustration see the grading curves plotted in Figure 5.1.

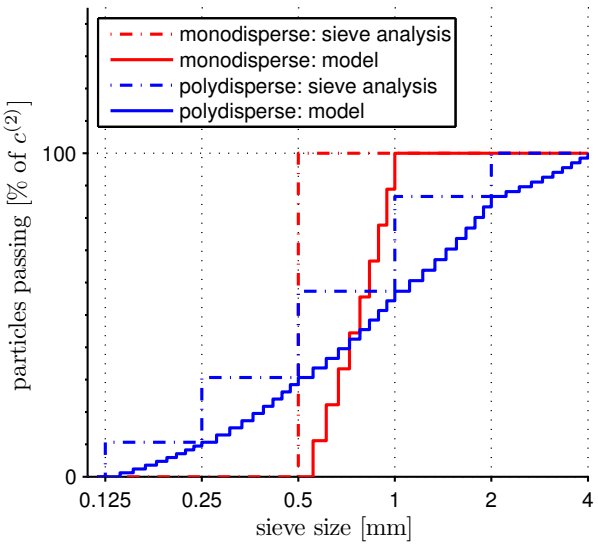

Figure 4.5: Grading curves representing the grain-size distributions of monodisperse and polydisperse aggregates. The sieve analysis provides the distribution into five rather wide intervals, which are further decomposed each into 9 sub-intervals by the linear interpolation for the calculation purposes.

4.3.2 Elastic Parameters

4.3.2.1 Matrix Young's Modulus

The matrix elastic stiffness (Young's modulus) was studied by means of quasi-static nanoindentation, the nanohardness tester (CSM Instruments, Switzerland) equipped with Berkovich pyramidal diamond tip. The mortar sample containing sand aggregates was sectioned and polished before the measurement, and a suitable location (away from aggregates) with minimum roughness was selected, Figure 4.6. Load-controlled quasi-static indentation test was employed for all imprints, with the load function containing three segments (constant loading at 24 mN/min, 10 seconds holding period, and unloading at 24 mN/min). The indents were evaluated according to the Oliver and Pharr methodology [99], utilizing the unloading part for the assessment of the material elastic modulus. The holding period was introduced to reduce the creep effects on the elastic unloading [98].

The penetration depth of individual indents varied in order to find the relationship between the penetration depth and the measured Young's modulus. A rapid decrease in elastic stiffness with increasing penetration depth, Figure 4.6 indicated that the evaluated Young's modulus was affected by the presence of microscale porosity occurring within the indented material volume. According to our measurements, based on mercury intrusion porosimetry, the maximum pore size was established as 900 nm and virtually no pores occurred beyond that limit. As a consequence, the penetration depth about 2,200 nm appeared sufficient to include all nano- and micro-pores, yielding the effective matrix stiffness approximately 8 GPa, see Figure 4.6.

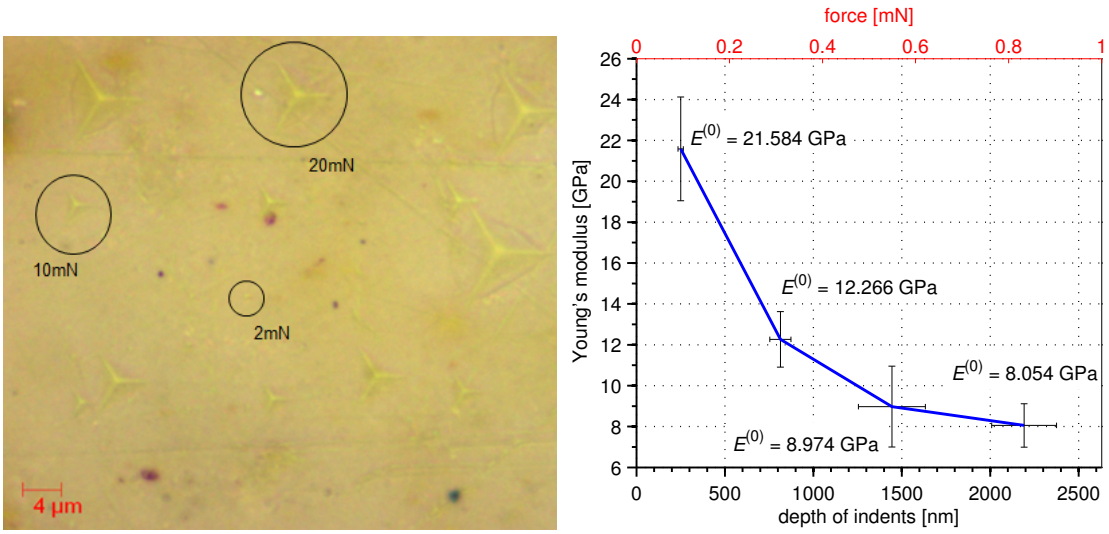

(a) location and size of indents within the lime-metakaolin matrix

(b) dependence of the effective matrix Young's modulus on the depth of indents; the vertical error bars indicate standard deviations in the measured Young's moduli, horizontal ones represent the deviations in indentation depth

Figure 4.6: Assessment of the matrix stiffness by means of nanoindentation.

Note that a similar study has been performed by Nežerka et al. [13] for pure lime-based pastes and their mechanical properties. However, the measured values of Young's modus

3.3 GPa reported therein cannot be used for the modeling of mortars, since the pastes were porous and contained larger voids due to the lack of aggregates. The inclusions contribute to consolidation of the fresh mortar, which results in a much denser matrix.

4.3.2.2 Young's Modulus of Aggregates and ITZ

The Young's modulus of crushed brick fragments was assessed using the resonance method as an average of six measurements on the uncrushed prismatic specimens (40 × 40 × 160 mm). The Young's modulus of river sand was provided by Nilsen and Monteiro [110] and the value is in agreement with Daphalapurkar et al. [111] who used nanoindentation for the sand elastic stiffness assessment.

According to Yang [112], the ITZ stiffness reduction in the thickness of 10 μm around stiff aggregates is approximately 30 %, compared to the surrounding matrix. The formation of damaged zone due to shrinkage cracking was also predicted by the numerical model as demonstrated in Figure 4.2. Therefore, the 30 % matrix stiffness reduction was also adopted in our micromechanical model. The reinforcement of the interface between the crushed brick fragments and the surrounding matrix by the formation of hydration products [31, 97] was not considered in the model, because their impact on mechanical properties was found to be negligible [13].

4.3.2.3 Poisson's Ratio

The values of the Poisson's ratio were set according to literature survey. Namely, the value of 0.25 was proposed for the lime-based pastes by Drdácký and Michoniová [113], and we employ the same value also for voids and ITZ. Vorel et al. [60] considered the value of the Poisson's ratio equal to 0.17 for siliceous sand and the same value was suggested in [19] for clay brick fragments.

4.3.3 Inelastic Matrix Properties

4.3.3.1 Matrix Compressive Strength

The onset of plastic deformation is assumed to take place exclusively in the matrix. Its strength was determined from the destructive uniaxial compression tests carried out on cubic 40 × 40 × 40 mm specimens of lime-metakaolin pastes, as described in [13].

4.3.3.2 Matrix Tensile Strength and Fracture Energy

Since the damage evolution in our model is restricted to the matrix, the tensile strength and fracture energy of other phases was not investigated. Because of a complicated clamping of the samples during the uniaxial tension test and huge scatter of the measured data [13], the tensile (formally flexural) strength was determined from the three-point bending tests on unnotched simply supported 160 × 40 × 40 mm beams with the distance between supports equal to 120 mm.

The same experimental set-up was employed for the determination of the fracture energy, however, the beams were weakened by a 10 mm notch in the midspan in order to capture the descending part of the load-displacement diagram and avoid snap-back. The fracture energy, G_f, was evaluated directly from the recorded load-displacement diagram using the RILEM approach [83].

4.3.4 Validation Data

Beside the acquisition of the input data, the purpose of the experimental analysis was to validate the proposed model. To that goal, six mortar specimens representing each batch were cast in prismatic molds 40 × 40 × 160 mm, compacted using shaking table to get rid of excessive air bubbles, and removed from the molds after 24 hours. The amount of water was adjusted so that the fresh mortars fulfilled workability defined by ČSN EN 1015-3 and the mortar cone expansion was in the range of 13±0.5 cm. Curing of mortars was executed at the temperature of 20±1 °C and relative humidity ranging between 65 and 75 %. The material properties of each mortar mix were assessed after the curing period of 3 months, using the same methods as described in Sections 4.3.2.1, 4.3.3.1, and 4.3.3.2.

The binder was composed of the same constituents as described in Section 4.3.1, i.e. lime and metakaolin in the mass ratio equal to 7:3. The aggregates were either sand or crushed bricks, both of monodisperse and polydisperse particle-size distribution as indicated in Figure 5.1. In order to test the model predictions, the samples with polydisperse distribution were prepared in variable binder to aggregate ratio, yielding the aggregate volume fractions equal to $c^{(2)}$= 0.238, 0.384, 0.483, 0.555, and 0.609, respectively.

4.4 Results and Discussion

To reproduce the experimental outcomes, the computational procedures described in Section 4.2 were employed. The Young's modulus, tensile strength and fracture energy were obtained by an inverse analysis of the stress-strain diagrams predicted by the proposed model[1]. The simulations of uniaxial compression and tension tests were carried out considering the same composition as pursued when preparing the tested mortars presented in Section 4.3.1. The study was mainly focused on the relationship between the effective mortar properties and the volume fraction of aggregates, either crushed bricks or quartz sand, both in mono- and poly-disperse configuration.

The accuracy of our model is demonstrated by means of the uniaxial tensile stress-strain curves in Figure 4.7, provided by the analysis of the samples with "monodisperse" particle size distribution, recall Figure 5.1. The visual comparison suggests that the model matches well the elastic modulus and the peak strength; the post-peak softening curves are reproduced less accurately, but still provide reasonably accurate values of the fracture energy.

The purpose of the following Sections 4.4.1–4.4.4 is to make these observations more quantitative, by investigating the accuracy of the Young's modulus, compressive and tensile

[1]The MATLAB code **Homogenizator MT: Composite with Cracks**, can be used for reproduction of results contained in this paper and it is freely available at `http://mech.fsv.cvut.cz/~nezerka/software`.

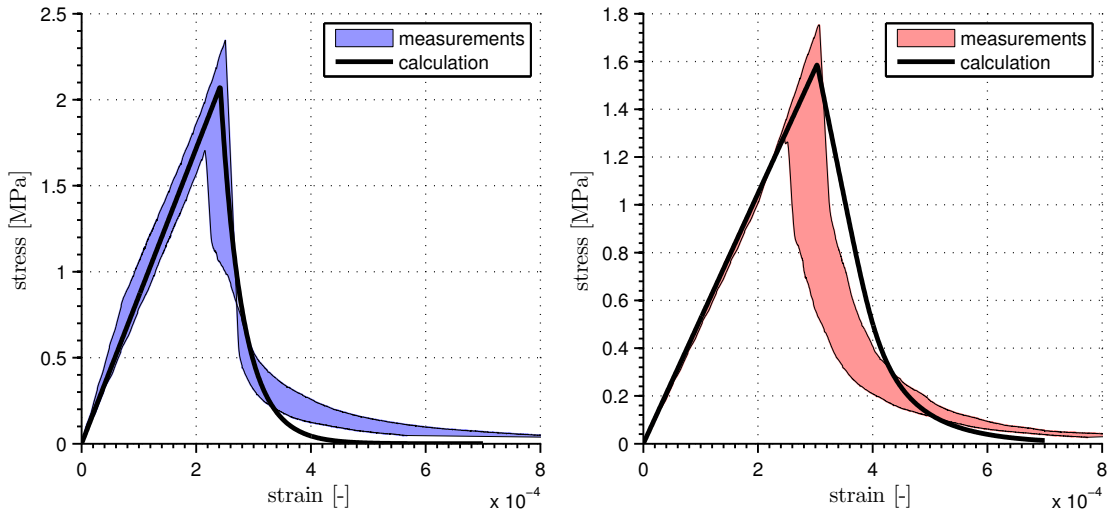

Figure 4.7: Comparison between the experimentally obtained and calculated stress-strain diagrams in uniaxial tension for the mixes containing monodisperse sand (left) and crushed brick (right) aggregates.

strengths, and tensile fracture energy, respectively. After validating the model, the study is closed by determining the optimal sand-to-crushed bricks composition in Section 4.4.5. We shall use the Pearson correlation coefficient

$$\xi = \frac{\sum_{i=1}^{n}(x_i - \overline{x})(y_i - \overline{x})}{\sqrt{\sum_{i=1}^{n}(x_i - \overline{x})^2}\sqrt{\sum_{i=1}^{n}(y_i - \overline{y})^2}} \tag{4.28}$$

to quantify the match between the n measured values $x_1, x_2, \ldots, x_n$ and the corresponding model predictions $y_1, y_2, \ldots, y_n$, with e.g. $\overline{x} = \frac{1}{n}\sum_{i=1}^{n} x_i$.

4.4.1 Young's Modulus

Figure 4.8(a) demonstrates that the Young's modulus of mortars containing sand is constant with the increasing volume fraction of sand particles. This rather surprising behavior is the result of the development of ITZ around the grains, as suggested by Neubauer et el. [96], and the presence of cracks among the shrinkage-constraining grains, observed e.g. in the study of mortar microstructures by Mosquera et al. [40].

The mortar stiffness reduction with the increasing volume fraction of crushed bricks is a consequence their compliance, which in turn results in the reduction shrinkage-induced cracking and elimination of ITZ formation. Moreover, the hydration promoting nature of the water-retaining crushed brick fragments and their rough surface contribute to a perfect interfacial bond, which has a positive impact on the inelastic properties discussed next.

Given that the values of Pearson correlation coefficient equal 0.973, Figure 4.8(b), the model predictions of the effective Young's modulus can be considered very accurate. Such accuracy can be attributed to the introduction of penny-shaped cracks between closely packed aggregates into the homogenization scheme at Level II. Without this step, the method significantly overestimate the stiffness of lime-based mortars, especially for stiff sand aggregates,

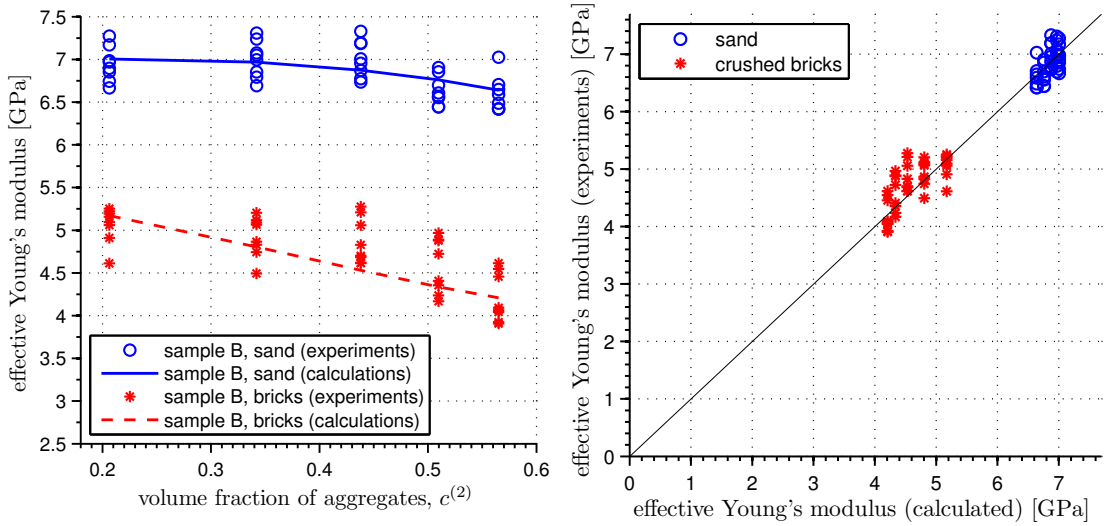

(a) dependence of the effective mortar Young's modulus on the amount of aggregates

(b) comparison between the calculated and measured values ($\xi = 0.973$)

Figure 4.8: Comparison between the calculated effective Young's modulus and the experimentally obtained data on mortars containing polydisperse aggregates.

see [21] for further details.

4.4.2 Compressive Strength

As follows from our experimental data, Figure 4.9(a), and from independent findings by Lanas et al. [29], the compressive strength of mortars containing sand grains should be higher than of those with crushed brick fragments and its value should decrease with increasing aggregate volume fractions, because of the stress concentration in the matrix phase. Both trends are correctly reproduced by our model both quantitatively and qualitatively; as visible from Figure 4.9(b), the agreement between the model predictions and experiments are of a similar accuracy as for the Young's modulus.

4.4.3 Tensile Strength

According to experimental measurements, Figure 4.10(a), the tensile strength of lime-based mortars is also reduced with the increasing volume fraction of aggregates, which is also in agreement with the findings of Lanas et al. [29]. The tensile strength reduction with the increasing amount of aggregates is more pronounced in the case of mortars containing sand. This phenomenon is reflected by higher strain concentrations in the matrix, responsible for the onset of damage at lower levels of externally applied macroscopic strain. The agreement between the model and experiments for the tensile strength is slightly worse that in the case of elastic stiffness, compare Figure 4.10(b) to Figure 4.8(b), but we consider such accuracy to be sufficient for engineering purposes, especially when taking into account the scatter of experimental data, Figure 4.10(a).

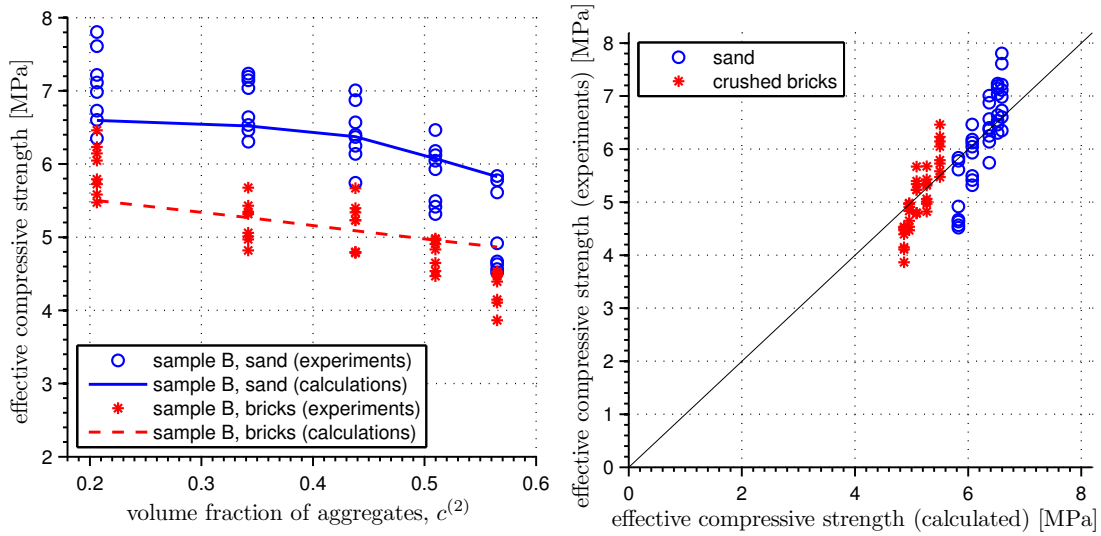

(a) dependence of the effective mortar compressive strength on the amount of aggregates

(b) comparison the between the calculated and measured values (ξ= 0.846)

Figure 4.9: Comparison between the calculated effective compressive strength and the experimentally obtained data on mortars containing polydisperse aggregates.

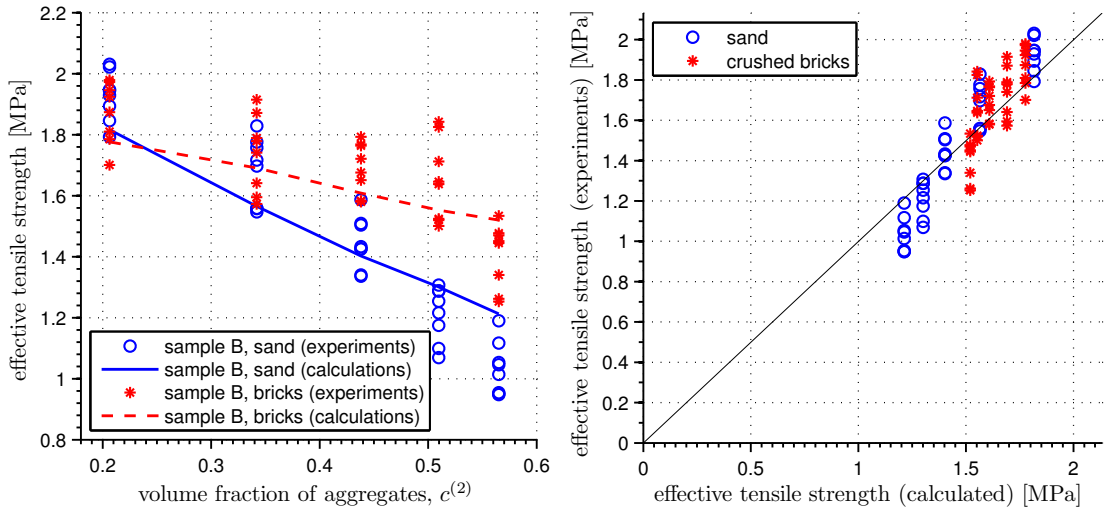

(a) dependence of the effective mortar tensile strength on the amount of aggregates

(b) comparison the between the calculated and measured values (ξ = 0.916)

Figure 4.10: Comparison between the calculated effective tensile strength and the experimentally obtained data on mortars containing polydisperse aggregates.

4.4.4 Fracture Energy

According to both, model and experiments, the values of fracture energy were higher in the case of mortars containing crushed brick aggregates, also because of the lower contrast in elastic properties leading to the decrease in stress concentrations. In consequence, these mortars accumulate more energy by allowing to reach higher values of elastic deformation, Figure 4.7. Again, the predictions of our model are satisfactory considering the relatively high scatter of the experimentally obtained data, as indicated by ξ equal to 0.879, see Figure 4.11(b).

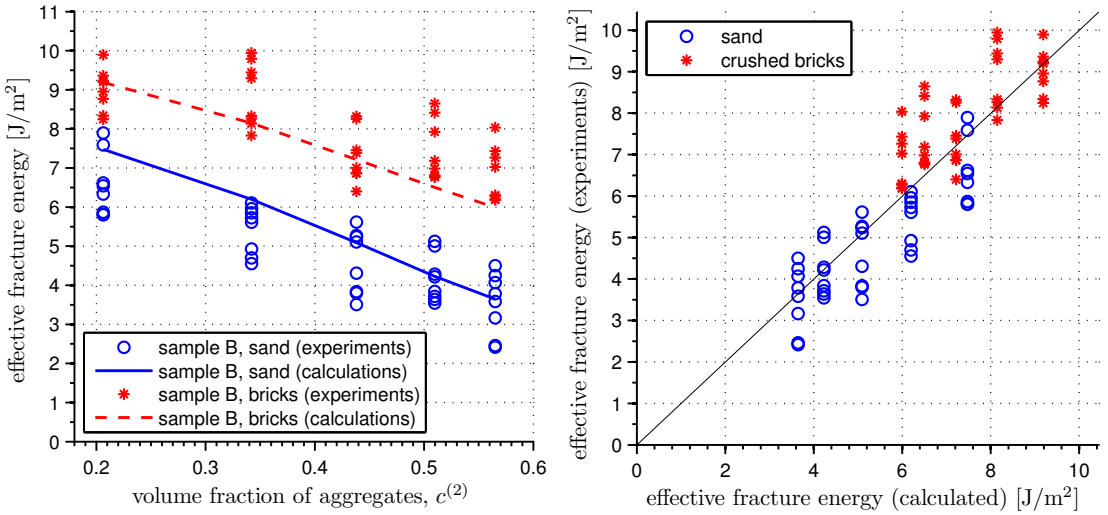

(a) dependence of effective mortar fracture energy on the amount of aggregates

(b) comparison the between the calculated and measured values (ξ = 0.879)

Figure 4.11: Comparison between the calculated effective fracture energy and the experimentally obtained data on mortars containing polydisperse aggregates.

In summary, our experimental and model-based results confirm that with respect to sand-reinforced lime mortars, the mortars containing crushed brick particles provide lower stiffness, higher tensile and compressive strengths, and fracture energies. These factors combined allow to achieve significantly larger maximum strain and ductility in tension, which probably contributes to the increased earthquake resistance. Such conclusions correspond well with the findings by e.g. Moropoulou et al. or Baronio et al. [18, 41], but our model provides a different explanation for the emergent behavior. Specifically, the improved mechanical performance is in [41] primarily attributed to the formation of hydration products at the interface between the lime matrix and fragments of crushed bricks. Even though this phenomenon has been recently confirmed by nano-indentation [20], our model reveals that it is of secondary importance. The dominant mechanism is found in the reduction of the shrinkage cracks due to more compliant cricks at Level II of the model; recall Figure 4.3 and see [21] for an explicit demonstration in the elastic regime.

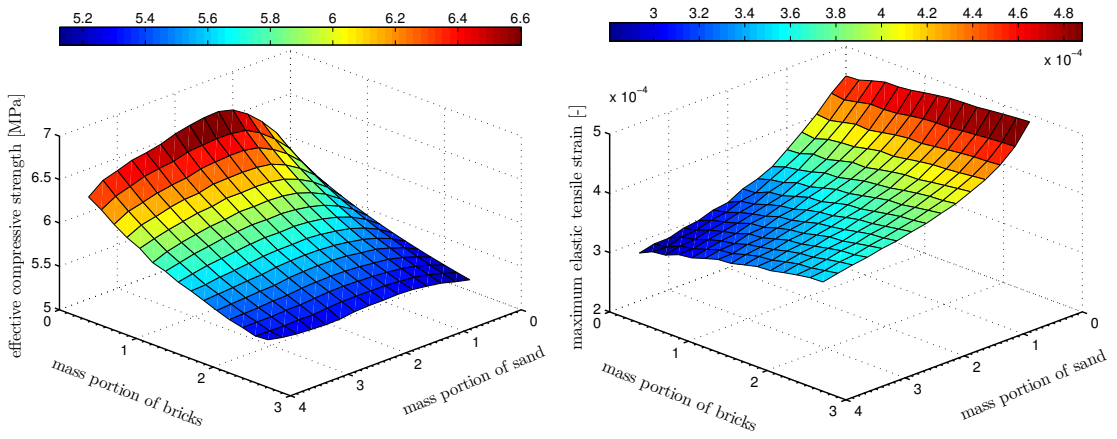

Figure 4.12: Dependence of the mortar compressive strength (left) and maximum elastic deformation in tension (right) on the amount of sand and crushed brick fragments, considering polydisperse aggregates.

4.4.5 Mortar Mix Optimization

Having validated the model, we now proceed with its application to the design of the optimal ratio between the amount of sand and crushed brick fragments to achieve maximum elastic deformation in tension and compressive strength. Figure 4.12 shows the predicted dependence of the target effective mortar properties, from which we suggest the optimum binder / sand / crushed bricks ratio equal to 1:1:1.5. These values are close to the generally established minimum binder / sand mass ratio 1:3 [12] in order to avoid excessive cracking, especially when recalculated to volumetric fractions due to low mass density of crushed brick aggregates. Based on our experience, such ratio also provides optimum workability when used as a bed joint masonry mortar.

4.5 Conclusion

The simple micromechanics-based model of lime-based mortars for the estimation of their elastic stiffness, compressive and tensile strength, and fracture energy was proposed and validated against experiments. The model consists of two levels, where the lower level describes the interaction among individual components of a mortar mix, while the upper scale accounts for the shrinkage-induced cracks that significantly influence the overall mechanical performance. As for the prediction of the effective parameters, the Mori-Tanaka / Dilute Approximation was used to estimate the overall stiffness, a J_2-based failure condition involving the average stress in matrix is adopted under compression, and under tension we employed the incremental Mori-Tanaka method coupled with the isotropic damage law and crack bend theory.

Based on the presented results, it was found that the model correctly predicts

1. the elastic stiffness of mortars containing sand, which does not increase with the increasing volume fraction of the aggregate due to the formation of ITZ and shrinkage-induced cracks between closely packed grains,

2. the elastic stiffness of mortars containing crushed brick fragments, which is also reduced by the addition of crushed bricks as a consequence of their low stiffness, and due to formation of shrinkage-induced cracks between the particles, however in lesser extent compared to the stiff sand grains,
3. the mortar compressive strength, which is higher in the case of mortars containing stiff sand grains, and decreases with the increasing amount of the aggregates,
4. the mortar tensile strength, significantly reduced by an increase of the amount of aggregates; the effect is more pronounced in the case of sand grains, rather than compliant crushed brick fragments,
5. the mortar fracture energy, being higher if the crushed brick fragments replace sand grains, since the more compliant mortars can reach higher elastic deformation.

For all these quantities, we reached both the quantitative and qualitative agreement between the experimental results and the model predictions.

The validated model can be used for obtaining the input data for numerical modeling of mortars at meso- and macroscale, or to find an optimal composition of the mix with respect to structural performance in masonry structures. As for the latter application, the interested reader is invited the following Chapter 5 (or paper [114]), where full-scale testing confirms that the optimized mortar delivers superior mechanical performance and durability with respect to conventional lime-based mortars with sand reinforcement.

Chapter 5

Performance of Lime-Based Mortars in Masonry Piers under Eccentric Loading

Based on: V. Nežerka, J. Antoš, J. Litoš, P. Tesárek, and J. Zeman, An Integrated Experimental-Numerical Study of the Performance of Lime-Based Mortars in Masonry Piers Under Eccentric Loading, *submitted to Construction and Building Materials* (2015) arXiv:1512.02407

5.1 Introduction

The study presented in this Chapter was focused on the investigation of various mortars commonly used for repairs of cultural heritage and their structural performance through comprehensive experimental and numerical analyses. In particular, lime-based mortars with various additives and aggregates, introduced in Section 5.2, were used in bed joints of masonry piers subjected to a combination of quasi-static compression and bending. The purpose of the experimental analysis, described in Section 5.3, was to study the failure modes and crack patterns using Digital Image Correlation (DIC), assess the structural performance of individual mortars, and verify the proposed material model used for the Finite Element (FE) predictions, presented in Section 5.4. The FE analysis was consequently utilized in Section 5.4.4 to assess the key material parameters influencing the load-bearing capacity, and to study the failure modes of the masonry piers containing mortars with variable properties, subjected to a combination of compression and bending.

5.2 Materials

The inconveniences connected to the use of modern lime, such as limited binder strength, slow hardening, enormous shrinkage, and consequent cracking and poor cohesion between the mortar and surrounding masonry blocks [12] can be overcome by the use of reactive additives rich in aluminosilicates, such as metakaolin or Portland cement. While metakaolin has been

generally accepted by the restoration community [5, 28], the use of Portland cement is on decline and the authorities for cultural heritage in many countries prohibit its additions to repair mortars [2, 3, 7]. According to a few studies, calcium-silicate-hydrates (CSH) and calcium-aluminum-silicate-hydrates (CASH) are the main hydrated phases formed at the room temperature after the pozzolanic reaction of metakaolin and $Ca(OH)_2$ [30, 32, 33]. The metakaolin presence in lime-based mortars results in an enhanced strength and durability [13], while the vapor transport properties are superior to the mortars containing Portland cement [7].

Beside the addition of pozzolans, shrinkage can be efficiently reduced by increasing the content of inert aggregates, since the stiff inclusions restrain the volume changes of the surrounding matrix [12, 44], which is more pronounced in the case of bigger inclusions [27]. However, large stiff pebbles are responsible for a formation of microcracks [24] that have a negative impact on the mortar integrity and reduce the mortar strength and stiffness [1, 29, 45]. Moreover, the shrinkage-induced cracking of mortars poor in pozzolans, or containing unsuitable aggregates, limits their use as renderings because of their poor aesthetic performance [40].

Even though it is generally accepted that the presence of sand aggregates increases the resistance of mortars against mechanical loading, there is a threshold beyond which any addition of aggregates makes the mortar weaker due to excessive microcracking and loss of cohesion between the grains and the surrounding matrix [1]. By experience, the 1 : 3 binder to aggregate volume ratio has been established as the most suitable for repair mortars, providing a reasonable strength, shrinkage and porosity. Based on the study by Stefanidou and Papayianni [27] it seems most favorable to use the sand of grain-size ranging between 0 and 4 mm, resulting in mortars of the highest strength.

The positive impact of compliant crushed brick aggregates is discussed in Chapter 4 with the indication of mass ration in a mortar mix. Beside the positive impact of crushed brick fragments on the mechanical properties and durability of the cocciopesto mortars, the use of crushed bricks brings another benefit — the use of waste by-products from ceramic plants leads to a cost reduction and production of a more sustainable material.

5.2.1 Prepared and Tested Mortars

For the presented study, we used a commonly available white air-slaked lime (CL90) Čertovy schody of a great purity (98.98% of CaO + MgO), produced in the Czech Republic. The most frequent particle diameter found in the lime hydrate was equal to 15 μm and its specific surface area, determined by the gas adsorption, was equal to 16.5 m^2/g. The finely ground burnt claystone metakaolin with a commercial name Mefisto L05, produced by České lupkové závody Inc., Nové Strašecí, Czech Republic, was chosen as the pozzolanic material. This additive is rich in SiO_2 (52.1 %) and Al_2O_3 (43.4 %). Portland cement CEM I 42.5 R produced in Radotín, the Czech Republic was used as an alternative to metakaolin. The selected Portland cement was rich in CaO (66 %), SiO_2 (20 %), Al_2O_3 (4 %), Fe_2O_3 (3 %), SO_3 (3 %) and MgO (2 %), as provided by XRF analysis [13].

Beside the investigation of metakaolin and Portland cement additions on the mechanical properties of lime-based mortars, the study was also focused on the influence of aggregate composition. River sand of grain size ranging between 0 and 4 mm from Zálezlice was selected based on experience as the most suitable for the application as the bed joint mortar. The

industrially produced crushed brick fragments of the grain-size 2–5 mm, from a brick plant Bratronice, the Czech Republic, were chosen based on results of previous studies [23] and experience of authors acquired by analyses of ancient mortar samples [18, 35, 72]. The grain size distribution of the sand and crushed bricks aggregates, obtained by a sieve analysis, is presented in Figure 5.1.

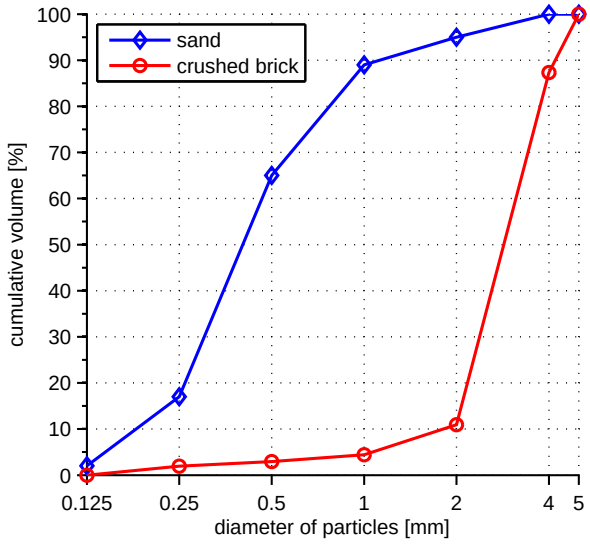

Figure 5.1: Grading curves of sand and crushed brick aggregates.

The mass ratio of lime and metakaolin / Portland cement was equal to 7:3 in all mortars. The amount of water was adjusted so that the fresh mortars fulfilled the workability slump test in accordance with ČSN EN 1015-3 and the mortar cone expansion reached 13.5±0.3 cm. Such consistency ensured a sufficient workability while keeping the water to binder ratio (w/b) as low as possible to avoid shrinkage cracking. The amount of aggregates was designed based on our experience, previous studies [1, 27, 29] and results of micromechanical modeling [24] towards high strength and acceptable shrinkage. The composition of the tested mortars is summarized in Table 5.1.

Table 5.1: Mass ratios of constituents in the tested mortars and their shrinkage after 90 days of hardening; PC and CB abbreviations stand for Portland cement and crushed bricks, respectively.

mix	binder			aggregate		water / dry mass	90-days
	lime	PC	metakaolin	sand	CB	(water / binder)	shrinkage
LC-S	0.7	0.3	–	3	–	0.175 (0.704)	0.71 %
LMK-S	0.7	–	0.3	3	–	0.180 (0.714)	0.83 %
LMK-SCB	0.7	–	0.3	1	1.5	0.250 (0.875)	0.64 %
L-SCB	1.0	–	0.3	1	1.5	0.320 (0.940)	1.10 %

The crushed bricks aggregate retains more water than sand (see the water / dry mass ratio records in Table 5.1). Based on such finding, we conjecture that the presence of water-retaining crushed bricks can promote the hydraulic reactions within the binder, and increase mortar strength and stiffness.

5.3 Experimental Testing

The experimental testing consisted of two stages — first the individual components, i.e. the mortars and masonry units, were subjected to series of three-point bending and compression tests in order to acquire the data necessary for the calibration of the FE model. The second stage involved a full-scale compression test of masonry piers.

5.3.1 Acquisition of Basic Material Parameters

The basic material parameters, describing the mechanical behavior of mortars and bricks, were obtained from results of three-point bending and uniaxial compression tests, carried out according to EN 1015-11. To that purpose six control specimens were cast into 160 × 40 × 40 mm prismatic molds, compacted using shaking table to get rid of excessive air bubbles, and removed after 48 hours. Curing was executed at the temperature of 20±1 °C and relative humidity ranging between 60 and 80 %.

Common fired clay bricks with dimensions 290 × 140 × 65 mm, produced in the brick plant Štěrboholy, the Czech Republic, were used as the masonry units for the construction of the tested masonry piers. In order to obtain the basic mechanical parameters, six 140 × 40 × 40 mm prisms were cut off the bricks and subjected to the three-point bending and compression tests. The same procedure was adopted for the mortar specimens.

Beside the bending and uniaxial compression tests, the dynamic Young's modulus was assessed by the resonance method on 90-day old samples, and the tensile strength of the interface between mortars and bricks was evaluated based on series of pull-out tests carried out in accordance with EN 1015-21. The tests revealed that the interface was not the weakest link in the case of all tested mortars, since the failure plane was not located at the brick boundary, Figure 5.2. The satisfactory interface strength is attributed to the relatively big roughness of the bricks and suitable workability of the fresh mortars.

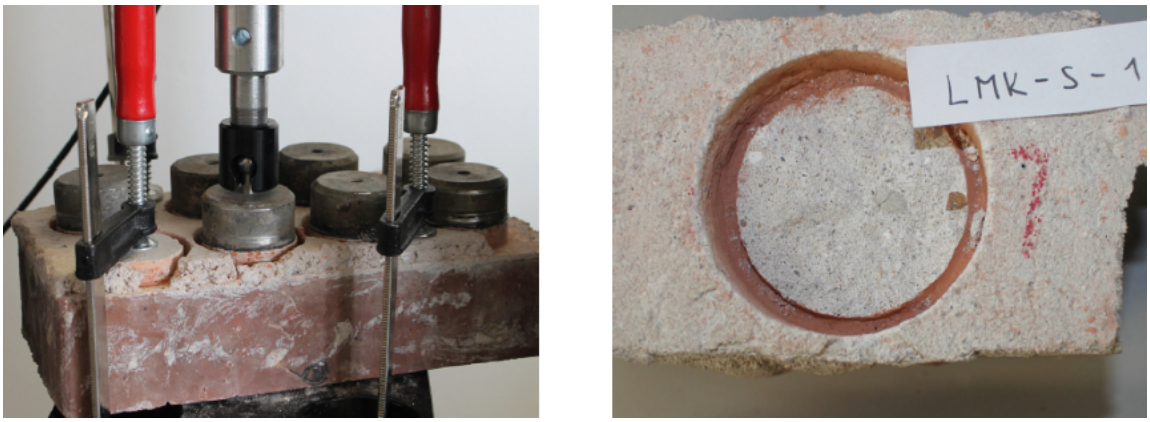

Figure 5.2: Interface strength pull-out testing: experiment set-up (left) and the failure plane located within the mortar layer (right).

5.3.1.1 Resonance Method

The non-destructive resonance method was utilized to assess the the dynamic Young's modulus, E_{dyn}, of both, mortars and brick. Such approach was chosen to overcome the inconvenience connected to the measurement of the static Young's modulus arising from the load-dependent compliance of the loading frame or improper attachment of strain-gauges. According to Malaikah et al. [79] the ratio between static and dynamic moduli measured on the same material should be within the range between 0.9 and 1.1.

The dynamic Young's modulus measurement is based on the equation for a longitudinal vibration of the beam with a continuously distributed mass and free-free boundary condition, following

$$E_{\mathrm{dyn}} = \frac{4Lmf_{\mathrm{I}}^2}{bt}, \tag{5.1}$$

where L is the length of the specimen [m], m is the mass of the specimen [kg], f_{I} is the fundamental longitudinal resonant frequency of the specimen [Hz], b is the width [m] and t is the thickness of the specimen [m]. For detailed information on the procedure of the dynamic Young's modulus assessment the reader is referred e.g. to [115].

The obtained values of the dynamic Young's modulus were used for re-scaling the displacements provided by the gauge attached to the loading frame, when evaluating the load-displacement diagrams provided by the three-point bending and uniaxial compression tests.

5.3.1.2 Three-Point Bending

The displacement-controlled three-point bending tests were performed on unnotched 160 $\times$ 40 $\times$ 40 mm simply supported beams with distance between supports equal to 100 mm in order to obtain the tensile failure-related material parameters. The loading was introduced in the midspan at the rate of 0.025 mm/min in order to capture the descending part of the load-displacement diagram and monitored using MTS Alliance RT 30 kN load cell.

5.3.1.3 Uniaxial Compression

The uniaxial compression test was carried out on cubic 40 $\times$ 40 $\times$ 40 mm specimens, cut off the halves of the cracked beams from the three-point bending test, using the same device as for the three-point bending. A uniform contact and force distribution was accomplished by loading the flat lateral sides, being in contact with mold during preparation of the specimens. The loading was displacement-controlled at the rate of 0.3 mm/min.

5.3.2 Testing of Masonry Piers

The geometry of the tested masonry piers of a square cross-section is described in the scheme provided in Figure 5.3. The piers were subjected to a displacement controlled quasi-static compression with an eccentricity to introduce a combination of bending and compression. The geometry, loading, boundary conditions, and material of the masonry blocks (clay bricks) were the same for all tested piers, because the study was focused on the influence of the bed joint

mortar. The bed joint thickness was equal to 15 mm, while the vertical joints were 10 mm thick, and the bricks were arranged in five layers to make a proper bond.

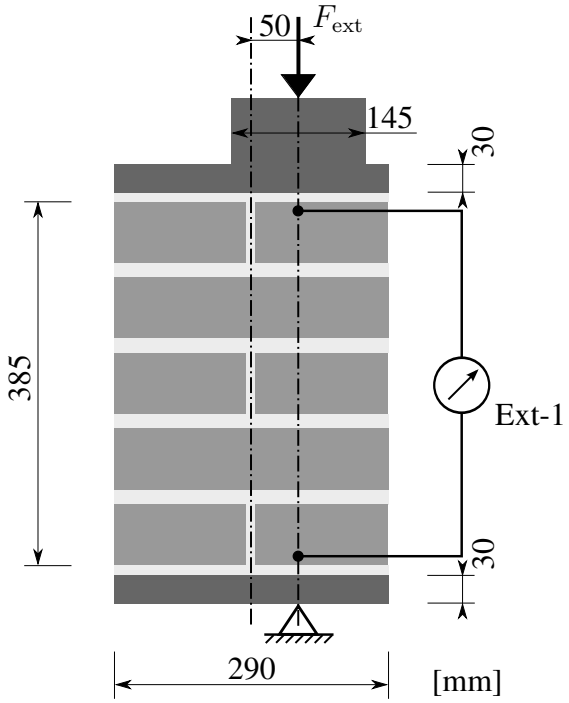

Figure 5.3: Loading of the tested piers and placement of virtual extensometers.

The loading of the piers was accomplished using a steel loading frame with a hydraulic actuator of 1 MN loading capacity. The steel slabs ensured a uniform distribution of stresses from the loading and a joint assembly allowed a rotation of the pier ends in all directions. The test was displacement-controlled with a loading rate of 1 mm/min in order to capture the descending part of the force-displacement diagram after the loss of pier integrity.

5.3.3 DIC

Extensometers and strain-gauges, conventionally used to measure displacements and deformation at pre-determined locations, cannot provide information about strain localization phenomena, such as cracking. The full-field DIC measurement allows to track the strain-field over the region of interest and capture the damage initiation and its progression until the complete loss of structural integrity. This non-contact method was first mentioned in papers by Yamaguchi [116], followed by Peters and Ranson [117], and their pioneering work established the basic principles.

DIC is based on tracking the in-plane deformation and displacement of a surface texture or a stochastic pattern applied artificially on a sample, Figure 5.5). A subset of gray-scale pixels in the reference image (representing an initial state) is matched to a subset with the best correlation within the deformed surface and its displacement and deformation are consequently evaluated. Using DIC, the deformation is not averaged over the strain-gauge length, because the averaging of strains depends purely on the camera resolution. Moreover, the technique is not

limited to the measurement of small strains and the surface can be relatively rough as in the case of masonry, where strain gauges usually fail. The studies focused on the evaluation of errors in the field of displacements and deformations obtained by DIC, e.g. [118, 119], demonstrate a relatively good accuracy of the method compared to conventional measurement techniques. A portion of the data can be lost if a spalling of the surface layer occurs, which easily happens in the case of quasi-brittle materials subjected to extreme loading, limiting the analysis of the post-peak behavior.

The optical monitoring of masonry piers was accomplished using high-definition Canon 70D camera taking pictures at 5-seconds time intervals, set equally for all tested piers, to yield on average 210 images documenting the deformation of a single pier until its complete failure. The light sensitivity ISO parameter was manually set to 100, since a powerful artificial lighting was available, Figure 5.4. The perfect illumination allowed the short exposure time (1/125 sec) and the low aperture number set to $f/8$, which was kept constant for all images in the series. In order to minimize the effect of lens distortion [120], the distance between the camera and the observed surface was approximately 1 m, and the focal length (zoom) was set to 55 mm. The resulting DIC real scale resolution equal to 0.202 mm/pixel was computationally feasible while preserving the required precision.

The displacement and strain fields were evaluated using an open source DIC software Ncorr [121], and post-processing of the results was accomplished using Ncorr_post tool [122], both operating in MATLAB environment. The DIC results were used for the validation of the numerical model introduced next in Section 5.4 and for capturing the strain localization. Figure 5.6 clearly demonstrates the difference between strain localization in bed joints in the case of a compliant (L-SCB) and a stiff mortar (LMK-SCB).

5.4 Numerical Simulations

The traditional design of masonry structures, based on rules-of-thumb, has been replaced by the numerical approach to address their complex failure mechanisms [123]. Our FE simulations were employed to find the optimum properties of the bed-joint mortars to be used in masonry piers subjected to a combination of compression and bending, which represents a typical loading of masonry walls, columns, and vaults. Mortar shrinkage was neglected in the numerical simulations. The verification process was accomplished by comparing the numerical predictions with the experimentally obtained data; DIC allowed to compare the predicted and observed failure modes, and easily construct the force-displacement diagrams.

In order to provide reliable predictions, the FE model must be supplied with a proper constitutive model. Based on experimental observations of masonry failure modes, damage-plastic models seem to provide the best description of both components, bricks and mortar. In the studies by Wawrzynek and Cincio [124] and Zhou et al. [125] the isotropic damage-plastic models were able to accurately describe the response of masonry to mechanical loading even in non-linear domain after plasticity and cracking took place.

In our simulations we used 15k (uniaxial compression test specimen), 30k (three-point bending test specimen), and 80k (masonry pier) linear tetrahedral elements and employed a phenomenological damage-plastic constitutive model proposed by Jirásek and Grassl [126],

Figure 5.4: Tested masonry pier subjected to the combination of compression and bending, introduced via eccentric loading and supporting.

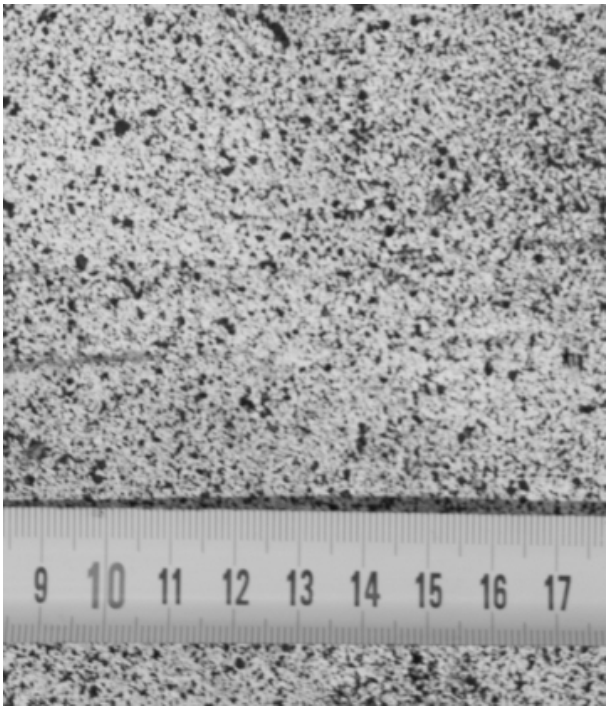

Figure 5.5: Black and white stochastic pattern applied onto the pier surface for the purposes of DIC; the main scale units represent centimeters.

implemented in the open-source FE package OOFEM [106]. The model was developed for the predictions of concrete failure subjected to general triaxial stress, and verified through a comprehensive experimental analysis.

The mesh generation was accomplished using Salome open-source generic platform and the post-processing of results and plotting the force-displacement diagrams was done using MATLAB scripts, while the graphical output was prepared in Paraview software.

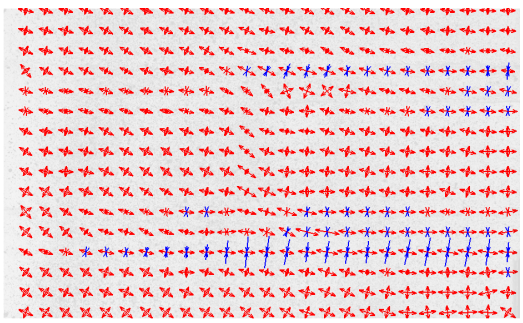

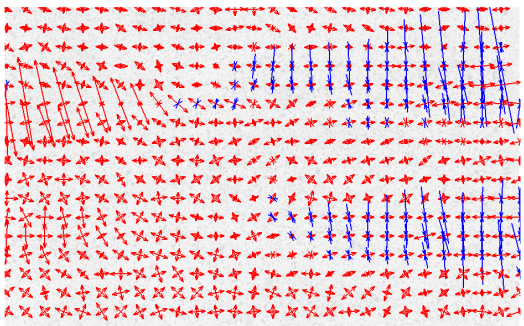

Figure 5.6: Direction and relative magnitude of principal strains on the surface of masonry piers: stiff LMK-SCB mortar joints (left) and compliant L-SCB joints (right); red and blue arrows indicate principal tension and compression, respectively.

5.4.1 Material Model

The material model [126] chosen to represent all components of the investigated masonry piers, i.e. studied mortars and bricks, considers the stress-strain law in the form of

$$\boldsymbol{\sigma} = (1 - \omega)\mathbf{D}_{\mathrm{e}} : (\boldsymbol{\varepsilon} - \boldsymbol{\varepsilon}_{\mathrm{p}}), \tag{5.2}$$

where $\boldsymbol{\sigma}$ is the stress tensor, ω is a scalar damage parameter (damage is assumed to be isotropic) and $\mathbf{D}_{\mathrm{e}}$ is the elastic stiffness tensor. In contrast to pure damage models the damage evolution is not driven by the total strain, $\boldsymbol{\varepsilon}$, but it is linked to the evolution of elastic strain, $\boldsymbol{\varepsilon} - \boldsymbol{\varepsilon}_{\mathrm{p}}$. The plastic part of the model formulation consists of a three-invariant yield condition, non-associated flow rule and a pressure-dependent hardening law. The mesh-independent response in the post-peak regime was achieved by the crack band approach [102, 127].

5.4.2 Identification of Material Model Parameters

The independent material model parameters to represent individual mortars and clay bricks were adjusted through an inverse analysis by reproducing the experimentally obtained data. First, the Young's modulus, E, and parameters to influence the flexural strength (tensile strength, f_{t}, and fracture energy, G_{f}) were adjusted to reproduce the results of the three-point bending tests, Figure 5.7.

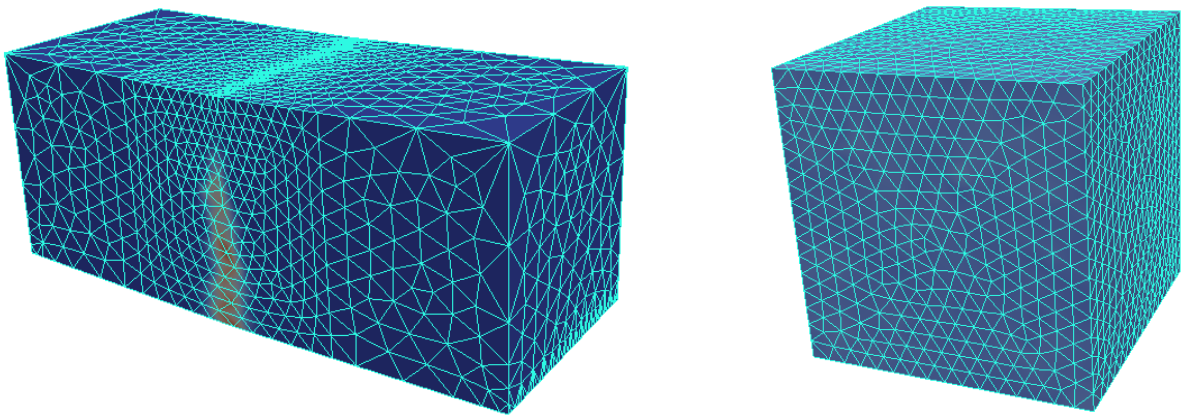

Figure 5.7: FE model of specimens for three-point bending (left) and uniaxial compression (right) tests.

The material model parameters to characterize the response to compression (compressive strength, f_{c}, softening and hardening parameters, A_{soft} and A_{hard} — see [126] for details) were calibrated by fitting the results from uniaxial compression tests. The Poisson's ratio was selected based on a literature study [19, 60, 113] as 0.2 to represent both, mortars and bricks. The influence of Poisson's ratio, ν, representing individual components was also analyzed to confirm its negligible impact on results when considered within reasonable bounds between 0.1 and 0.3, as reported in literature, e.g. [128, 129].

Even though the nature of the chosen material model did not allow to accurately reproduce the entire experimentally obtained load-displacement path, the results are, with respect

to the large scatter of the experimental data (indicated by the shaded area in Figures 5.8, 5.9, and 5.10), considered satisfactory. The summary of the material model input parameters to represent individual mortars and bricks are summarized in Table 5.2.

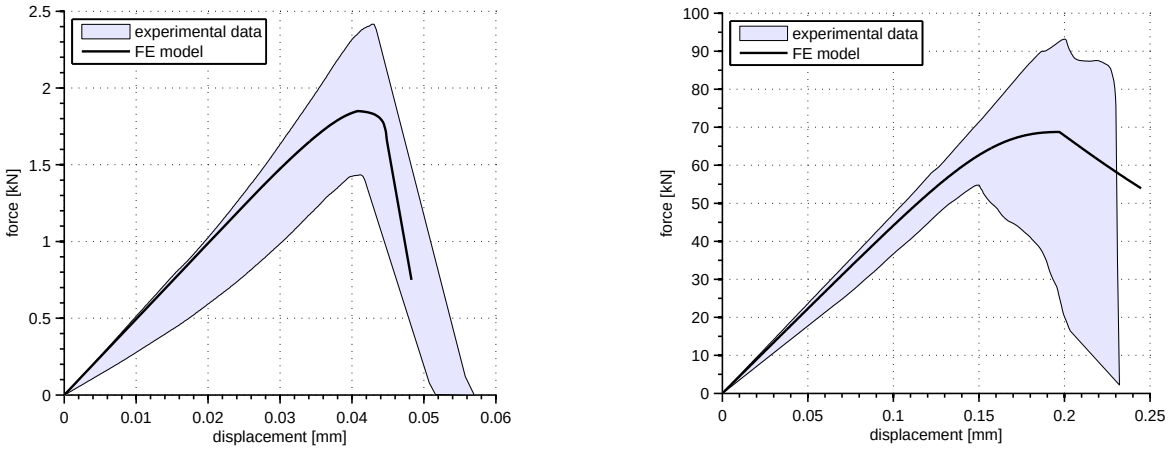

Figure 5.8: Fit of the material model input parameters representing bricks to reproduce the results of three-point bending (left) and uniaxial compression (right) tests.

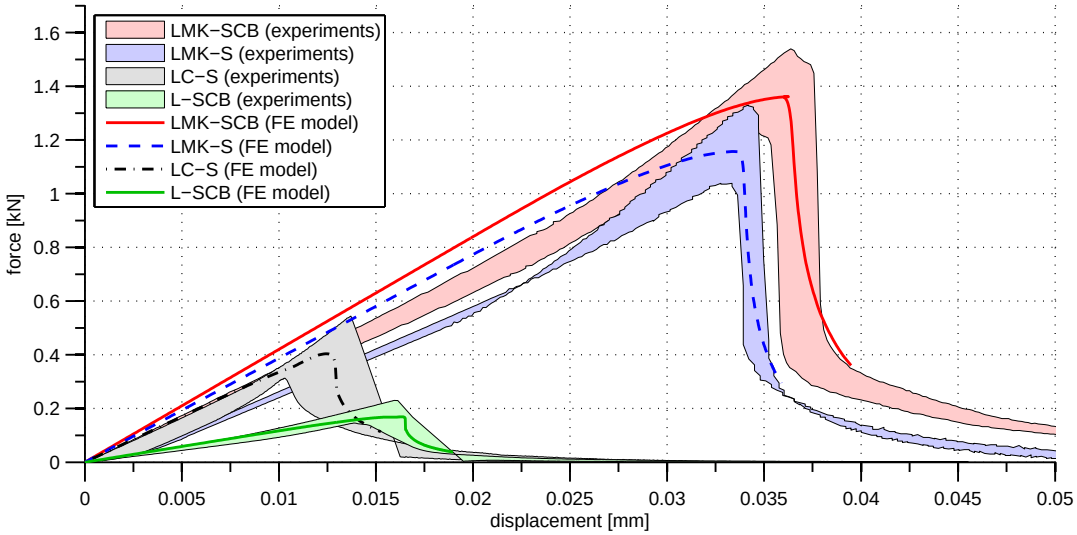

Figure 5.9: Fit of the material model input parameters representing the individual tested mortars to reproduce the results of three-point bending tests.

5.4.3 Numerical Simulations of Masonry Pier Failure

The geometry of the 3D FE model was following the geometry of the experimentally tested masonry piers, as described in Figure 5.3; the FE mesh is presented in Figure 5.11. The interface between bricks and surrounding mortar was not explicitly defined and modeled using interface elements, because the interface was not the weakest link in tension, recall Section 5.3.1.

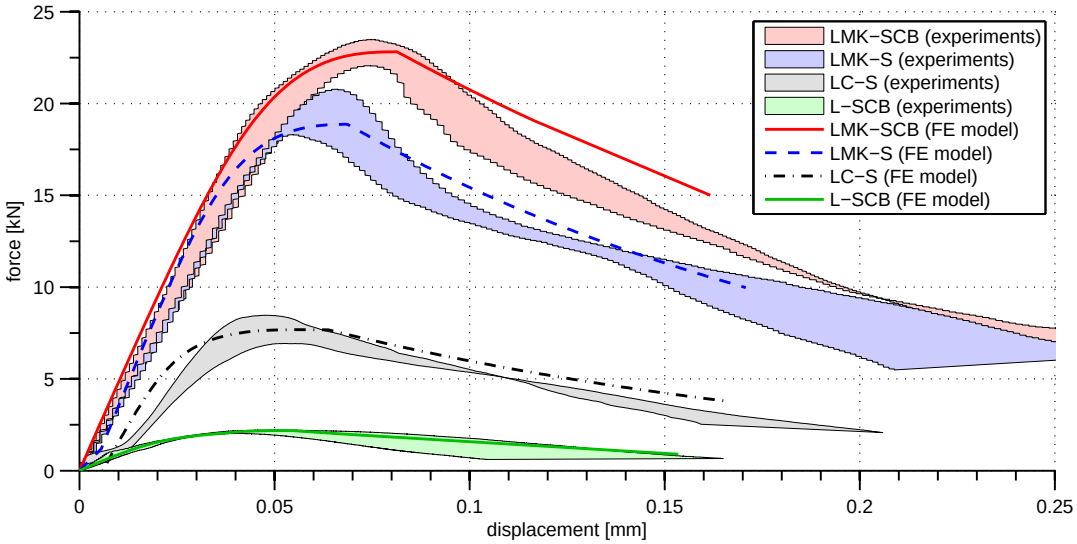

Figure 5.10: Fit of the material model input parameters representing the individual tested mortars to reproduce the results of uniaxial compression tests.

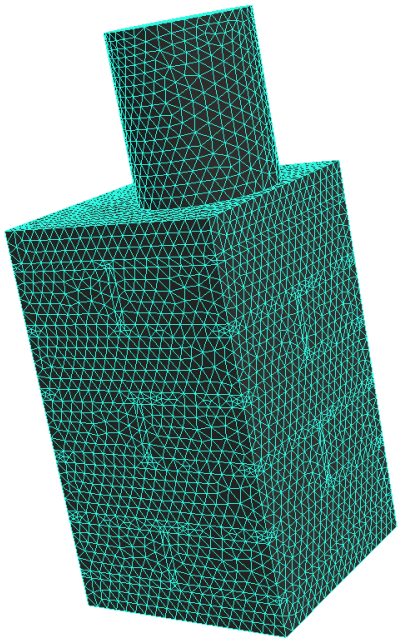

Figure 5.11: FE mesh of the investigated masonry piers.

Table 5.2: Key material input properties of bricks and the tested mortars; E, ν, f_c, f_t and G_f denote the Young's modulus, Poisson's ratio, compressive strength, tensile strength and fracture energy, respectively.

material	E [GPa]	ν [-]	f_c [MPa]	f_t [MPa]	G_f [J/m^2]
bricks	14.0	0.20	30.0	2.70	30.0
LC-S	7.10	0.20	4.80	0.55	3.20
LMK-S	7.40	0.20	11.3	1.53	13.5
LMK-SCB	10.0	0.20	14.7	1.92	26.0
L-SCB	2.45	0.20	1.30	0.26	1.55

In order to define the loading of the piers and boundary conditions in a realistic way, the model also consisted, beside the auxiliary steel slabs, of the cylindrical load cell, both modeled as an isotropic elastic continuum. The loading was accomplished by an incremental displacement imposed to a single node at the crest of the steel cylinder in order to allow rotations around all axes. The load-step increments were adjusted for each loading stage individually in order to reach convergence for a minimum computational cost.

The FE model was at first validated by comparing the predicted and measured load-displacement diagrams, as presented in Figure 5.12. Both, the reactions in a load cell and the displacements obtained from DIC by placing virtual extensometers at the top and bottom of the tested piers, were in a good agreement with the numerically obtained predictions, Figure 5.3. The agreement between the predicted cracking patterns (reflected in the field of damage distribution) and the observed development of cracks (visualized as a map of maximum principal strains obtained from DIC) is not perfect for all tested piers. However, considering the non-homogeneous microstructure of the tested materials, the FE analysis results cab be considered satisfactory.

In the case of piers with lime-cement mortar LC-S (Figure 5.13(a)), the model correctly predicted the formation of multiple cracks at the compressed side of the tested piers and the formation of two major cracks at the opposite side due to tensile stresses from the pier bending. The DIC results in the case of lime-metakaolin mortar LMK-S (Figure 5.13(b)) were influenced by a spalling of pier surface at the bottom, but the major crack formation in the middle of the tested pier can be identified in both, model predictions and DIC results. On the other hand, the formation of the major splitting crack in the case of mortar LMK-SCB (Figure 5.13(c)), containing metakaolin and crushed bricks, was perfectly predicted by the FE simulation, as well as the distributed cracking at the compressed pier edge in the case of the weak mortar L-SCB (Figure 5.13(d)).

In conclusion, the strategy to model the masonry units and mortar separately allowed us to capture the failure mode quite realistically (see Figure 5.13), enabling to study the relationship between the mechanical resistance of the masonry piers and bed-joint mortar properties.

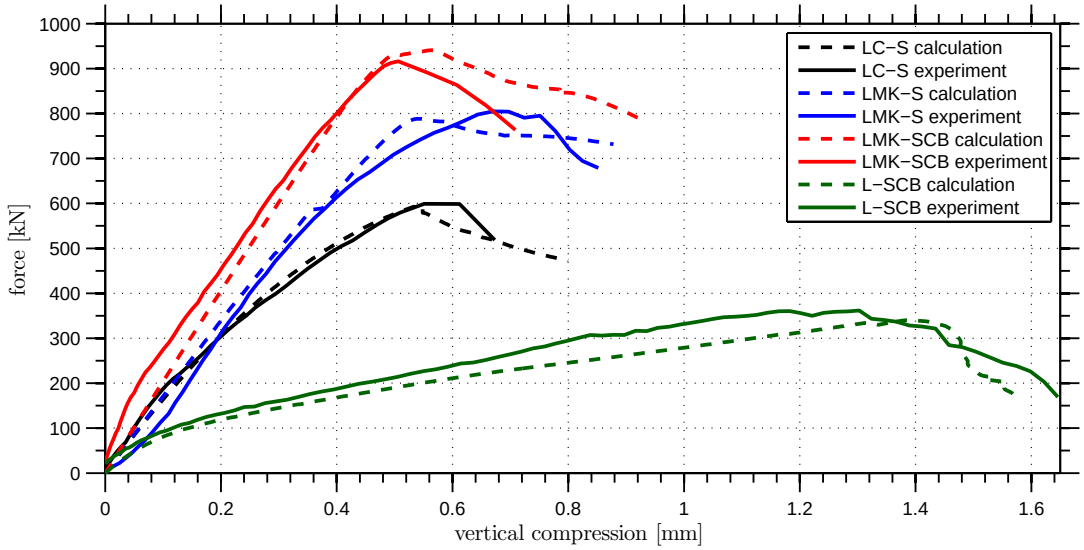

Figure 5.12: Comparison between the numerically and experimentally obtained load-displacement diagrams, describing the response of the tested masonry piers to the imposed vertical displacement at the crest of the loading cell.

5.4.4 Influence of Mortar Properties on Mechanical Resistance of Masonry Piers

The aim of the presented study was to show the relationship between the individual mortar material parameters and the load-bearing capacity of masonry piers having the same configuration of geometry and loading conditions as described in Sections 5.3 and 5.4.3. The lime-metakaolin mortar without crushed bricks (LMK-S) was chosen as the reference material, for which a single material parameter was changed at a time to assess its impact on the load-bearing capacity of the masonry pier.

Such analysis clearly indicated what the key material parameters were, and how to optimize the mortar composition towards a higher mechanical resistance of masonry structures. Similar approach was adopted e.g. by Sandoval and Roca [129], who studied the influence of geometry and material properties of individual constituents on the buckling behavior of masonry walls.

5.4.4.1 Influence of Mortar Stiffness

The plot in Figure 5.14 clearly demonstrates that the value of the mortar Young's modulus has just a minor impact on the load-bearing capacity of the studied masonry pier, and that there is no abrupt change when the mortar stiffness becomes superior to the stiffness of masonry units. However, the failure mode changes quite significantly. The use of a compliant mortar results in a multiple cracking of bricks at the more loaded side due to poor supporting, while a major crack passing through the entire column in the middle forms if the bed joints are stiff, see Figure 5.15.

It could seem advantageous to use mortars lacking pozzolanic additives because of their lower stiffness, in order to produce masonry of a higher deformation capacity within the elastic

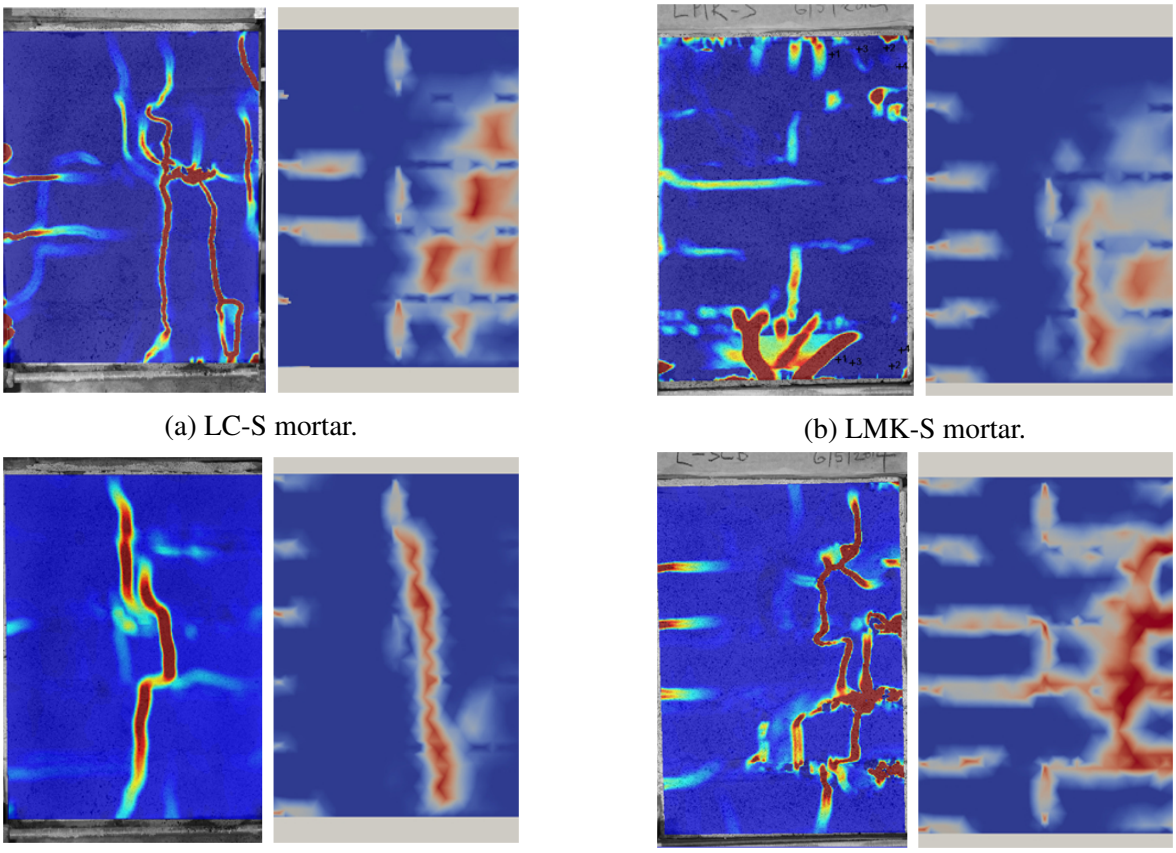

(a) LC-S mortar.

(b) LMK-S mortar.

(c) LMK-SCB mortar.

(d) L-SCB mortar.

Figure 5.13: Field of maximum principal strain obtained by DIC (left within the couples) and FE model damage predictions (right) on the face of the tested piers after reaching the peak load. The images provide a qualitative comparison between the predicted cracking patterns and experimental observations using DIC; the red areas represent the localized cracks.

range. Such masonry would in theory better resist seismic loading or imposed displacements, e.g. due to differential subsoil settlement. However, the compliant pure-lime mortars without additives promoting the hydraulic reactions are weak and suffer from an increased shrinkage cracking [13].

5.4.4.2 Influence of Mortar Tensile Strength

The tensile strength and fracture energy had to be modified carefully at the same time in order to avoid snap-back in the stress-strain diagram, and to preserve the same post-peak ductility for all investigated mortars.

Given the studied masonry pier and the boundary conditions, the tensile strength appears to have just a minor effect if it is lower than the strength of masonry units (bricks), see Figure 5.16. On the other hand, the mortars of higher strength in tension act as a confinement of the eunits and the masonry reinforcement. Since common lime- or cement-based mortars hardly attain the tensile strength superior to the strength of masonry units, the bed joint strengthening is

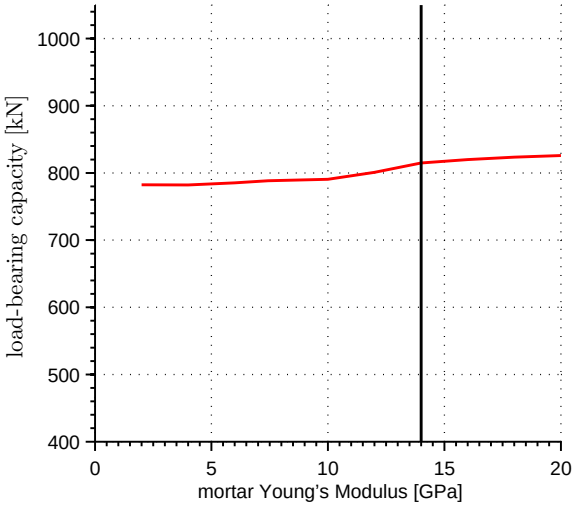

Figure 5.14: Dependence of the masonry pier maximum load-bearing capacity on mortar stiffness; black line represents the brick Young's modulus $E^{(\mathrm{b})}$ = 14 GPa.

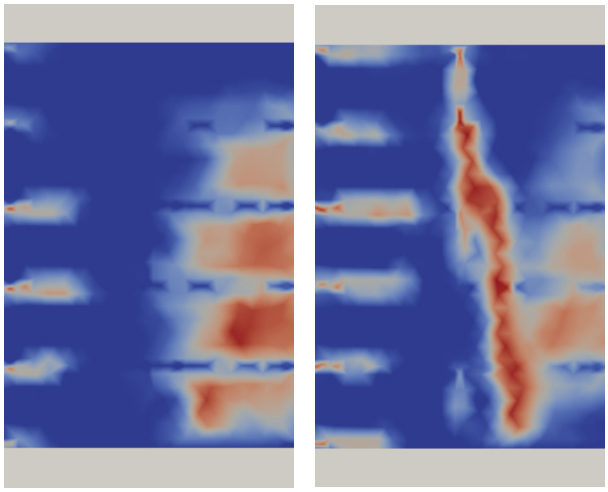

Figure 5.15: Crack patterns on masonry piers containing compliant ($E^{(\mathrm{m})}$ = 2 GPa, left) and stiff ($E^{(\mathrm{m})}$ = 20 GPa, right) mortar.

accomplished e.g. by means of embedded steel rods [130].

According to our numerical simulations, the confinement imposed by the strong mortars resulted in the cracking of the bricks and eventually the formation of the wedge-like failure as opposed to the vertical splitting of the pier containing a very weak mortar as indicated in Figure 5.17.

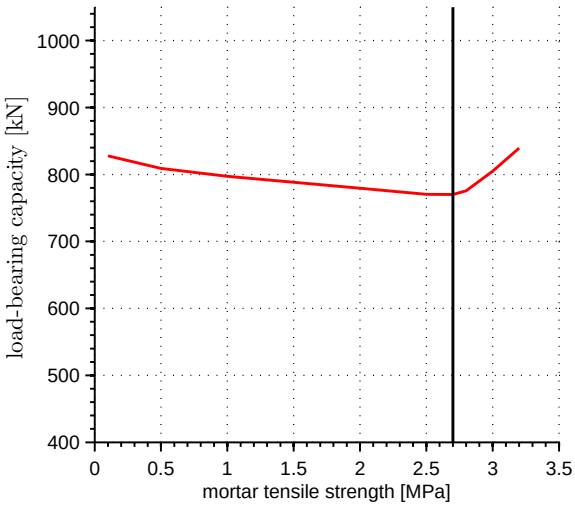

Figure 5.16: Dependence of the masonry pier maximum load-bearing capacity on mortar tensile strength; black line represents the brick tensile strength $f_{\mathrm{t}}^{(\mathrm{b})}$ = 2.7 MPa.

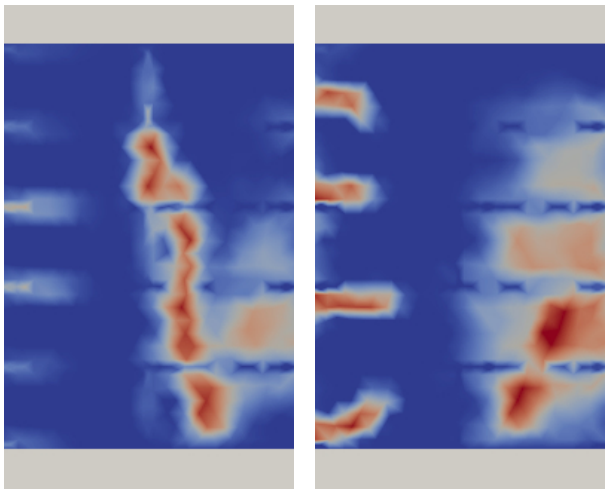

Figure 5.17: Crack patterns on masonry piers containing weak (f_{t} = 0.1 MPa, left) and strong (f_{t} = 3.2 MPa, right) mortar in tension.

5.4.4.3 Influence of Mortar Compressive Strength

The bed-joint mortar compressive strength appears to be the crucial parameter with respect to the load-bearing capacity of masonry subjected to a combination of compression and bending. Mortars of a low compressive strength suffer an irreversible deformation at relatively low levels of external load, and masonry units are consequently subjected to uneven distribution of stresses due to imperfect supporting and excessive deformation of the bed joints.

In the case of the modeled masonry piers, the early crushing of the weak bed-joint mortar resulted in cracking of bricks at the more loaded pier periphery, Figure 5.19. This phenomenon limited the load-bearing capacity of the tested pier rather significantly, especially in the case of very poor mortars ($f_c^{(m)} < 10$ MPa), see Figure 5.18. The bed joints containing mortars of a high compressive strength did not suffer the inelastic deformation before the major splitting vertical crack appeared due to transversal expansion, resulting in a high load-bearing capacity. Therefore, the mortars with superior compressive strength should be used especially if a bed joint reinforcement is introduced so that the high strength can be efficiently exploited.

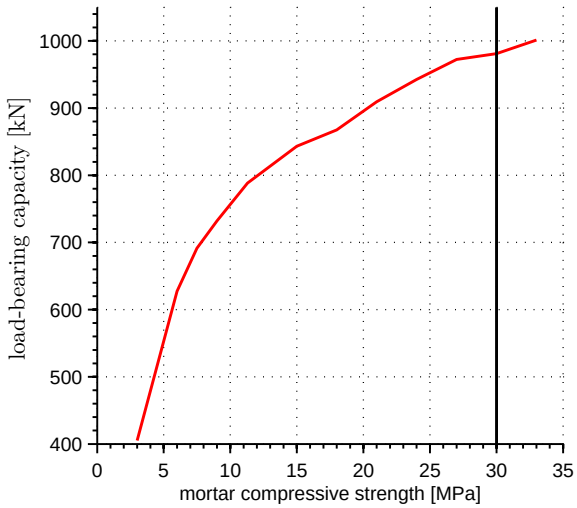

Figure 5.18: Dependence of the masonry pier maximum load-bearing capacity on mortar compressive strength; black line represents the brick compressive strength $f_c^{(b)}$ = 30 MPa.

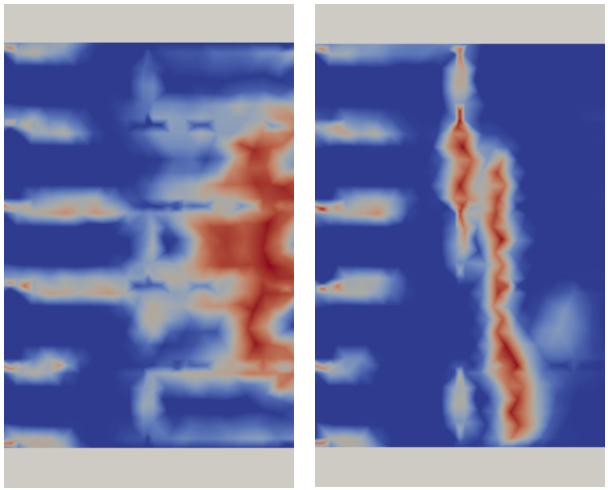

Figure 5.19: Crack patterns on masonry piers containing weak (f_c = 3 MPa, left) and strong (f_c = 33 MPa, right) mortar in compression.

5.5 Discussion of Results

The eccentrically compressed masonry pier was selected as a model example to address both, behavior in compression, being the most frequent loading of masonry elements, and tension, which is considered critical for masonry. The performance of the conventionally used lime-cement mortar was compared with mortars containing the pozzolanic alternative — metakaolin. To reach even better performance, crushed brick fragments were also used to replace a portion of stiff river sand. Such approach was adopted based on findings from the previous studies,

e.g. [13, 21, 23], claiming that mortars containing active pozzolans and relatively compliant crushed brick fragments exhibit a superior strength.

Series of compression and three-point bending tests were carried out primarily in order to obtain the input parameters characterizing individual materials in the FE model. The results of the basic material tests conclusively indicate that the addition of metakaolin provides the lime-based mortars with significantly higher strength than the addition of Portland cement. On the other hand, the pure-lime mortars lacking any additives appeared to be very poor. These findings are in agreement with several studies; e.g. by Vejmelková et al. [28] claiming that by replacing 20 % of lime with metakaolin the mortar compressive strength can increase up to five times and the flexural strength up to three times, which is in agreement with the study by Velosa et al. [5].

The partial replacement of sand grains by crushed brick fragments further improved the mechanical performance of the mortars, justifying their extensive use in ancient times [14, 17, 18]. The higher strength is attributed to a reduction of shrinkage-induced cracking due to presence of the compliant brick fragments. This in turn leads to a better mortar integrity as suggested by Nežerka et al. [13, 20], and lower stress concentrations in the vicinity of aggregates, as studied in detail in [24].

The superior strength of the metakaolin-enriched mortars was also reflected by the increased load-bearing capacity of the tested piers, in particular from 360 kN and 600 kN, reached in the case of pure-lime (L-SCB) and lime-cement mortar (LC-S), respectively, up to 800 kN when 30 % of the binder was replaced by metakaolin (LMK-S). Moreover, the load-bearing capacity was further increased with the use of mortar containing crushed bricks (LMK-SCB), reaching up to 915 kN. This strength enhancement can explain the resistance and longevity of numerous ancient masonry structures containing cocciopesto [35, 42]. The extraordinary strength of the LMK-SCB mortar together with the good adhesion between the mortar and bricks should also result in an increased seismic resistance, as suggested by Costa et al. [131].

Knowing the basic material parameters, the damage-plastic material model used for the 3D FE simulations allowed to reproduce the experimental results with a relatively high accuracy, despite the complex composite action taking place in masonry. Even the simplest case of uniaxial compression leads to a triaxial compression in mortar, while introducing a uniaxial compression and biaxial tension in usually stiffer masonry units. Such scenario usually leads to the formation of vertical splitting cracks leading to a complete failure [132].

The chosen strategy to model the bricks and mortars as two distinct materials allowed to investigate the relationship between the individual material parameters and structural behavior of the masonry pier. Our findings that the mortar compressive strength has the biggest impact on the load-bearing capacity is in contradiction with the conclusions of Gumaste et al. [133] and Pavía and Hanley [134]. They claim that mortar compressive strength has just a minor impact on the behavior of masonry subjected to uniaxial compression. This discrepancy can be probably attributed to a different experimental set-up, in particular to the eccentricity of loading introduced in our study. The eccentric loading was responsible for a significant deformation of the bed joints, leading to a non-linear response at relatively early loading-stage.

The assumption that the difference between the Young's modulus of bricks and mortar is the precursor of the compression failure [135] was not confirmed, and the load-bearing capacity of the masonry piers was almost independent of mortar stiffness.

5.6 Conclusion

The chosen strategy to combine the comprehensive experimental analysis together with the numerical modeling revealed new findings to be considered during the design of bed joint mortars. Even though the study was focused purely on the lime-based mortars, because these are accepted by the authorities for cultural heritage, our findings can also help with the design of mortars and masonry based on modern materials.

The results of the basic material tests demonstrate the superior strength of mortars containing metakaolin, when compared to a pure-lime or lime-cement ones. The mortar strength was further increased by the addition of crushed bricks, which is attributed to the reduction of microcracking due to shrinkage around the relatively compliant ceramic fragments. It can be also conjectured that the hydraulic reaction in mortars containing metakaolin was promoted by the presence of water retained within the crushed brick fragments.

The enhanced strength of the metakaolin-rich mortars, and especially those containing crushed bricks, was reflected in the significantly increased load-bearing capacity of masonry piers loaded by the combination of compression and bending. This can explain the extraordinary resistance and durability of ancient masonry structures with cocciopesto mortars. Moreover, the utilization of the waste by-products from ceramic plants makes the material sustainable for a relatively low cost, since the fragments partially replace binder, being the most expensive mortar component.

Based on experimental observations the damage-plastic material model seemed to be the most appropriate to describe the constitutive behavior of mortars and bricks in the FE model. The chosen strategy to model the mortars and bricks as distinct materials allowed the relatively accurate reproduction of the experimentally obtained data in terms of the predicted crack patterns and load-displacement diagrams. Results of the numerical simulations and DIC analysis clearly demonstrate that the mortar properties have an enormous impact on the load-bearing capacity of masonry, strain localization, and the formation of cracks.

The numerical analysis, based on the FE model verified through the comprehensive experimental analysis, revealed that mortar compressive strength is the key material parameter with respect to the load-bearing capacity of the piers subjected to the combination of bending and compression. Considering the studied geometry and boundary conditions, tensile strength and mortar Young's modulus influence the pier behavior and modes of failure, however, do not have any significant impact on the load-bearing capacity.

Chapter 6

Conclusions and Final Remarks

The main objective of the project focused on the development of a modern cocciopesto mortar with superior mechanical properties was met despite facing unforeseen obstacles, and beside the desired outcome the research yielded numerous new findings. By investigating the mortar behavior and properties on multiple scales, it was possible to unveil the relationships between the mortar microstructure and its structural behavior on macro-scale.

First, the investigation of lime-pozzolan pastes without aggregates provided valuable information about the mortar matrix. Metakaolin proved to be much more reactive pozzolan than crushed bricks, as demonstrated by the pozzolanic activity test results, weight development during hardening, and TGA. Moreover, mercury intrusion porosimetry indicated the presence of hydration products in the metakaolin-rich pastes. The SEM-BSE microscopy gave a clue about the microstructure, and the observed disintegration of metakaolin and lime particles suggested their reaction. Elemental mapping by SEM-EDX clearly demonstrated the integration of silica from metakaolin grains in lime and, on the contrary, unreacted crushed brick particles. Based on the study of unreinforced pastes, shrinkage of the mortar matrix was quantified for various pozzolan amounts, and most importantly the mechanical properties were assessed using basic material tests. These findings explained the increase of strength in lime-based mortars containing pozzolans — since the observed strength enhancement of the pastes with the addition of pozzolans was not significant, the increase of strength in pozzolan-rich mortars was attributed the lower shrinkage, resulting in a reduction of micro-cracking.

The assumption that the brick-matrix interface is reinforced by hydration products, which could explain the remarkable earthquake resistance and durability of masonry structures with cocciopesto, was subjected to an integrated micromechanical and chemical study. To that purpose a sample from a late Byzantine church built approximately in 9-th century in the district Üsküdar, located in Istanbul, Turkey, was analysed. First, SEM-BSE microscopy was employed to observe the microstructure, and the micro chemical analysis was accomplished by means of SEM-EDX. The SEM analyses revealed the reaction rims with reduced porosity at the boundary of crushed brick fragments in the thickness up to 200 μm due to filling of voids by CaO. The presence of aluminosilicates that reinforce ITZ was also detected in a thickness of 20–30 μm around the fragments. Using grid nanoindentation it was proven that the interface exhibits an increased elastic stiffness compared to the bulk matrix. In particular, a steep stiffness gradient within ITZ was located in a narrow band of the thickness about 20–30 μm, which

is in agreement with SEM-EDX findings. The average ITZ Young's modulus was approximately 18.4 GPa, which corresponds to the stiffness of low-density CSH found in cementitious materials. However, such phenomenon was not observed in the case of reproduced mortars after the curing period of 3 months, which had been too short to allow the formation of reinforcing layer. On the other hand, the vicinity of brick fragments was not affected by the formation of shrinkage cracks as in the case of stiff sand aggregates. These information contributed to a better understanding cocciopesto mortars and provided the input data for their further micromechanical modeling.

The simple micromechanics-based model of lime-based mortars for the estimation of their elastic stiffness, compressive and tensile strength, and fracture energy was proposed and validated against experiments. Based on experimental observations, the model was formulated in such a way to account for the shrinkage-induced cracks that significantly influence the overall mechanical performance. While the Mori-Tanaka and Dilute Approximation were used to estimate the overall stiffness, a J_2-based failure condition involving the average stress in matrix was adopted under compression, and under tension the incremental Mori-Tanaka method coupled with the isotropic damage law and crack bend theory was employed. The validated model provided a reliable tool for optimizing the mortar mix composition.

Based on the modeling outcomes, a cocciopesto mortar mixture ensuring superior strength parameters was proposed. The mortar contained an optimized amount of lime, metakaolin, sand, and crushed bricks, in the mass ratios 0.7, 0.3, 1.0, and 1.5, respectively. The mortar performance was compared with various mixtures intended for repairs of historic structures and the reference one, enriched by Portland cement. Acquisition of basic material parameters revealed that the mortars containing metakaolin, when compared to a pure-lime or lime-cement ones, exhibit a superior strength, especially when reinforced by crushed brick fragments. This phenomenon is attributed to the reduction of microcracking and to the promotion of hydraulic reaction in the metakaolin enriched matrix due to excess of water, retained in the porous ceramic fragments. The enhanced strength of the developed cocciopesto mortar was reflected in a significantly increased load-bearing capacity of masonry piers loaded by the combination of compression and bending, which can explain the extraordinary resistance and durability of ancient masonry structures with cocciopesto. Based on the response of mortar to mechanical loading a damage-plastic material model was chosen as the most appropriate to describe their constitutive behavior. The results of FE simulations and DIC analysis clearly demonstrated that the mortar properties have an enormous impact on the behavior of masonry, strain localization, and formation of cracks under mechanical loading.

To test the performance of the developed mortar in masonry exposed to natural agents such as wet-dry and freeze-thaw cycles in outdoor environment, a full-scale U-shaped wall (Figure 6.1) was built and visually monitored over the period of 15 months. During that time there was a long episode of high temperatures as well as cycles of precipitations and freezing. Despite these conditions, regular visual inspections did not reveal any damage to the masonry or bed joints, only the formation of algae and lichen due to presence of extreme moisture at the bottom part of the wall, Figure 6.2. In addition, one year after the wall construction, a modal analysis demonstrated a perfect integrity of the wall as indicated by the shape of eigenmodes in Figure 6.3. The results of the laboratory tests combined with the outcomes of the masonry wall monitoring led to a registration of the mortar composition in the form of utility model no. 28520 as of August, 2015.

Figure 6.1: Masonry wall built from clay bricks and the optimized cocciopesto mortar, located in the yard of the Faculty of Civil Engineering, CTU in Prague.

Figure 6.2: Bottom part of the wall after 13 months since its construction, water rising by capillary action, resulting in the growth of algae and lichen at the masonry surface.

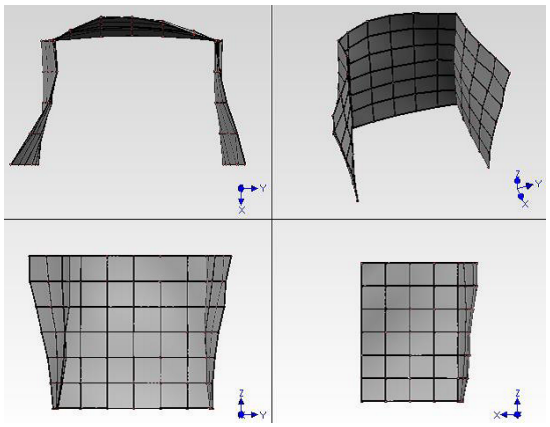

Figure 6.3: Eigenmodes of the masonry wall with the cocciopesto mortar revealing that no internal discontinuities formed in the structure.

References

[1] A. Arizzi and G. Cultrone. Aerial lime-based mortars blended with a pozzolanic additive and different admixtures: A mineralogical, textural and physical-mechanical study. *Construction and Building Materials*, 31:135–143, 2012. doi: 10.1016/j.cemconres.2012.03.008.

[2] F. Veniale, M. Setti, C. Rodriguez-Navarro, S. Lodola, W. Palestra, and A. Busetto. Thamasite as decay product of cement mortar in brick masonry of a church near Venice. *Cement & Concrete Composites*, 25:1123–1129, 2003. doi: 10.1016/s0958-9465(03)00159-8.

[3] K. Callebaut, J. Elsen, K. Van Balen, and W. Viaene. Nineteenth century hydraulic restauration mortars in the Saint Michael's Church (Leuven, Belgium). Natural hydraulic lime or cement? *Cement and Concrete Research*, 31:397–403, 2001. doi: 10.1016/s0008-8846(00)00499-3.

[4] A. Moropoulou, A. Bakolas, and S. Anagnostopoulou. Composite materials in composite structures. *Cement & Concrete Composites*, 27:295–300, 2005. doi: 10.1016/j.cemconcomp.2004.02.018.

[5] A. L. Velosa, F. Rocha, and R. Veiga. Influence of chemical and mineralogical composition of metakaolin on mortar characteristics. *Acta Geodynamica et Geomaterialia*, 153:121–126, 2009.

[6] M. P. Seabra, J. A. Labrincha, and V. M. Ferreira. Rheological behaviour of hydraulic lime-based mortars. *Journal of the European Ceramic Society*, 27:1735–1741, 2007. doi: 10.1016/j.jeurceramsoc.2006.04.155.

[7] A. Sepulcre-Aguilar and F. Hernández-Olivares. Assessment of phase formation in lime-based mortars with added metakaolin, Portland cement and sepiolite, for grouting of historic masonry. *Cement and Concrete Research*, 40:66–76, 2010. doi: 10.1016/j.cemconres.2009.08.028.

[8] A. Moropoulou, A. Bakolas, and E. Aggelakopoulou. Evaluation of pozzolanic activity of natural and artificial pozzolans by thermal analysis. *Thermochimica Acta*, 420: 135–140, 2004. doi: 10.1016/j.tca.2003.11.059.

[9] Z. Slížková. Characteristics of metakaoline modified mortars applied on historic objects. *Metakaolin, Brno*, pages 146–155, 2009.

[10] I. Papayianni. The longevity of old mortars. *Applied Physics A*, 83:685–688, 2006. doi: 10.1007/s00339-006-3523-2.

[11] I. Papayianni and M. Stefanidou. Durability aspects of ancient mortars of the archeological site of Olynthos. *Journal of Cultural Heritage*, 8:193–196, 2007. doi: 10.1016/j.culher.2007.03.001.

[12] D. Wilk, L. Bratasz, and R. Kozlowski. Shrinkage cracking in Roman cement pastes and mortars. *Cement and Concrete Research*, 53:168–175, 2013. doi: 10.1016/j.cemconres.2013.03.012.

[13] V. Nežerka, Z. Slížková, P. Tesárek, T. Plachý, D. Frankeová, and V. Petráňová. Comprehensive study on microstructure and mechanical properties of lime-pozzolan pastes. *Cement and Concrete Research*, 64:17–29, 2014. doi: 10.1016/j.cemconres.2014.06.006.

[14] L. G. Mallinson and I. L. Davies. A historical examination of concrete. *Office for Official Publications of the European Communities, Luxembourg, Final Report CD-NA-10937-EN-C*, 1987.

[15] A. Farci, D. Floris, and P. Meloni. Water permeability vs. porosity in samples of Roman mortars. *Journal of Cultural Heritage*, 6:55–59, 2005. doi: 10.1016/j.culher.2004.08.002.

[16] L. Sbordoni-Mora. Les matériaux des enduits traditionnels. *In: Proceedings of the ICCROM Symposium on Mortars, Cements and Grouts used in the Conservation of Historic Buildings, Rome*, pages 375–383, 1981.

[17] P. Degryse, J. Elsen, and M. Waelkens. Study of ancient mortars from Sagalassos (Turkey) in view of their conservation. *Cement and Concrete Research*, 21:1457–1463, 2002. doi: 10.1016/s0008-8846(02)00807-4.

[18] G. Baronio, L. Binda, and N. Lombardini. The role of brick pebbles and dust in conglomerates based on hydrated lime and crushed bricks. *Construction and Building Materials*, 11:33–40, 1997. doi: 10.1016/s0950-0618(96)00031-1.

[19] V. Nežerka and J. Zeman. A micromechanics-based model for stiffness and strength estimation of cocciopesto mortars. *Acta Polytechnica*, 52:29–37, 2012.

[20] V. Nežerka, J. Němeček, Z. Slížková, and P. Tesárek. Investigation of crushed brick-matrix interface in lime-based ancient mortar by microscopy and nanoindentation. *Cement & Concrete Composites*, 55:122–128, 2015. doi: 10.1016/j.cemconcomp.2014.07.023.

[21] V. Nežerka, P. Tesárek, and J. Zeman. Fracture-micromechanics based model of mortars susceptible to shrinkage. *Key Engineering Materials*, 592–593:189–192, 2014. doi: 10.4028/www.scientific.net/kem.592-593.189.

[22] B. F. Dela and H. Stang. Two-dimensional analysis of crack formation around aggregates in high-shrinkage cement paste. *Engineering Fracture Mechanics*, 65: 149–164, 2000. doi: 10.1016/s0013-7944(99)00113-7.

[23] P. Tesárek, V. Nežerka, P. Padevět, J. Antoš, and T. Plachý. Influence of aggregate stiffness on fracture-mechanical properties of lime-based mortars. *Applied Mechanics and Materials*, 486:289–294, 2014. doi: 10.4028/www.scientific.net/amm.486.289.

[24] V. Nežerka, J. Němeček, and J. Zeman. Micromechanics-based simulations of compressive and tensile testing on lime-based mortars, arxiv preprint 1512.01227. 2015.

[25] P. Johannesson and P. Utgenannt. Microstructural changes caused by carbonation of cement mortar. *Cement and Concrete Research*, 31:925–931, 2001. doi: 10.1016/s0008-8846(01)00498-7.

[26] I. Papayianni and M. Stefanidou. Strength-porosity relationships in lime-pozzolan mortars. *Construction and Building Materials*, 20:700–705, 2005. doi: 10.1016/j.conbuildmat.2005.02.012.

[27] M. Stefanidou and I. Papayianni. The role of aggregates on the structure and properties of lime mortars. *Cement & Concrete Composites*, 27:914–919, 2005. doi: 10.1016/j.cemconcomp.2005.05.001.

[28] E. Vejmelková, M. Keppert, Z. Keršner, P. Rovnaníková, and R. Černý. Mechanical, fracture-mechanical, hydric, thermal, and durability properties of lime-metakaolin plasters for renovation of historical buildings. *Construction and Building Materials*, 31: 22–28, 2012. doi: 10.1016/j.conbuildmat.2011.12.084.

[29] J. Lanas, J. L. Pérez Bernal, M. A. Bello, and J. I. Alvarez Galindo. Mechanical properties of natural hydraulic lime-based mortars. *Cement and Concrete Research*, 34: 2191–2201, 2004. doi: 10.1016/j.cemconres.2004.02.005.

[30] Ö. Cizer. *Competition between carbonation and hydration on the hardening of calcium hydroxide and calcium silicate binders*. Phd thesis, Katholieke Universiteit Leuven, 2009.

[31] G. Baronio and L. Binda. Study of the pozzolanicity of some bricks and clays. *Construction and Building Materials*, 11:41–46, 1997. doi: 10.1016/s0950-0618(96)00032-3.

[32] P. S. De Silva and F. P. Glasser. Phase relations in the system $CaO - Al_2O_3 - SiO_2 - H_2O$ relevant to metakaolin-calcium hydroxide hydration. *Cement and Concrete Research*, 23:627–639, 1993. doi: 10.1016/0008-8846(93)90014-z.

[33] M. F. Rojas and J. Cabrera. The effect of temperature on the hydration rate and stability of the hydration phases of metakaolin-lime-water systems. *Cement and Concrete Research*, 32:133–138, 2002. doi: 10.1016/s0008-8846(01)00642-1.

[34] J. Silva, J. Brito de, and R. Veiga. Incorporation of fine ceramics in mortars. *Construction and Building Materials*, 23:556–564, 2009. doi: 10.1016/j.conbuildmat.2007.10.014.

[35] A. Moropoulou, A. S. Cakmak, G. Biscontin, A. Bakolas, and E. Zendri. Advanced Byzantine cement based composites resisting earthquake stresses: the crushed brick/lime mortars of Justinian's Hagia Sophia. *Construction and Building Materials*, 16:543–552, 2002. doi: 10.1016/s0950-0618(02)00005-3.

[36] H. Böke, S. Akkurt, B. Ípekoğlu, and E. Uğurlu. Characteristics of brick used as aggregate in historic brick-lime mortars and plasters. *Cement and Concrete Research*, 36:1115–1122, 2006. doi: 10.1016/j.cemconres.2006.03.011.

[37] J. Elsen. Microscopy of historic mortars: A review. *Cement and Concrete Research*, 36:1416–1424, 2006. doi: 10.1016/j.cemconres.2005.12.006.

[38] M. Arandigoyen, J. L. Pérez Bernal, M. A. Bello López, and J. I. Alvarez. Lime-pastes with different kneading water: pore structure and capillary porosity. *Applied Surface Science*, 252:1449–1459, 2005. doi: 10.1016/j.apsusc.2005.02.145.

[39] R. M. Lawrence, T. J. Mays, S. P. Rigby, P. Walker, and D. D'Ayala. Effects of carbonation on the pore structure of non-hydraulic lime mortars. *Cement and Concrete Research*, 37:1059–1069, 2007. doi: 10.1016/j.cemconres.2007.04.011.

[40] M. J. Mosquera, B. Silva, B. Prieto, and E. Ruiz-Herrera. Addition of cement to lime-based mortars: Effect on pore structure and vapor transport. *Cement and Concrete Research*, 36:1635–1642, 2006. doi: 10.1016/j.cemconres.2004.10.041.

[41] A. Moropoulou, A. S. Cakmak, and N. Lohvyn. Earthquake resistant construction techniques and materials on Byzantine monuments in Kiev. *Soil Dynamics and Earthquake Engineering*, 19:603–615, 2000. doi: 10.1016/s0267-7261(00)00021-x.

[42] A. Moropoulou, A. Bakolas, and K. Bisbikou. Investigation of the technology of historic mortars. *Journal of Cultural Heritage*, 1:45–58, 2000. doi: 10.1016/s1296-2074(99)00118-1.

[43] S. Kramar, V. Zalar, M. Urosevic, W. Körner, A. Mauko, B. Mirtič, J. Lux, and A. Mladenović. Mineralogical and microstructural studies of mortars from the bath complex of the Roman *villa rustica* near Mošnje (Slovenia). *Materials Characterization*, 62:1042–1057, 2011. doi: 10.1016/j.matchar.2011.07.019.

[44] T. Rougelot, F. Skoczylas, and N. Burlion. Water desorption and shrinkage in mortars and cement pastes: experimental study and poromechanical model. *Cement and Concrete Research*, 39:36–44, 2009. doi: 10.1016/j.cemconres.2008.10.005.

[45] J. Lanas and J. I. Alvarez. Masonry repair lime-based mortars: factors affecting the mechanical behaviour. *Cement and Concrete Research*, 33:1867–1876, 2003. doi: 10.1016/s0008-8846(03)00210-2.

[46] A. M. Neville. *Properties of Concrete: Fourth Edition*. Longman, 1996.

[47] M. R. Veiga and F. Carvalho. Some performance characteristics of lime mortars for use on rendering and repointing of ancient buildings. *Proceedings* 5^{th} *International Masonry Conference, London*, pages 107–111, 1998.

[48] C. Giavarini, A. S. Ferretti, and M. L. Santarelli. Mechanical characteristics of Roman opus caementicium. *Fracture and Failure of Natural Building Stones*, pages 107–120, 2006. doi: 10.1007/978-1-4020-5077-0_7.

[49] Z. Hashin. Analysis of composite materials — a survey. *ASME Journal of Applied Mechanics*, 50:481–505, 1983. doi: 10.1115/1.3167081.

[50] T. Kanit, S. Forest, I. Galliet, V. Mounoury, and D. Jeulin. Determination of the size of the representative volume element for random composites: statistical and numerical approach. *International Journal of Solids and Structures*, 40:3647–3679, 2003. doi: 10.1016/s0020-7683(03)00143-4.

[51] R. Hill. Continuum micro-mechanics of elastoplastic polycrystals. *Journal of the Mechanics and Physics of Solids*, 13:89–101, 1965. doi: 10.1016/0022-5096(65)90023-2.

[52] Z. Hashin and S. Shtrikman. A variational approach to the theory of the elastic behavior of multiphase materials. *Journal of Mechanics and Physics of Solids*, 10: 343–352, 1963. doi: 10.1016/0022-5096(63)90060-7.

[53] S. Torquato. *Random Heterogeneous Materials: Microstructure and Macroscopic Properties*. Springer, New York, 2002. doi: 10.1115/1.1483342.

[54] J. D. Eshelby. The Determination of the Elastic Field of an Ellipsoidal Inclusion, and Related Problems. *Proceedings of the Royal Society of London*, 241:376–396, 1957. doi: 10.1098/rspa.1957.0133.

[55] T. Mori and K. Tanaka. Average stress in matrix and average elastic energy of materials with mixfitting inclusions. *Acta Metallurgica*, 21:571–574, 1973. doi: 10.1016/0001-6160(73)90064-3.

[56] Y. Benveniste. A new approach to the application of Mori-Tanaka theory in composite materials. *Mechanics of Materials*, 6:147–157, 1987. doi: 10.1016/0167-6636(87)90005-6.

[57] E. Herve and A. Zaoui. n-layered inclusion-based micromechanical modelling. *International Journal of Engineering Science*, 31:1–10, 1993. doi: http://dx.doi.org/10.1016/0020-7225(93)90059-4.

[58] M. Kachanov. A simple technique of stress analysis in elastic solids with many cracks. *International Journal of Fracture*, 20:R11–R19, 1985.

[59] M. Kachanov. Solids with cracks and non-spherical pores: proper parameters of defect density and effective elastic properties. *International Journal of Fracture*, 97:1–32, 2005.

[60] J. Vorel, V. Šmilauer, and Z. Bittnar. Multiscale simulations of concrete mechanical tests. *Journal of Computational and Applied Mathematics*, 236:4882–4892, 2012. doi: 10.1016/j.cam.2012.01.009.

[61] B. Pichler and Ch. Hellmich. Upscaling quasi-brittle strength of cement paste and mortar: A multi-scale engineering mechanics model. *Cement and Concrete Research*, 41:467–476, 2011. doi: 10.1016/j.cemconres.2011.01.010.

[62] K. J. Willam and E. P. Warnke. Constitutive model for the triaxial behaviour of concrete. *Proceedings of the International Association for Bridge and Structural Engineering*, 19:1–30, 1974.

[63] M. S. Akman, A. Güner, and I. H. Aksoy. The history and properties of Kheasan mortar and concrete. Turkish and Islamic science and technology in the 16th century. *Istanbul: ÌTÜ Research Center of History of Science and Technology I*, pages 101–112, 1986.

[64] R. Spence. Lime and Surkhi manufacture in India. *Appropriate Technology*, 1(4):6–8, 1974.

[65] V. Šmilauer, P. Hlaváček, F. Škvára, R. Šulc, L. Kopecký, and J. Němeček. Micromechanical multiscale model for alkali activation of fly ash and metakaolin. *Journal of Materials Science*, pages 1–11, 2011. doi: 10.1007/s10853-011-5601-x.

[66] J. Cabrera and M. F. Rojas. Mechanism of hydration of the metakaolin-lime-water system. *Cement and Concrete Research*, 31:177–182, 2000. doi: 10.1016/s0008-8846(00)00456-7.

[67] C. Rodriguez-Navarro, E. Hansen, and W. S. Ginell. Calcium hydroxide crystal evolution upon aging of lime putty. *Journal of the American Ceramic Society*, 91(11): 3032–3034, 1998. doi: 10.1111/j.1151-2916.1998.tb02735.x.

[68] S. P. Pandey and R. L. Sharma. Lime-pastes with different kneading water: pore structure and capillary porosity. *Applied Surface Science*, 252:1449–1459, 2005.

[69] G. C. Cordeiro, R. D. Toledo Filho, L. M. Tavares, and E. M. R. Fairbairn. Pozzolanic activity and filler effect of sugar cane bagasse ash in portland cement and lime mortars. *Cement & Concrete Composites*, 30:455–462, 2008. doi: 10.1016/j.cemconcomp.2008.01.001.

[70] T. Perraki, G. Kakali, and E. Kontori. Characterization and pozzolanic activity of thermally treated zeolite. *Journal of Thermal Analysis and Calorimetry*, 82:109–113, 2005. doi: 10.1007/s10973-005-0849-5.

[71] *CSN EN 459-2 — Building lime — Part 2: Test methods*, 2010. European Standard.

[72] A. Moropoulou, A. Bakolas, and K. Bisbikou. Characterization of ancient, Byzantine and later historic mortars by thermal and X-ray diffraction techniques. *Thermochemica Acta*, 269/270:779–995, 1995. doi: 10.1016/0040-6031(95)02571-5.

[73] M. Stefanidou. Methods for porosity measurement in lime-based mortars. *Construction and Building Materials*, 24:2572–2578, 2010. doi: 10.1016/j.conbuildmat.2010.05.019.

[74] S. Quellet, B. Bussiere, M. Aubertin, and M. Bnzaazoua. Microstructural evolution of cemented paste backfill: mercury intrusion porosimetry test results. *Cement and Concrete Research*, 37:1654–1665, 2007. doi: 10.1016/j.cemconres.2007.08.016.

[75] S. P. Pandey and R. L. Sharma. The influence of mineral additives on the strength and porosity of OPC mortar. *Cement and Concrete Research*, 30:19–23, 2000.

[76] A. Idiart, J. Bisschop, A. Caballero, and P. Lura. A numerical and experimental study of aggregate-induced shrinkage cracking in cementitious composites. *Cement and Concrete Research*, 42:272–281, 2012. doi: 10.1016/j.cemconres.2011.09.013.

[77] P. Grassl, H. S. Wong, and N. R. Buenfeld. Influence of aggregate size and volume fraction on shrinkage induced micro-cracking of concrete and mortar. *Cement and Concrete Research*, 40:85–93, 2010. doi: 10.1016/j.cemconres.2009.09.012.

[78] J. R. Rosell and I. R. Cantalapiedra. Simple method of dynamic Young's modulus determination in lime and cement mortars. *Materiales de Construccion*, 61:39–48, 2011. doi: 10.3989/mc.2010.53509.

[79] A. Malaikah, K. Al-Saif, and R. Al-Zaid. Prediction of the dynamic modulus of elasticity of concrete under different loading conditions. *International Conference on Concrete Engineering and Technology Universiti Malaya*, pages 32–39, 2004.

[80] P. Tesárek, T. Plachý, A. Hájková, P. Padevět, and M. Polák. Time evolution of "grey gypsum" mechanical properties. *Latest Trends in Engineering Mechanics, Structures, Engineering Geology, Athens, WSEAS Press*, pages 413–417, 2010.

[81] T. Plachý, P. Padevět, and M. Polák. Comparison of two txperimental techniques for determination of Young's modulus of concrete specimens. *Proceedings of the 5th WSEAS International Conference on Applied and Theoretical Mechanics - Recent Advances In Applied And Theoretical Mechanics, Athens, WSEAS Press*, pages 68–71, 2009.

[82] Ö. Cizer, K. Van Balen, D. Van Gemert, and J. Elsen. Blended cement-lime mortars for conservation purposes: Microstructure and strength development. *Proceedings of the 6th Conference Structural Analysis of Historical Constructions: Preserving Safety and Significance edition, Bath, CRC Press*, 2008.

[83] RILEM. Determination of the fracture energy of mortar and concrete by means of three-point bend tests on notched beams. *Materials and Structures*, 18:285–290, 1985.

[84] Z. P. Bažant and M. T. Kazemi. Size dependence of concrete fracture energy determined by RILEM work-of-fracture method. *International Journal of Fracture*, 51: 121–138, 1991. doi: 10.1007/978-94-011-3638-9_9.

[85] S. Muralidhara, B. K. Raghu Prasad, B. L. Karihaloo, and R. K. Singh. Size-independent fracture energy in plain concrete beams using tri-linear model. *Construction and Building Materials*, 25:3051–3058, 2011. doi: 10.1016/j.conbuildmat.2011.01.003.

[86] V. Vydra, K. Trtík, and F. Vodák. Size independent fracture energy of concrete. *Construction and Building Materials*, 26:357–361, 2012. doi: 10.1016/j.conbuildmat.2011.06.034.

[87] T. Nishikawa, M. Takatsu, and M. Daimon. Fracture behavior of hardened cement paste incorporating mineral additions. *Cement and Concrete Research*, 25:1218–1224, 1995. doi: 10.1016/0008-8846(95)00114-r.

[88] M. Stefanidou, V. Pachta, S. Konopissi, F. Karkadelidou, and I. Papayianni. Analysis and characterization of hydraulic mortars from ancient cisterns and baths in greece. *Materials and Structures*, 2013. doi: 10.1617/s11527-013-0080-y.

[89] J. J. Hughes and P. Trtik. Micro-mechanical properties of cement paste measured by depth-sensing nanoindentation: a preliminary correlation of physical properties with phase type. *Materials Characterization*, 53:223–231, 2004. doi: 10.1016/j.matchar.2004.08.014.

[90] G. Constantinides and F. J. Ulm. The effect of two types of C-S-H on the elasticity of cement-based materials: Results from nanoindentation and micromechanical modeling. *Cement and Concrete Research*, 34:67–80, 2004. doi: 10.1016/s0008-8846(03)00230-8.

[91] J. Němeček, V. Králík, and J. Vondřejc. Micromechanical analysis of heterogeneous structural materials. *Cement & Concrete Composites*, 36:85–92, 2013. doi: j.cemconcomp.2012.06.015.

[92] P. Tesárek and J. Němeček. Microstructural and micromechanical study of gypsum. *Chemické listy*, 105:852–853, 2011.

[93] P. Tesárek, T. Plachý, P. Ryparová, and J. Němeček. Micromechanical properties of different materials on gypsum basis. *Chemické listy*, 106:547–548, 2012.

[94] F.-J. Ulm, M. Vandamme, M. Bobko, and J. A. Ortega. Statistical indentation techniques for hydrated nanocomposites: concrete, bone, and shale. *Journal American Ceramics Society*, 90:2677–2692, 2007. doi: 10.1111/j.1551-2916.2007.02012.x.

[95] L. Sorelli, G. Constantinides, F.-J. Ulm, and F. Toutlemonde. The nano-mechanical signature of ultra high performance concrete by statistical nanoindentation techniques. *Cement and Concrete Research*, 38:1447–1456, 2008. doi: 10.1016/j.cemconres.2008.09.002.

[96] C. M. Neubauer, H. M. Jennings, and E. J. Garboczi. A three-phase model of the elastic and shrinkage properties of mortar. *Advanced Cement Based Materials*, 4:6–20, 1996. doi: 10.1016/s1065-7355(96)90058-9.

[97] A. Bakolas, E. Aggelakopoulou, and A. Moropoulou. Evaluation of pozzolanic activity and physico-mechanical characteristics in ceramic powder-lime pastes. *Journal of Thermal Analysis and Calorimetry*, 92:345–351, 2008. doi: 10.1007/s10973-007-8858-1.

[98] J. Němeček. Creep effects in nanoindentation of hydrated phases of cement pastes. *Materials Characterization*, 60:1028–1034, 2009. doi: 10.1016/j.matchar.2009.04.008.

[99] W. C. Oliver and G. M. Pharr. An improved technique for determining hardness and elastic modulus using load and displacement sensing indentation experiments. *Journal of Materials Research*, 7:1564–1583, 1992. doi: 10.1557/jmr.1992.1564.

[100] R. Hill. A self-consistent mechanics of composite materials. *Journal of the Mechanics and Physics of Solids*, 13:213–222, 1965. doi: 10.1016/0022-5096(65)90010-4.

[101] B. Budiansky. On the elastic moduli of some heterogeneous materials. *Journal of the Mechanics and Physics of Solids*, 13:223–227, 1965. doi: 10.1016/0022-5096(65)90011-6.

[102] Z. P. Bažant and B. H. Oh. Crack band theory for fracture of concrete. *Materials and Structures*, 16:155–177, 1983. doi: 10.1007/bf02486267.

[103] J. Bisschop and J. G. M. van Mier. Effect of aggregates on drying shrinkage microcracking in cement-based composites. *Materials and Structures*, 35:453–461, 2002. doi: 10.1007/bf02483132.

[104] G. W. Milton. *The Theory of Composites*. Cambridge Monographs on Applied and Computational Mathematics. Cambridge University Press, 2002. doi: 10.1115/1.1553445.

[105] B. Pichler, C. Hellmich, and J. Eberhardsteiner. Spherical and acicular representation of hydrates in a micromechanical model for cement paste: prediction of early-age elasticity and strength. *Acta Mechanica*, 203(3):137–162, 2009. doi: 10.1007/s00707-008-0007-9.

[106] B. Patzák and Z. Bittnar. Design of object oriented finite element code. *Advances in Engineering Software (`www.oofem.org`)*, 32:759–767, 2001. doi: 10.1016/s0965-9978(01)00027-8.

[107] M. Jirásek. *Comments on microplane theory, Mechanics of Quasi-Brittle Materials and Structures, ed. G.Pijaudier-Cabot, Z. Bittnar, and B. Gérard*. Hermès Science Publications, Paris, 1999.

[108] P. H. Feenstra and R. de Borst. Constitutive model for reinforced concrete. *Journal of Engineering Mechanics, ASCE*, 121:587–595, 1995. doi: 10.1061/(asce)0733-9399(1995)121:5(587).

[109] Z. P. Bažant and G. Pijaudier-Cabot. Measurement of characteristic length of nonlocal continuum. *Journal of Engineering Mechanics*, 115(4):755–767, 1989. doi: 10.1061/(asce)0733-9399(1989)115:4(755).

[110] A. U. Nilsen and P. J. M. Monteiro. Concrete: a three phase material. *Cement and Concrete Research*, 23:147–151, 1993. doi: 10.1016/0008-8846(93)90145-y.

[111] N. P. Daphalapurkar, F. Wang, B. Fu, H. Lu, and R. Komanduri. Determination of mechanical properties of sand grains by nanoindentation. *Experimental Mechanics*, 51: 719–728, 2011. doi: 10.1007/s11340-010-9373-z.

[112] C. C. Yang. Effect of the transition zone on the elastic moduli of mortar. *Cement and Concrete Research*, 28:727–736, 1998. doi: 10.1016/s0008-8846(98)00035-0.

[113] M. Drdácký and D. Michoinová. Lime mortars with natural fibres. *Britle Matrix Composites, Proceedings of the 7th Int. Symposium*, pages 523–532, 2003.

[114] V. Nežerka, J. Antoš, J. Litoš, P. Tesárek, and J. Zeman. Influence of mortar properties on structural performance of masonry piers, arxiv preprint 1512.01227. 2015.

[115] M. Radovic, E. Curzio-Lara, and Riester L. Comparison of different techniques for determination of elastic properties of solids. *Materials Science and Engineering*, A368: 56–70, 2004. doi: 10.1016/j.msea.2003.09.080.

[116] I. Yamaguchi. A laser speckle strain gauge. *Journal of Physics E: Scientific Instruments*, 14:1270, 1981. doi: 10.1088/0022-3735/14/11/012.

[117] W. H. Peters and W. F. Ranson. Digital imaging techniques in experimental stress analysis. *Optical Engineering*, 21:427–431, 1982. doi: 10.1117/12.7972925.

[118] P. Lava, S. Cooreman, S. Coppieters, M. De Strycker, and D. Debruyne. Assessment of measuring errors in DIC using deformation fields generated by plastic FEA. *Optics and Lasers in Engineering*, 47:747–753, 2009. doi: 10.1016/j.optlaseng.2009.03.007.

[119] M. Bornert, F. Brémand, P. Doumalin, J.C. Dupré, M. Fazinni, M. Grédiac, F. Hild, S. Mistou, J. Molimard, J. J. Orteu, L. Robert, Y. Surrel, P. Vacher, and B. Wattrisse. Assessment of digital image correlation errors: Methodology and results. *Experimental Mechanics*, 49:353–370, 2009. doi: 10.1007/s11340-012-9704-3.

[120] B. Pan, L. Yu, D. Wu, and L. Tang. Systematic errors in two-dimensional digital image correlation due to lens distortion. *Optics and Lasers in Engineering*, 51:140–147, 2013. doi: 10.1016/j.optlaseng.2012.08.012.

[121] J. Blaber, B. Adair, and A. Antouniou. Ncorr: Open-source 2d digital image correlation matlab software. *Experimental Mechanics*, 55:1105–1122, 2015. doi: 10.1007/s11340-015-0009-1.

[122] V. Nežerka. Ncorr_post: DIC Post-Processing Tool, http://mech.fsv.cvut.cz/ nezerka/dic/index.htm. *CTU in Prague*, 2014.

[123] P. Lourenço. Computations on historic masonry structures. *Progress in Structural Engineering and Materials*, 4:301–319, 2002. doi: 10.1002/pse.120.

[124] A. Wawrzynek and A. Cincio. Plastic-damage macro-model for non-linear masonry structures subjected to cyclic or dynamic loads. *In: Proc. Conf. Analytical Models and New Concepts in Concrete and Masonry Structures, AMCM, Gliwice, Poland*, 2005.

[125] W. F. Zhang and H. Wang. Elasticity damage and plastic analyses of masonry. *Applied Mechanics and Materials*, 166–169:1454–1458, 2012. doi: 10.4028/www.scientific.net/amm.166-169.1454.

[126] M. Jirásek and P. Grassl. Damage-plastic model for concrete failure. *International Journal of Solids and Structures*, 43:7166–7196, 2006. doi: 10.1016/j.ijsolstr.2010.12.005.

[127] M. Jirásek and M. Bauer. Numerical aspects of the crack band approach. *Computers & Structures*, 110–111:60–78, 2012. doi: 10.1016/j.compstruc.2012.06.006.

[128] V. Corinaldesi. Mechanical behavior of masonry assemblages manufactured with recycled-aggregate mortars. *Cement & Concrete Composites*, 31:505–510, 2009. doi: 10.1016/j.cemconcomp.2009.05.003.

[129] C. Sandoval and P. Roca. Study of the influence of different parameters on the buckling behaviour of masonry walls. *Construction and Building Materials*, 35:888–899, 2012. doi: 10.1016/j.conbuildmat.2012.04.053.

[130] M. Valluzzi, L. Binda, and C. Modena. Mechanical behaviour of historic masonry structures strengthened by bed joints structural repointing. *Construction and Building Materials*, 19:63–73, 2005. doi: 10.1016/j.conbuildmat.2004.04.036.

[131] A. A. Costa, A. Arêde, A. Costa, J. Guedes, and B. Silva. Experimental testing, numerical modelling and seismic strengthening of traditional stone masonry: comprehensive study of a real Azorian pier. *Bulletin of Earthquake Engineering*, 10: 135–159, 2012. doi: 10.1007/s10518-010-9209-3.

[132] H. B. Kaushik, D. C. Rai, and S. K. Jain. Stress-strain characteristics of clay brick masonry under uniaxial compression. *Journal of Materials in Civil Engineering*, 19: 728–739, 2007. doi: 10.1061/(asce)0899-1561(2007)19:9(728).

[133] K. S. Gumaste, K. S. Nanjunda Rao, B. V. Venkatarama Reddy, and K. S. Jagadish. Strength and elasticity of brick masonry prisms and wallettes under compression. *Materials and Structures*, 40:241–253, 2007. doi: 10.1617/s11527-006-9141-9.

[134] S. Pavía and R. Hanley. Flexural bond strength of natural hydraulic lime mortar and clay brick. *Materials and Structures*, 43:913–922, 2010. doi: 10.1617/s11527-009-9555-2.

[135] A. Zucchini and P. B. Lourenço. Mechanics of masonry in compression: Results from a homogenisation approach. *Computers and Structures*, 85:193–204, 2007. doi: 10.1016/j.compstruc.2006.08.054.